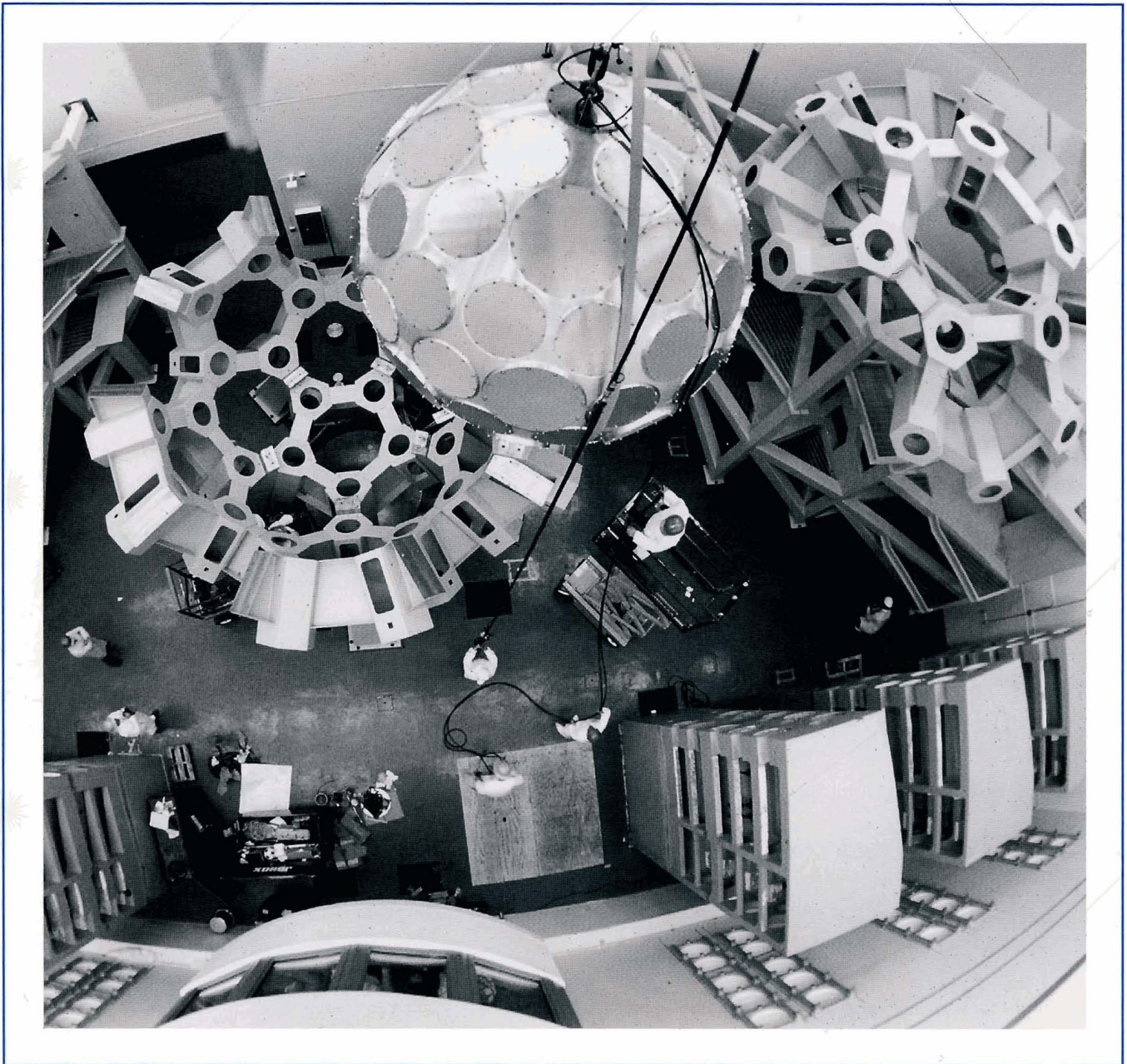# LLE Review

Quarterly Report

UR
LLE

About the Cover:

A remote camera suspended from the OMEGA target bay crane captured the November 1993 installation of the Upgrade target chamber—a DOE milestone achievement. The 11-ft-diam, 3.5-in.-thick, 6-ton aluminum chamber is shown being lowered into the bottom section of the 22-ft-diam target mirror structure (TMS). To the right of the chamber, the preassembled top section of the TMS rests atop the south-end mirror structure. After the chamber was bolted into the TMS, the top section was moved into place, thus completing the assembly. Also visible in the foreground are the massive final alignment sensor package structures, which will incorporate the alignment and diagnostic sensors for each laser beamline. All of the major structures are now installed in the target bay, except the TMS personnel platform. Installation of the optomechanical assemblies begins in early 1994.

For questions or comments, contact Albert Simon, *Editor*, Laboratory for Laser Energetics, 250 East River Road, Rochester, NY 14623-1299, (716) 275-7703.

LLE Review

UR
LLE

Quarterly Report

Contents

In Brief

The three-month period of October–December 1993 is covered by this volume of the LLE Review. During this quarter, the visible fruits of our long design labors on the OMEGA Upgrade began to appear. The target mirror structure was put in place, along with the target chamber itself. The laser bay structures were also installed, and the bay is now being prepared to receive optomechanical, control, and laser assemblies. Further details are in the OMEGA Upgrade Status Report in this issue.

Theory and analysis of previous experiments continued during this reporting period. Articles contained herein describe an improved theory of the ablative Rayleigh-Taylor instability; a novel proposal for characterizing plasma-density profiles by using grid image refractometry; a much-improved treatment of the damping of ion sound waves in a mixture of light and heavy ions; and, finally, a new interpretation of measurements of 3/2-harmonic radiation emitted from the long-scale-length plasmas created in earlier OMEGA experiments.

Highlights of the research reported in this issue include

- Linear stability analysis of unsteady ablation fronts is carried out for a semi-infinite uniform medium. For a laser-accelerated target, it is shown that a properly selected modulation of the laser intensity can lead to the dynamic stabilization or growth-rate reduction of a large portion of the unstable spectrum. The theory is in qualitative agreement with the numerical results obtained by using the two-dimensional hydrodynamic code *ORCHID*.

- Grid image refractometry (GIR) is a more general Schlieren technique for experimental determination of density profiles. Here the technique is illustrated by analysis of an experiment carried out at KMS Fusion on the CHROMA laser. The extracted profiles compare quite closely with those obtained using the code *SAGE*.

- Collisional damping of ion-acoustic waves was calculated for a mixture of light and heavy ions. The results are strikingly different from those using a single-species average-ion model. The improved result includes a new joule term as well as thermal diffusion and viscous damping contributions. The overall damping rate can be increased as much as 58-fold, when evaluated properly.

- Analysis of the observed emission of radiation near the 3/2 harmonic of the irradiating laser frequency shows that any interpretation in terms of self-interaction of the laser beam with the primary plasmons it created via the two-plasmon instability (TPI) is not credible. Rather, it seems necessary to invoke a secondary electron-plasma-wave decay (EPD) of the "blue" plasmon resulting from the TPI. This secondary EPD has its own threshold, exceeded only when the TPI is well above its threshold. Hence, onset of this 3/2 signal is not a good measure of onset of the TPI. The k-dependence of the EPD also explains why only spectral splittings corresponding to the Landau cutoff are observed.

Albert Simon
Editor

Stability Analysis of Unsteady Ablation Fronts

The classical Rayleigh-Taylor instability[1] occurs when a heavy fluid is accelerated by a lighter fluid. In inertial-confinement fusion (ICF) the heavy fluid is the compressed ablated target material that is accelerated by the low-density ablated plasma. The classical treatment of the incompressible Rayleigh-Taylor instability leads to a linear growth rate given by $\gamma = \sqrt{|kg|A}$, where k is the instability wave number, g is the acceleration, and A is the Atwood number $A = (\rho_h - \rho_l)/(\rho_h + \rho_l)$. ($\rho_l$ and ρ_h represent the light- and heavy-fluid densities, respectively.) For typical (ICF) parameters, a classical Rayleigh-Taylor instability would produce an unacceptably large amount of distortion in the unablated target, resulting in a degraded capsule performance with respect to the final core conditions. Thus, it is important to study the possible means for suppression of the ablation surface instability in ICF. It has been recently shown that the ablation process leads to convection of the perturbation away from the interface between the two fluids.[2-5] Since the instability is localized at the interface, the ablative convection stabilizes short-wavelength modes. The typical growth rate of the ablative Rayleigh-Taylor instability can be written in the following approximate form:[3]

$$\gamma = \sqrt{|kg|A} - \beta |kV_a| ,$$ (1)

where V_a is the ablation velocity and β is a numerical factor $(\beta \simeq 3-4)$.

In this article we show that a properly selected modulation of the laser intensity can significantly reduce the unstable spectrum and the maximum growth rate. To treat the analytic linear stability of unsteady ablation fronts, we consider a simplified sharp boundary model consisting of a heavy fluid, with density ρ_h, adjacent to a lighter fluid (ρ_l), in the force field $g(t) = g(t)\mathbf{e}_y$ in a direction opposite to the density gradient [$g(t) < 0$ and $\mathbf{e}_y$ is the unit vector in the direction of the density gradient] and with an arbitrary time dependence. The heavy fluid is moving downward with velocity $\mathbf{U}_h = -V_a\mathbf{e}_y$, and the lighter fluid is ejected with velocity U_l.

The equilibrium velocities $U_l(t)$ and $U_h(t)$ are both dependent on the ablation ratio per unit surface $\dot{m}(t)$ that is treated as an arbitrary function of time. The equilibrium can be readily derived from conservation of mass and momentum. We consider a class of equilibria with nonuniformities localized at the interface between the two fluids. Continuity of the mass flow and the pressure balance across the interface lead to the following conditions:

$$\rho_l U_l(t) = \rho_h U_h(t)$$ (2)

$$P_h - P_l = \rho_l U_l^2(t) - \rho_h U_h^2(t) ,$$ (3)

where P_h and P_l represent the pressure of the heavy and light fluid, respectively, at the interface. Notice that U_l and U_h are negative in the chosen frame of reference. We assume that the discontinuities in the equilibrium quantities can be removed by including the physics of the ablation process.

The linear stability problem can be greatly simplified by an appropriate choice of the linearized equation of state. It is widely known that the most Rayleigh-Taylor unstable perturbations are incompressible. Furthermore, ablative stabilization is a convective process and is, therefore, independent of the equation of state. It follows that the essential physics of the instability can be captured by a simple incompressible flow model. The stability analysis proceeds in a standard manner. All perturbed quantities are written as $Q_1 = \tilde{Q}(y,t)\exp(ikx)$, and the system of equations describing the linear evolution of the perturbation assumes the following form:

$$(\partial_t + U_j\partial_y)\tilde{\rho}_j = 0,$$

$$\rho_j(\partial_t + U_j\partial_y)\tilde{v}_{jx} = -ik\tilde{p}_j$$ (4)

$$\rho_j(\partial_t + U_j\partial_y)\tilde{v}_{jy} + \tilde{\rho}_j\partial_t U_j = -\partial_y\tilde{p}_j + \tilde{\rho}_j g$$

$$ik\tilde{v}_{jx} + \partial_y\tilde{v}_{jy} = 0,$$

where the subscript j denotes the heavy fluid region ($j = h$) and the light fluid region ($j = l$) and $\partial_y = \partial/\partial y$, $\partial_t = \partial/\partial t$. The two regions are separated by an interface (the ablation front) that moves with the heavy fluid. In order to match the solutions in the two regions, an equation describing the evolution of the interface is needed. Such an equation can be easily derived by a comparison with a nonablative equilibrium ($U_h = 0$). In that case the interface $\left[y = \tilde{\eta}(t)\exp(ikx) \right]$ moves with the heavy fluid, and the rate of distortion $\left(\partial_t\tilde{\eta} \right)$ is equal to the normal component of the velocity, $\partial_t\tilde{\eta} = \tilde{v}_{hy}(y = 0,t)$. In the ablative case, the heavy fluid is moving toward the ablation front with velocity $U_h = -V_a$. A Lagrangian surface, coming from $y = +\infty$, would become distorted as it approaches the interface where the instability is localized (Fig. 57.1). As for static equilibria, the rate of distortion $\left(\tilde{\xi} \right)$ of that surface is still equal to the normal component of the velocity:

$$\frac{d\tilde{\xi}}{dt} = \tilde{v}_{hy}. \tag{5a}$$

However, since the surface is moving, the time derivative has to be convective $\left(d_t = \partial_t + U_h\partial_y \right)$. From Eq. (5a) the distortion of a Lagrangian surface can be written in the following integral form:

$$\tilde{\xi}(t) = \int_{-\infty}^{t} \tilde{v}_{hy}\left[y_0(t'),t' \right]dt', \tag{5b}$$

where

$$y_0(t') = \int^{t'} U_h(t'')dt'' + constant$$

is the unperturbed trajectory of a Lagrangian surface. In the absence of smoothing effects, the ablation front coincides with that Lagrangian surface whose equilibrium orbit overlaps the ablation front ($y = 0$) at time $t' = t$. The unperturbed trajectory of such a surface is given by

$$y_0(t') = \int_{t}^{t'} U_h(t'')dt'',$$

and the equation for the evolution of the ablation front $\left(\tilde{\eta} \right)$ can be written in the following differential form:

$$\partial_t\tilde{\eta} = \tilde{v}_{hy}[0,t] - U_h(t)\int_{-\infty}^{t} \frac{\partial \tilde{v}_{hy}}{\partial y}\left[y_0(t'),t' \right]dt'. \tag{5c}$$

TC3354
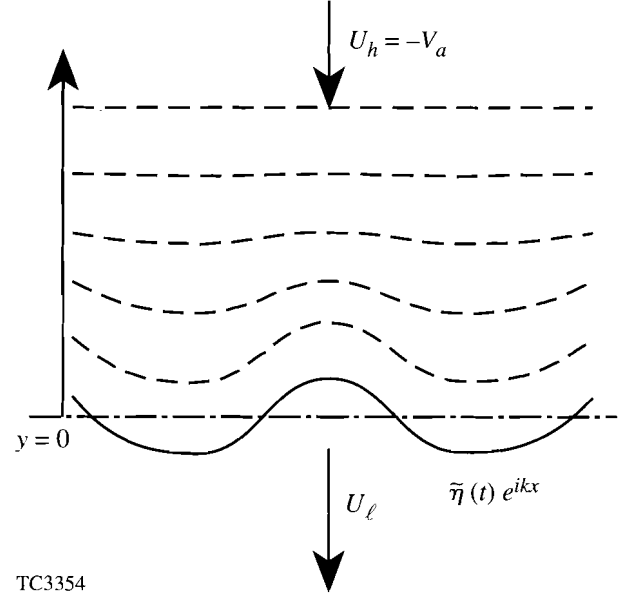
Figure 57.1
Deformation of a Lagrangian surface approaching the ablation front.

Once $\tilde{\eta}$ is known, a set of jump conditions relating the values of the physical quantities in the two regions can be derived by writing the time derivative of any perturbed quantity at the ablation front as $\partial_t\tilde{Q} = -\left(Q_h - Q_l \right)\partial_t\tilde{\eta}\,\delta(y)$ and integrating the incompressibility and conservation equations across the thin ablative layer. A short calculation yields

$$\tilde{v}_{hy} = \tilde{v}_{ly}$$

$$\left(\rho_h - \rho_l \right)\left(\partial_t\tilde{\eta} - \tilde{v}_{hy} \right) - U_h\tilde{\rho}_h + U_l\tilde{\rho}_l = 0$$

$$\tilde{v}_{hx} - \tilde{v}_{lx} + ik\tilde{\eta}\left(U_h - U_l \right) = 0 \tag{6}$$

$$\tilde{p}_h - \tilde{p}_l + \tilde{\rho}_h U_h^2 - \tilde{\rho}_l U_l^2 + g\left(\rho_h - \rho_l \right)\tilde{\eta} = 0.$$

The first of Eqs. (6) follows directly from the incompressibility condition $\nabla \cdot \tilde{v} = 0$. A better representation of the perturbation at the interface can be obtained by using an equation of state and calculating the jump in the energy.[2] This approach would greatly complicate the calculation. However, as shown in Appendix A, when the flow is subsonic

$$\left[U_h^2, U_l^2 \ll p_h/\rho_h, p_l/\rho_l \right],$$

the flow of internal energy across the interface has to be conserved and the incompressible result is recovered.

The next step is to solve Eqs. (4) in the two regions and then apply the jump conditions and the boundary conditions at $y = \pm\infty$. Since the heavy and light fluids extend to infinity and the instability is localized at the interface, the perturbation must vanish at $y = \pm\infty$.

The solution of the linearized equation in the heavy-fluid region (h) is greatly simplified by the following transformation: $y_h = y - \int_0^t U_h(t')dt'$. A straightforward calculation leads to the following form of the perturbed variables in region h:

$$\tilde{v}_{hy} = \tilde{u}_h(t)\exp(-ky_h) + \tilde{a}(y_h)$$

$$\tilde{v}_{hx} = \frac{i}{k}\frac{\partial\,\tilde{v}_{hy}}{\partial y_h}$$

$$\tilde{\rho}_h = \tilde{\rho}_h(y_h) \tag{7}$$

$$\tilde{p}_h = -\frac{\rho_h}{k^2}\frac{\partial^2\tilde{v}_{hy}}{\partial t\partial y_h} ,$$

where $\tilde{u}_h(t)$, $\tilde{\rho}_h(y_h)$, and $\tilde{a}(y_h)$ are arbitrary functions of t and y_h, and k is chosen to be positive $(k > 0)$. In order to satisfy the boundary conditions, $\tilde{a}$ and $\tilde{\rho}_h$ must vanish at $y_h \to \infty$. Since $\lim_{t\to\infty} y_h = \infty$, it follows that $\tilde{a}$ and $\tilde{\rho}_h$ asymptotically vanish in time. In our asymptotic stability analysis, we neglect all the quantities that do not grow in time. Thus, we set $\tilde{a} = 0$ and $\tilde{\rho}_h = 0$. Furthermore, because of the incompressibility condition and negative flow velocity, $\tilde{\rho}_h = 0$ at all times.

We apply the same procedure to the light-fluid region (l) and define the new coordinates $y_l = y - \int_0^t U_l(t')dt'$. The solution of the linearized equations in region l can be written in the following form:

$$\tilde{v}_{ly} = \tilde{u}_l(t)\exp(ky_l) + \tilde{b}(y_l) + \tilde{c}(y_l)f(t)$$

$$\tilde{v}_{lx} = \frac{i}{k}\frac{\partial\,\tilde{v}_{ly}}{\partial y_l}$$

$$\tilde{\rho}_l = \tilde{\rho}_l(y_l) \tag{8}$$

$$\tilde{p}_l = -\frac{\rho_l}{k^2}\frac{\partial^2\tilde{v}_{ly}}{\partial t\partial y_l} ,$$

where $\tilde{b}(y_l)$ and $\tilde{\rho}_l(y_l)$ are free functions of y_l that vanish

at $y_l \to -\infty$, and $\tilde{u}_l(t)$ is an arbitrary function of t. The functions $\tilde{c}(y_l)$ and $f(t)$ satisfy the following differential equations:

$$\left[\frac{d^2}{dy_l^2} - k^2\right]\tilde{c} + k^2\frac{\tilde{\rho}_l}{\rho_l} = 0$$
$$\tag{9}$$

$$\frac{df}{dt} = G(t) ,$$

where

$$G(t) \equiv g(t) - \frac{\partial U_l}{\partial t} . \tag{10}$$

The next step is to recognize that, using Eqs. (7) in Eq. (5c), the interface equation can be rewritten in the following form: $(\partial_t - kU_h)\tilde{\eta} = \tilde{v}_{hy}(y = 0, t)$.

After substituting Eqs. (7) and (8) into the jump conditions [Eqs. (6)] and using the differential form of the interface equation, the following ordinary differential equation for $\tilde{\eta}(t)$ is derived:

$$(\partial_t - kU_l)G^{-1}\Big\{(\partial_t - kU_l)(\partial_t - kU_h)\tilde{\eta}$$

$$+ A\big[kU_l(\partial_t - kU_h) + kg\big]\tilde{\eta}\Big\}$$

$$- Ak^2U_h\tilde{\eta} = 0 , \tag{11}$$

where

$$A \equiv (\rho_h - \rho_l)/(\rho_h + \rho_l)$$

is the Atwood number. For ICF applications, the appropriate ordering

$$U_h/U_l = \rho_l/\rho_h \sim (1 - A) << 1 \text{ and } g > \partial U_l/\partial t.$$

To lowest order in 1-A, the last term in Eq. (11) can be neglected, yielding

$$\Big\{(\partial_t - kU_l)(\partial_t - kU_h) + A\big[kU_l(\partial_t - kU_h) + kg\big]\Big\}\tilde{\eta} = 0. \tag{12}$$

Equation (12) can be further simplified by using the Ansatz

$$\tilde{\eta}(t) = \xi(t)\exp\left[\frac{3}{2}k\int_0^t U_h(t')dt'\right] \qquad (13)$$

and by neglecting other terms of order $(1-A) \ll 1$. After some straightforward manipulations, we obtain

$$\frac{d^2\xi}{dt^2} + k\left[Ag - \frac{1}{2}\frac{dV_a}{dt} - \frac{1}{4}kV_a^2\right]\xi = 0 , \qquad (14)$$

where g and V_a are functions of time with V_a the ablation velocity. Observe that, for steady equilibrium configurations, Eqs. (13) and (14) yield the normal mode solution for $\tilde{\eta} \sim \exp(\gamma t)$, with γ satisfying the dispersion relation

$$\gamma = \sqrt{\left(|kg|A\right) + \frac{1}{4}k^2V_a^2} - \frac{3}{2}|kV_a| . \qquad (15)$$

It is easy to recognize that the contribution of the second term under the square root is relevant only at very small wavelengths, where the mode is already strongly stabilized by convection [the last term in Eq. (15)]. Neglecting such a term in Eqs. (14) and (15) would cause only a small shift of the cutoff wave number $\left[\Delta k_c/k_c = 1/9\right]$, which is consistent with the order of magnitude of the previous approximations. After neglecting such a term, Eq. (15) reproduces the numerically derived growth rate of Ref. 3 with $\beta = 1.5$. Equations (13) and (14), which are valid for arbitrary unsteady configurations, can now be applied to the particular equilibrium obtained by temporally modulating the laser intensity. Consider a planar target of thickness d and density ρ_0 irradiated by a uniform laser beam. The periodically modulated laser intensity $\left[I(t) = I_0(1 + \Delta\sin\omega_0 t), \Delta \leq 1\right]$ induces an oscillating ablation pressure $P_a(t) = P_0\left(1 + \Delta_p\sin\omega_0 t\right)$ and ablation velocity $V_a(t) = V_{a0}\left(1 + \Delta_a\sin\omega_0 t\right)$ with $\Delta_p \lesssim \Delta$ and $\Delta_a \lesssim \Delta$. For simplicity, we assume that the ablation pressure and the ablation velocity are directly proportional to the laser intensity, and the ablation process develops on a very slow time scale compared to an oscillation period and the sound transit time through the target [$V_a \ll c_s, c_s$ is the sound speed]. Although the scaling $V_a \sim \sqrt{I} \sim \left[1 + \Delta\sin(\omega_0 t)\right]^{1/2}$ is more appropriate than a simple linear dependence, the numerical simulations show that the ablation velocity is almost insensitive to the oscillations in the laser intensity $\left(\Delta_a \ll 1\right)$ and

$V_a \simeq V_{a0}$. I_0 and P_0 are two slowly varying functions of time

$$\left[V_a/d < (1/I_0)(dI_0/dt) = (1/P_0)(dP_0/dt) \ll \omega_0 \sim c_s/d\right].$$

A simple estimate of the acceleration of the ablation front can be derived by solving the one-dimensional compressible fluid equations of Ref. 6 for a target accelerated by the ablation pressure. As shown in Appendix B, the time-dependent acceleration can be written in the following form:

$$g(t) = -\frac{dV_a}{dt} - L^{-1}\left\{\coth\left[\frac{s}{c_s}(d - \bar{y}_a)\right]\frac{s\hat{p}_a(s)}{\rho_0 c_s}\right\}, \qquad (16)$$

where L^{-1} denotes the inverse Laplace transform, s is the Laplace variable, and $\hat{p}_a(s)$ is the Laplace transform of the ablation pressure. The quantity $\bar{y}_a = \int_0^t V_a(t')dt'$ is the position of the ablation front in the Lagrangian frame of the moving target. In deriving Eq. (16), the slow ablation time scale $\left(\sim d/V_a\right)$ has been treated as an independent variable. A simple expression for $g(t)$ can be derived in the asymptotic limit $\left(d/V_a\right) > t \gg \left(d/c_s\right)$, yielding

$$g(t) = -g_0\left[1 + \alpha\sin\omega_0 t + \epsilon\cos\omega_0 t\right] , \qquad (17)$$

where $g_0 \equiv P_0/\rho_0 d_a$, $\alpha \equiv \Delta_p\left(\omega_0 d_a/c_s\right)\cot\left(\omega_0 d_a/c_s\right)$, and $\epsilon = V_{a0}\Delta_a\omega_0/g_0$, $d_a = d - \bar{y}_a$. A more accurate estimate of $g(t)$ (and of the parameters g_0, α, and ϵ) can be obtained by using a one-dimensional code. Later in this article we will use the one-dimensional hydrodynamic code $LILAC^7$ to derive g_0, α, and ϵ. However, Eq. (17) gives some physical insight into the relevant quantities that affect the oscillation amplitude in the target acceleration. In particular, large oscillations can be achieved for values of the modulation period shorter than the sound transit time through the target $\left[T_0 \equiv 2\pi/\omega_0 < d/c_s\right]$. Before proceeding further, it is important to define the range of validity of the stability model for the prescribed equilibrium. The oscillations in the ablation pressure propagate inside the target at the sound speed. Thus, the equilibrium parameters can be considered as uniform over a distance $\Delta y < c_s T_0$. The stability analysis, carried out for a uniform semi-infinite medium, can be applied to perturbations with sufficiently short wavelength $k\Delta y > 1$. It follows that a necessary condition for the validity of the stability model is $kc_s T_0 \gg 1$. For such wavelengths, Eq. (17) can be used in

Eq. (14) to derive the function $\xi(t)$. Thus, Eq. (14) can be written in the following form:

$$\frac{d^2\xi}{dt^2} - \gamma_c^2 \left[1 + q\sin(\omega_0 t + \phi)\right]\xi = 0 ,\qquad (18)$$

where $\gamma_c = \sqrt{A|kg_0|}$ is the classical growth rate,

$$q = \sqrt{\alpha^2 + 9\epsilon^2/4} ,$$

and

$$\phi = \tan^{-1}(3\epsilon/2\alpha) .$$

Notice that Eq. (18) is a Mathieu equation, whose solution has the form $\xi(t) = \sigma(t)\exp(\mu t)$, with $\sigma(t)$ being periodic with period ω_0. Using Eq. (13), the growth rate of the instability can be easily derived:

$$\gamma = -k\beta \frac{1}{T_0}\int_0^{T_0} V_a(t')dt' + \mu ,\qquad (19)$$

where $\beta = 1.5$ for the simplified stability model. However, when Eq. (19) is compared to the Takabe formula, we let $\beta = \beta^T = 3 - 4$. In order to find μ, one needs to numerically

solve Eq. (18) for one period of oscillation. Figure 57.2 shows the parameter μ, plotted versus the wave number k, for the following equilibrium parameters: $d = 20 \ \mu m$, $g_0 = 5 \times 10^{15}$ cm/s^2, $A = 1$, $\langle V_a \rangle = 7 \times 10^4$ cm/s, $c_s = 10^6$ cm/s, $T_0 = 0.3 \times 10^{-9}$ s, $\phi = 0$, and $q = 0, 2.5$, and 3.5. The validity of the stability model requires $\lambda = 2\pi/k << 20 \ \mu m$. For any value of q and ω_0, it is possible to identify intervals of the k axis, where $Re[\mu] = 0$. We denote such intervals as dynamically stabilized (DS) regions, and we emphasize the importance of ablative convection [see Eq. (19)] at shorter wavelengths. According to Eqs. (1) and (19), the short-wavelength modes are stabilized by convection, and the cutoff wave number is $k_c = gA/\beta^2 V_A^2$. It follows that an efficient dynamic stabilization can be achieved by choosing values of q and ω_0 that cause the first DS region to be located inside the interval $0 < k < k_c$. In Fig. 57.3, the growth rates derived from Eq. (19) for $q = 0, 2.5$, and 3.5 and $\beta = 3.5$ (as given by Takabe et al.[3]) are shown. Observe that as q increases, a better stabilization is induced at longer wavelengths, but shorter wavelengths can be destabilized ($q = 3.5$). This short-wavelength instability is driven by the oscillations in the acceleration, with the perturbation having the characteristic structure of an oscillatory mode with an exponentially increasing amplitude. For convenience, we denote these short-wavelength modes as "parametric instabilities."

Furthermore, when the mode wavelength is smaller than the density gradient scale length
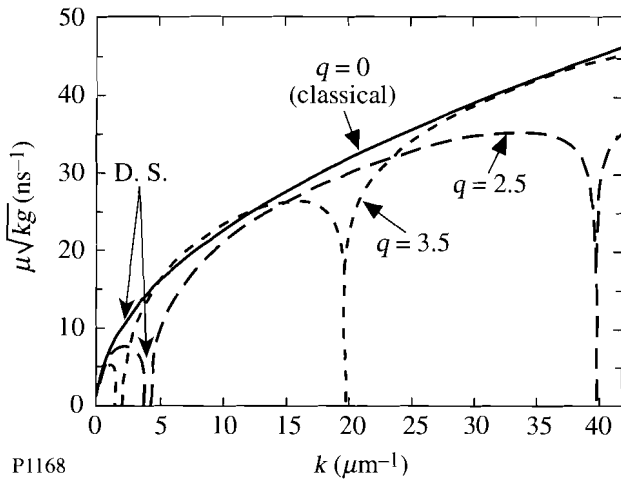
Figure 57.2

Plot of the instability drive term μ versus the mode wave number k for modulated ($q \neq 0$) and unmodulated ($q = 0$) laser intensity, assuming $d = 20 \ \mu m$, $g_0 = 5 \times 10^{15}$ cm/s^2, the Atwood number $A = 1$, $\langle V_a \rangle = 7 \times 10^4$ cm/s, $T_0 = 0.3$ ns, and $\phi = 0$.
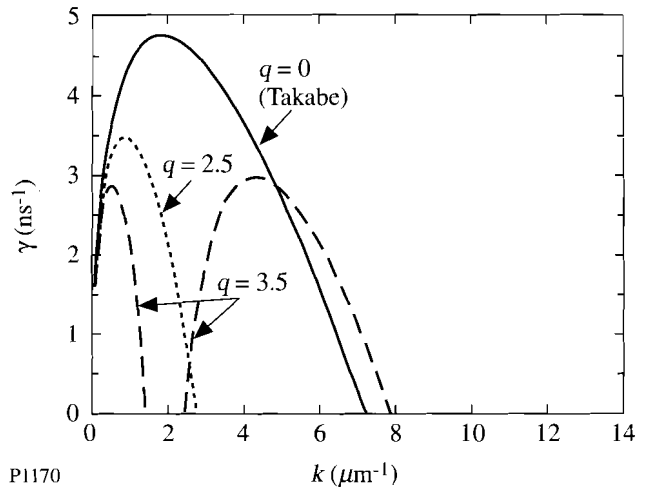
Figure 57.3

Plot of the instability growth rate versus the mode wave number k for modulated ($q \neq 0$) and unmodulated ($q = 0$) laser intensity, assuming the same equilibrium parameters as in Fig. 57.1.

$$\left[\delta = \left| (1/\rho) \, dp/dy \right|^{-1} \right],$$

the sharp boundary model is not valid and Eq. (19) cannot be used.

The results of the analytic theory have been compared with two-dimensional simulations obtained using the code *ORCHID*.[8] We have considered an 18-μm CH planar target irradiated by a uniform laser beam of wavelength 1.06 μm. The laser intensity is modulated in time with a period of 0.3 ns. The modulation amplitude is 100%, and the flat-top average intensity is 50 TW/cm^2. For an accurate comparison with the analytic stability theory, we derive the equilibrium parameters g, $\langle V_a \rangle$, and q from the one-dimensional code *LILAC*.[7] The result is $g = 4.5 \cdot 10^{15} \, \text{cm/s}^2$, $\langle V_a \rangle = 7 \cdot 10^4 \, \text{cm/s}$, $\delta = 1.5$ to 2 μm, $\phi = 0$, and $q = 3.5$ to 5.5. In the two-dimensional simulation, an initial single-wavelength perturbation evolves for 3 ns. Because of the short modulation period, the simulation shows no significant change in the foil isentrope with respect to the unmodulated case. Figure 57.4 shows a comparison between the linear growth rate derived from the simulation with the one given by Eq. (19). Three regions of the k-axis can be identified: (1) The long-wavelength region with $k < 0.2 \, \mu\text{m}^{-1}$, where the growth rate is virtually insensitive to the modulation of the laser intensity and very close to the classical value. (2) The intermediate wavelength region with $0.2 < k < 1$. For these values of the wave number, the dynamic stabilization is particularly effective. Observe that for $\lambda = 2\pi / k \approx 7 \, \mu\text{m}$ the mode is completely stabilized. (3) The short-wavelength region is defined as having a wave number $k > 1$. In this region $k\delta > 1$ and the effect of finite density-gradient scale length cannot be neglected. Notice that the simulation shows the presence of an unstable mode with wavelength $\lambda \approx 5 \, \mu$m. Using Eq. (19) beyond its limit of validity ($k\delta < 1$) and dividing γ_c^2 by $(1 + \theta k\delta)$ with $\theta < 1$, we would predict the existence of parametric instabilities at shorter wavelengths (Fig. 57.4). However, the structure of the perturbation observed in the numerical simulation does not clearly show the characteristics of a parametric instability. Furthermore, the cutoff wave number observed in the numerical simulation (with or without laser-intensity modulation) is much shorter than the one predicted by Eqs. (1) and (19). The stability of very-short-wavelength perturbations needs further investigation to determine an accurate value of the cutoff wave number.

The dynamic stabilization of the Rayleigh-Taylor instability in ICF targets was first observed in numerical simulations by J. Boris.[9] In this article we have shown the derivation of the linear stability theory for unsteady ablation fronts and the conditions for the dynamic stabilization of the ablative Rayleigh-Taylor instability. The growth rate of the instability has been calculated for a sinusoidal modulation of the laser intensity. It is shown that an appropriate modulation frequency and amplitude can stabilize a large portion of the unstable spectrum and significantly reduce the maximum growth rate.

P1200
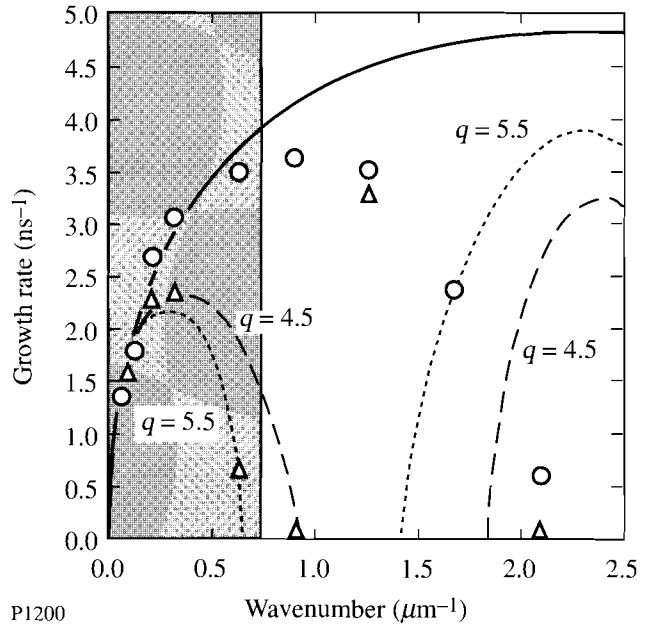
Figure 57.4

Comparison of the growth rate obtained from numerical simulations (with modulation $\triangle$ and without modulation $\bigcirc$) and the modified Eq. (19). Here, $d = 18 \, \mu$m, $g_0 = 4.5 \times 10^{15}$ cm/s^2, $\langle V_a \rangle = 7 \times 10^4$ cm/s, $T_0 = 0.3$ ns, $\phi = 0$, $A = 1$, $\beta = 3$, $\theta\delta = 1.5 \times 10^{-5}$ cm, $q = 5.5$ (dotted), $\beta = 4$, $\theta\delta = 0.3 \times 10^{-5}$ cm, $q = 4.5$ (dashed). The solid line represents the Takabe formula, and the shaded area represents the region with $\kappa\delta \leq 1$.

ACKNOWLEDGMENT

APPENDIX A: CONDITIONS FOR INCOMPRESSIBLE FLOW

A better model for the Rayleigh-Taylor instability can be obtained by replacing the incompressibility condition with an adiabatic equation of state. In the heavy- and light-fluid regions, where the velocity and density equilibrium profiles are uniform, the linearized adiabatic equation of state can be written as

$$\left(\partial_t + U_j \partial_y\right)\tilde{p}_j + \tilde{v}_{jy}\frac{dP_J}{dy} + \frac{5}{3}P_j \nabla \cdot \tilde{v}_j = 0, \quad \text{(A.1)}$$

where P_j represents the equilibrium pressure in the region j. Ordering $\partial_t \sim \sqrt{kg} \sim kU_h$ and using the momentum conservation equation, one finds that $\tilde{p}_j \sim \rho_j U_j \tilde{v}_j$, $\partial_y \tilde{p}_j \sim k\tilde{p}_j$, and $\left(dP_J/dy\right) \sim \rho g$. A simple comparison between the two terms in Eq. (A.1) yields

$$\frac{P_j \nabla \cdot \tilde{v}_j}{\left(\partial_t + U_j \partial_y\right)\tilde{p}_j + v_{jy}\left(dP_J/dy\right)} \sim \frac{1}{M_j^2}, \quad \text{(A.2)}$$

where $M_j^2 = 3\rho_j U_j^2/5P_j$ is the Mach number in region j. For subsonic flows ($M_j \ll 1$), Eq. (A.1) leads to the incompressibility condition $\nabla \cdot \tilde{v}_j \approx 0$. Although the flow in the two regions is clearly incompressible, at the interface between the fluids, where the equilibrium velocity and density have very sharp gradients, the conclusions derived above do not immediately apply.

A jump condition relating the energies in the two regions can be derived by integrating the adiabatic equation of state across the ablative layer. Following the work of Ref. 2, the calculation can be greatly simplified by using the conservative form of the equation of state:

$$\partial_t \left(\frac{1}{2}\rho v^2 + \frac{3}{2}p\right) + \nabla \cdot \left[\left(\frac{1}{2}\rho v^2 + \frac{5}{2}p\right)\mathbf{v}\right]$$

$$= \rho \mathbf{g} \cdot \mathbf{v} + I\delta\left(y - \tilde{\eta}\right), \quad \text{(A.3)}$$

where I is the power deposited at the ablation front. Integrating Eq. (A.3) and linearizing the variables yields the following jump condition for the fluid energy:

$$\partial_t \tilde{\eta}\left(\rho_h U_h^2 - \rho_l U_l^2\right) + \left(\frac{3}{2}\rho_h U_h^2 + \frac{5}{2}P_h\right)\tilde{v}_{hy}$$

$$-\left(\frac{3}{2}\rho_l U_l^2 + \frac{5}{2}P_l\right)\tilde{v}_{ly} + \frac{5}{2}\tilde{p}_h U_h$$

$$-\frac{5}{2}\tilde{p}_l U_l - \frac{1}{2}\tilde{\rho}_l U_l^3 = 0, \quad \text{(A.4)}$$

where all the quantities are calculated at the unperturbed ablation front ($y = 0$). In the derivation of Eq. (A.4), the incompressible results in the two regions have been used. The ordering for the perturbed quantities can be derived from the conservation equations

$$\partial_t \tilde{\eta} \sim \tilde{v}_{hy}/kU_h \qquad \tilde{p}_j \sim \rho_j U_j \tilde{v}_j \qquad \tilde{\rho}_l \sim \rho_h \tilde{v}_{hy}/U_l \quad \text{(A.5)}$$

Substituting the relations in Eq. (A.5) into Eq. (A.4) yields the following equation for the perturbed normal velocities at the ablation front:

$$\left[1 + O\left(M_h^2\right)\right]\tilde{v}_{hy} = \left[1 + O\left(M_l^2\right)\right]\tilde{v}_{ly} \quad \text{(A.6)}$$

For $M_j^2 \to 0$, Eq. (A.6) reduces to

$$\tilde{v}_{hy} = \tilde{v}_{ly}. \quad \text{(A.7)}$$

Observe that the latter can also be derived from the incompressibility condition ($\nabla \cdot \mathbf{v} = 0$) integrated across the ablative layer. Thus, the assumption of incompressible flow holds at the ablation front as well as at the two uniform regions on both sides of the interface when the Mach number is much less than unity, i.e., the flow is subsonic.

APPENDIX B: UNSTEADY EQUILIBRIUM OF AN ACCELERATED TARGET

The time evolution of the equilibrium of a planar target accelerated by an externally applied pressure $P_a(t)$ can be obtained by solving the one-dimensional fluid equations of Ref. 6. In ICF the accelerating pressure is induced by the laser irradiation. In order to simplify the calculation, we rewrite the fluid equations in a Lagrangian frame, and we neglect the reduction of the target thickness due to ablation. Let $y_T(\bar{y}, t)$ be the trajectories of the fluid elements and $\bar{y}$ the Lagrangian coordinate: i.e., the position of the fluid elements at time $t = 0$. As shown in Ref. 6, a linear wave equation describing the evolution of the fluid trajectories can be derived from the nonlinear set of equations

$$\frac{\partial^2 y_T}{\partial t^2} = c_s^2 \frac{\partial^2 y_T}{\partial \bar{y}^2}, \tag{B.1}$$

where c_s is the sound speed of the target at rest. We consider a planar target of thickness d ($0 \le \bar{y} \le d$) with the irradiated side at $\bar{y} = 0$ $[p(0,t) = P_a(t)]$. On the surface opposite to the laser $(\bar{y} = d)$, the external pressure is negligible $[p(d,t) = 0]$. These boundary conditions lead to the following equations for the trajectories at $\bar{y} = 0$ and $\bar{y} = d$:

$$\frac{\partial y_T}{\partial \bar{y}}(0,t) = 1 - \frac{P_a(t)}{\rho c_s^2} \qquad \frac{\partial y_T}{\partial \bar{y}}(d,t) = 1. \tag{B.2}$$

We let the laser irradiation start at time $t = 0$ (target at rest). Thus, the velocity at $t = 0$ is zero through the target:

$$\frac{\partial y_T}{\partial t}(\bar{y},0) = 0 \qquad y_T(\bar{y},0) = \bar{y}. \tag{B.3}$$

Equation (B.1), together with the boundary and initial conditions [Eqs. (B.2) and (B.3)], can be solved in the Laplace transform domain. A short calculation yields the following form of the Laplace transform (L) of the acceleration:

$$\hat{g}(s,\bar{y}) = \frac{\hat{P}(s)}{\rho c_s} s \frac{\cosh\left[\dfrac{s}{c_s}(d - \bar{y})\right]}{\sinh\left(\dfrac{sd}{c_s}\right)}, \tag{B.4}$$

where

$$g(\bar{y},t) = \frac{\partial^2 y_T}{\partial t^2} \qquad \hat{g}(\bar{y},s) = L\left[g(\bar{y},t)\right]$$

$$\hat{P}_a(s) = L\left[P_a(t)\right] \tag{B.5}$$

and s is the Laplace variable. Using the identity

$$\frac{1}{\sinh z} \equiv 2\sum_{n=0}^{\infty} e^{-(2n+1)z}$$

and taking the inverse transform of Eq. (B.4), we obtain the acceleration of the ablation front

$$g(0,t) = \frac{1}{\rho c_s}\left\{\frac{dP_a}{dt}\left[t - \frac{\bar{y}}{c_s}\right]\right.$$

$$\left. + 2\sum_{n=1}^{\infty} \frac{dP_a}{dt}\left[t - \frac{2nd}{c_s}\right]\Theta\left[t - \frac{2nd}{c_s}\right]\right\}, \tag{B.6}$$

where $\Theta(t)$ is the Heaviside step function. Focusing on an oscillating applied pressure induced by an oscillating laser intensity

$$\left[P_a(t) = P_0\left(1 + \Delta_p \sin \omega_0 t\right)\right],$$

we determine the asymptotic value of the acceleration after many periods of the oscillation $(t\omega_0 \gg 1)$. A short calculation yields

$$g(0,t) = \frac{P_0}{\rho d}(1 + \alpha \sin \omega_0 t), \tag{B.7}$$

where $\alpha = \Delta_p\left(\omega_0 d/c_s\right)\cot\left(\omega_0 d/c_s\right)$. The first term on the RHS represents the incompressible component of the acceleration. The other terms are induced by the oscillation in the applied pressure and vanish for $c_s \to \infty$, i.e., incompressible fluid. Observe that Eq. (B.7) yields the resonant condition for the oscillations, $\omega_0 d/\pi c_s = n$, where $n = 1, 2, \ldots$.

A more accurate expression of the acceleration can be obtained by retaining the effect of finite ablation velocity (V_a). For a subsonic ablation flow $(V_a \ll c_s)$ and times shorter than the ablation time $\left(2\pi/\omega_0 \ll t \ll d/V_a \right)$, the ablative flow can be treated as a perturbation of the equilibrium. Thus, the acceleration becomes

$$g(0,t) = g_0\left(1 + \alpha \sin \omega_0 t + \epsilon \cos \omega_0 t\right), \qquad \text{(B.8)}$$

where $g_0 = P_0/\rho d_a$, $d_a = d - \int_0^t V_a dt'$ is the target thickness at time t, and the ablation velocity has been taken proportional to the laser intensity $\left[V_a = V_{a0}\left(1 + \Delta_a \sin \omega_o t\right) \propto I(t)\right]$. For typical ICF parameters and oscillation periods of the order of hundreds of picoseconds, the term $\epsilon = \Delta_a V_{a0}\omega_0/g_0$ is much less than unity and can be neglected.

REFERENCES

1. Lord Rayleigh, *Scientific Papers* (Cambridge University Press, Cambridge, England, 1900), Vol. II, p. 200.

2. S. E. Bodner, Phys. Rev. Lett. **33**, 761 (1974).

3. H. Takabe, K. Mima, L. Montierth, and R. L. Morse, Phys. Fluids **28**, 3676 (1985).

4. H. J. Kull and S. I. Anisimov, Phys. Fluids **29**, 2067 (1986).

5. A. B. Bud'ko and M. A. Liberman, Phys. Rev. Lett. **68**, 178 (1992).

6. N. Rostoker and H. Tahsiri, Comments Plasma Phys. Cont. Fusion **3**, 39 (1977).

7. E. B. Goldman, Laboratory for Laser Energetics Report No. 16, 1973 (unpublished); J. Delettrez and E. B. Goldman, Laboratory for Laser Energetics Report No. 36, 1976 (unpublished).

8. R. L. McCrory and C. P. Verdon, *Computer Applications in Plasma Science and Engineering*, edited by Adam T. Drobot (Springer-Verlag, NY, 1991), pp. 291–325.

9. J. P. Boris, Comments Plasma Phys. Cont. Fusion **3**, 1 (1977).

Characterization of Laser-Produced Plasma Density Profiles Using Grid Image Refractometry

Grid image refractometry (GIR)[1] is proposed as a new technique for determining the two-dimensional density profiles of long-scale-length laser-produced plasmas such as will be generated on the OMEGA Upgrade. Interferometry, which has been successfully used to diagnose smaller plasmas, is unsuited to these plasmas because of problems associated with high fringe counts and fringe blurring.

The distinctive feature of GIR is that an optical probe beam is broken up into "rays" by being passed through a grid before traversing the plasma. The refraction angles of these rays are measured by imaging the plasma at two or more object planes and are integrated to yield the phase front. For cylindrically symmetric plasmas the density profile is then determined using Abel inversion. The feasibility of GIR is illustrated here by an analysis of an experiment carried out at KMS Fusion. The inferred density profile is substantially larger than any previously reported using interferometry and compares quite closely with *SAGE* hydrodynamic simulations.

Introduction

A fundamental concern in the study of laser-plasma interactions is the characterization of the plasma density profile that results when one or more laser beams irradiate a solid target. Knowledge of quantities including the plasma density, scale length, and temperature is especially important for the understanding of stimulated plasma physics processes, which can lead to a reduction in the overall laser-target coupling efficiency and/or the production of energetic electrons that potentially preheat the fusion fuel. In addition, it is desirable to compare experimental density profiles with predictions of hydrodynamic simulations in order to check the accuracy of computer modeling, especially in two dimensions where there is a sparsity of experimentally determined density profiles. Such comparisons might also provide insight into different models of thermal transport in the underdense corona.

The primary diagnostic of plasma density profiles has for many years been interferometry. Typically a short, 0.26-μm optical probe beam, derived from frequency quadrupling a Nd:glass laser, has been used to diagnose electron densities (n_e) up to $\sim 1 \times 10^{21}$ cm^{-3}. Generally the plasma is cylindrically symmetric, and Abel inversion (see, for example, Refs. 2–4) has been used to obtain the two-dimensional density profile. (Regrettably, very few such two-dimensional profiles have ever been published.) Notable results from interferometry have included the observation of profile steepening for 1-μm laser wavelengths,[5,6] where the high spatial resolution of interferometry has allowed scale lengths of ~ 1 μm to be measured. However, plasmas of current interest are less amenable to interferometric characterization for a number of reasons—the primary reason being their size. Exploding-foil plasmas with density scale length $L_n \sim 0.5$–1 mm have been produced on lasers such as NOVA[7] at the Lawrence Livermore National Laboratory and OMEGA[8] at the University of Rochester, and plasmas with true reactor scale lengths ($L_n \gtrsim 1$ mm) have recently been produced on NOVA using foams and high-density gas targets.[9] Interferograms of these plasmas would contain hundreds of fringes with spacing d_F (in the plane of the plasma) ranging from a few microns to around a millimeter. (The minimum spacing d_{min} is approximately equal to $2 F\lambda_p$, where F is the f number of the collection optics and λ_p is the probe wavelength, and the maximum spacing is comparable to the plasma scale length at the density corresponding to the outer fringe.) A large field of view would thus be required. Moreover, the fringe pattern can change very rapidly in time and be smeared out unless a sufficiently short probe beam is used.

To illustrate the limitations of plasma interferometry it is worth noting that, to the best of our knowledge, there are no reports in the literature of laser-produced plasma density profiles that have been determined from interferograms with over 20 fringes. (One fringe corresponds to a path length of 8 μm for a 0.25-μm probe and a plasma density of 10^{21} cm^{-3}.) In experiments in which small microballoon targets[5,6,10,11] or fiber tips[12,13] were irradiated with short laser pulses of 1-μm wavelength, ~ 5 fringes were typically observed. For 10-μm laser irradiation of somewhat bigger microballoons,[14] ~ 10 fringes were observed (after the subtraction of back-

ground fringes). In later experiments on the CHROMA laser, in which targets were irradiated at 0.5 μm and diagnosed with a four-frame holographic system,[15] 10–20 fringes were observed both for exploding-foil targets[16,17] and cryogenic microballoon targets.[18] Large fringe counts (up to ~75) were seen in other (unpublished) experiments on CHROMA and were often limited by blurring due to plasma motion and inhomogeneities. Of all the experiments cited here, only in the 10-μm case[14] were the two-dimensional density contours reported.

A further problem, not unique to interferometry but shared by all optical probing techniques, is that it is unrealistic to probe to (electron) densities higher than 1 (or possibly 2) $\times$ 10^{21} cm^{-3}. This density is independent of the plasma size but does depend (usually weakly) on the plasma shape. (Simple estimates of this density are given in Ref. 1.) While this allows probing to the critical density (n_c) for 1-μm radiation, information can generally be obtained only up to ~0.1–0.2 n_c for the short laser wavelengths ($\lambda \leq 0.35$ μm) of current interest. This is not a substantial concern since stimulated Raman scattering, one parametric process of great interest, occurs strongly at densities n_e ~ 0.1 n_c, and sometimes parametric processes at lower densities are also of interest.[19] Moreover, in the exploding-foil geometries that are often used for plasma physics experiments (see Ref. 8 and references therein), the density gradients tend to zero in the center of the plasma, the refractive limitation does not apply there, and higher densities can be diagnosed.

The long-scale-length plasmas generated on OMEGA[8] were diagnosed using a simple Schlieren technique in which the inner portion of the collection optic was blocked by a disk of f number F_s. Images of the plasma thus provided two contours of deflection angle, $\theta_{min} = \tan^{-1}(2F_s)^{-1}$ and $\theta_{max} = \tan^{-1}(2F)^{-1}$, where F is the f number of the collection optic. Comparison of these images with two-dimensional hydrodynamic/ray-tracing simulations using the code $SAGE$[20] showed good agreement, increasing confidence in the predicted density profiles. However, insufficient information was obtained to enable the density profile to be arrived at independent of simulations.

Grid image refractometry (GIR), as described in this article, is a more general Schlieren technique that can permit the independent experimental determination of density profiles. It permits, in principle, every contour of deflection angle (up to θ_{max}) to be obtained, thus providing sufficient information for the density profile to be inferred for plasmas with cylin-

drical symmetry. The term "refractometry" is used to describe the well-established technique whereby the refractive index $\mu(\mathbf{r})$ of an optical medium is inferred from the refraction angles $\Delta\theta(p)$ of a one- or two-dimensional set of probe rays parametrized by an impact parameter p. For the common case of cylindrical symmetry, Abel inversion of $\Delta\theta(p)$ to give $\mu(\mathbf{r})$ is straightforward.[3]

With GIR, the refraction angles are measured by passing an optical probe beam through a grid before it propagates through the plasma. An image of the grid is formed within the plasma with a relatively long depth of focus. The probe beam is effectively broken up into a two-dimensional set of "rays," one ray corresponding to each point on the grid. The collection optics are then used to form two or more images of the grid corresponding to different object planes within the plasma. The refraction angles of each ray (in the two orthogonal directions) may be determined simply from the difference between the apparent positions of the associated grid element in two object planes divided by the distance between those planes.

A wide variety of alternative methods for measuring the refraction angles have been reported. The technique closest to GIR is known as the "point-grid method" and is described by Vasil'ev.[21] Here a two-dimensional square grid is placed at an appropriate point in the path of the probe beam (after the medium being probed and near a focal plane of the imaging optics). Again, each grid point may be thought of as corresponding to a ray. By comparing the grid-point positions in the images taken with and without the optical medium present (the working and reference images, respectively), the ray deflection angles in each direction can be obtained from a knowledge of the parameters of the optical system. This was illustrated in Ref. 21 with a cylindrical medium (air flowing around a heated pipe) probed parallel to its axis. Essentially the same method was used by Gurfein et al. to measure the density profile of a very compressible fluid (near-critical CO_2) in the Earth's gravitational field,[22] and by Miyanaga et al.[23] and Benattar[24] to determine the density profile in the overdense region of a laser-produced plasma using x rays as the probing radiation. In Ref. 23, kilo-electron-volt x rays from a point source passed through a laser-irradiated spherical target, through a zone plate (used as a grid), and onto film; from the observed distortion of the image of the zone plate the ray refraction angles (up to 8 mrad) and hence the electron-density profile (10^{23}–10^{24} cm^{-3} with a scale length ~20 μm) were determined. A closely related technique, moiré deflectometry,[25] has also been demonstrated for x-ray

wavelengths.[26] Moiré deflectometry provides the ray refraction angles in one direction. A similar principle is embodied in Hartmann sensors used for the testing of optical surfaces.[27] Here the phase front is broken up into rays by being passed through a screen perforated with an array of holes; the ray deflection angles are then calculated from the ray locations in a far-field recording plane. Photothermal deflection provides yet another form of refractometry and has been used, for example, to diagnose the laser ablation of materials.[28] Here the whole-beam deflection is measured of a probe beam whose diameter is small in comparison with the scale length of the medium being probed. A separate shot is needed for each impact parameter, although a single shot suffices if the shape of the refractive index profile in the medium is known independently.

Interferometry may be considered to be a form of refractometry in which wave rather than geometrical optics are used to measure the refraction angle. The fringe spacing d_F determines the angle $\Delta\theta$ between the actual and reference wavefronts: for small angles, $d_F \approx \lambda_p/\Delta\theta$. In the approximation of weak refraction, integration of the refraction angle (or equivalently fringe counting) yields the phase front, although the case of strong refraction, where fringe distortion and ray crossing can occur, is more complicated.

One advantage of GIR is that the impact parameters of all probe rays are known. The point-grid and other methods described above are all diagnostics of the emerging wavefront, requiring the impact parameter of each ray to be inferred. Distortion of the fringe count and the apparent fringe positions due to small focusing errors (between the object plane of the probe beam and the symmetry axis of the irradiating laser) has been a major problem in plasma interferometry. GIR, however, is not sensitive to this error; indeed, in the data reduction reported here, no knowledge of the absolute location of any of the object planes was needed. For the diagnosis of long-scale-length plasmas, GIR can provide essentially the same density information as interferometry, but it does not suffer from the major drawbacks of interferometry. The micron spatial resolution of interferometry is lost, but this is not usually an important consideration for millimeter scale lengths.

In this article the GIR technique is illustrated by an experiment carried out at KMS Fusion on the CHROMA laser. Useful data were obtained from just one shot. From this data, it has been possible to extract very plausible density profiles that compare quite closely with two-dimensional hydrodynamic simulations using the code *SAGE*.

Experiment

The layout of the KMS experiment is shown schematically in Fig. 57.5(a). An incident laser of wavelength $\lambda_L = 527$ nm irradiated a 50-μm-thick solid CH disk target. The plasma was diagnosed using a short (~30-ps), 263-nm probe beam (of energy ~10 μJ) that was passed in the z direction through a copper-mesh grid, of spatial periodicity 50 μm × 50 μm, before passing through the plasma. The optical system relayed an image of the grid into the plasma, with unit magnification, onto the plane $z = z_0$ containing the incident laser axis, using a fairly slow, $f/10$, source lens. The refracted probe light was collected by an $f/2$ catadioptric reflector system[15] and relayed to a plane where it interfered with a reference beam and was recorded on holographic film. On reconstruction, an image of the grid was formed on the film plane with a magnification of ~10. The advantage of the holographic recording used was that by varying the position of the film plane, images were obtained corresponding to various different object planes (14 in total) within the plasma.
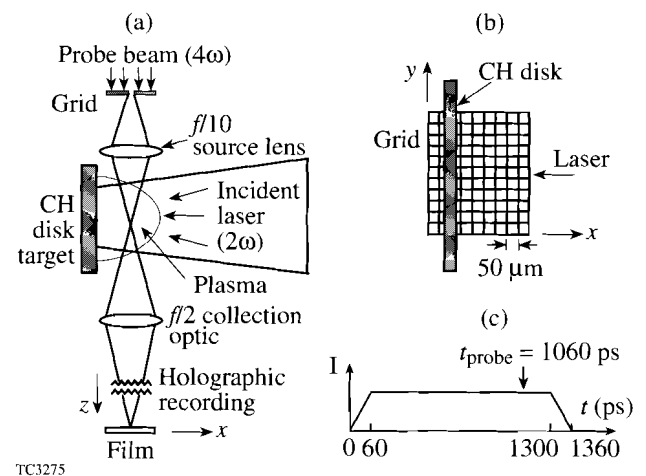
Figure 57.5

Schematic of GIR experiment carried out on the CHROMA laser at KMS Fusion. (a) Solid CH disk target, irradiated by a 527-nm laser. The plasma was diagnosed with a 263-nm probe beam with optics that relayed an image of a 50-μm grid into the plasma and then (holographically) onto film. (b) Grid as viewed by the probe beam. (c) Laser time history.

The grid location with respect to the disk target is shown in Fig. 57.5(b). [Unfortunately, due to a lack of comparison images from a plasma-free reference shot, the absolute location of the disk in the (x,y) plane and the y coordinate of the laser axis were not known.] The (x,y,z) coordinate system shown in Figs. 57.5(a) and 57.5(b) is used consistently throughout this article; thus the cylindrically symmetric *SAGE*

simulations are carried out with x the symmetry axis and y the radial direction.

The temporal history of the laser pulse, as modeled by SAGE, is shown in Fig. 57.5(c). It is essentially a flat pulse of 1.3-ns duration with the probe beam timed at 1.06 ns. The beam energy was 107 J and the beam diameter on target was d_0 ~ 400 μm. Since the exact on-target spatial profile was not known, simulations were carried out for two spatial shapes that should bracket the actual profile: (a) a flat profile truncated to zero at radius $d_0/2$, giving a laser intensity of 6.5×10^{13} W/cm^2 for $d_0 = 400$ μm, and (b) a Gaussian profile whose intensity falls to 10% of the peak at a radius $d_{90}/2$, truncated to zero at this radius, giving an on-axis intensity of 1.1×10^{14} W/cm^2 for $d_{90} = 400$ μm. (Simulations were also carried out with different spot diameters.)

Three representative images, resulting from holographic reconstruction and corresponding to different object planes, are shown in Fig. 57.6. The first image corresponds to an object plane closer to the grid ($z < z_0$) and the third to a plane closer to the collection optic ($z > z_0$). The left portion of the dark band is due to obscuration by the unirradiated target, which could present a width of >50 μm if not perfectly aligned. The right portion results from probe rays that are incident close to the target surface and are refracted through angles outside the $f/2$ cone of the catadioptric optic. The images have slightly different magnifications due to their different object planes.

A number of features may be seen in Fig. 57.6. The positions of the grid points behind the target appear to be unchanged from image to image. This is not surprising since simulations show that no significant plasma is expected to form behind the target. On the other hand, the grid points to the right of the target, especially those close to the target, shift to the right with increasing z. This shift is greater for grid points near the laser axis, resulting in a change of curvature between images that can be best perceived in the vertical line just to the right of the dark band. Image quality degrades toward the edge of the image, some (ideally square) grid images degrade into double images, and interference effects between neighboring grid elements are apparent. In image (c) there appears to be a caustic on the right edge of the dark band, pointing to an overlap of grid-point images resulting from strong refraction. In all the images there appears to be an up-down skew to the vertical lines: i.e., those on the right do not appear to be quite parallel to those behind the target. This is unlikely to result from an up-down asymmetry in the expanding plasma since the distortion persists (and may even be greatest) on the far right where the plasma density is the lowest. Rather, the distortion is presumed to be due to a nonuniformity in the grid or an aberration in the optical system. Qualitatively, then, most features of the images may be understood; however, digitization of the images is essential to enable GIR to provide quantitative information.

The principle of GIR is illustrated schematically in Fig. 57.7(a). Here, a set of parallel probe rays is shown incident on the plasma, one per grid element. A typical ray, which would appear to come from point P if the plasma were absent, is refracted through an angle θ_x in the (x,z) plane [and a corresponding angle θ_y in the (y,z) plane]. Depending on the

(a)   (b)   (c)
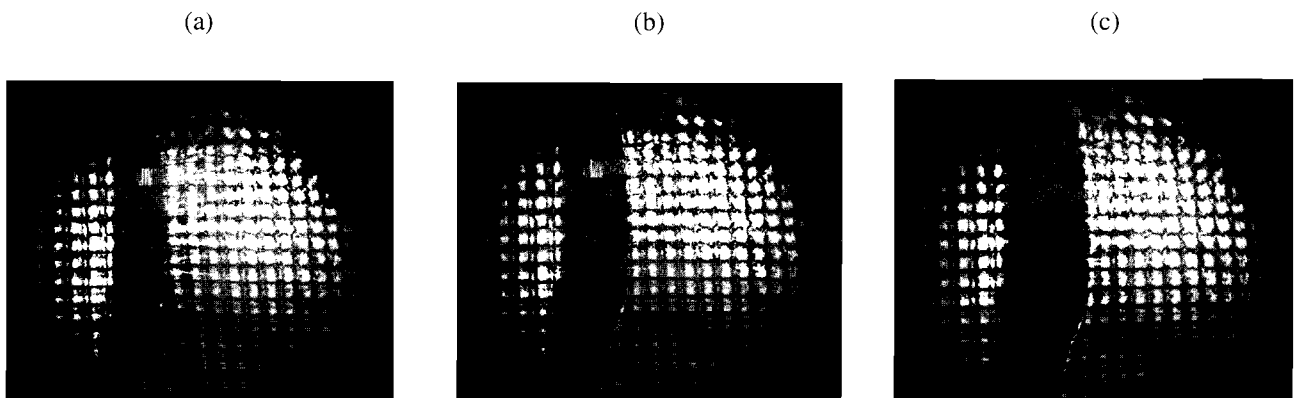
TC3089

Figure 57.6

Images after holographic reconstruction at object planes (a) $z = 200$ μm, (b) $z = 600$ μm, and (c) $z = 800$ μm, in the same orientation as Fig. 57.5(b). Image (b) corresponds approximately to the center of the plasma. The dark band is due partially to obscuration by the CH target and partially to refraction of probe rays close to the target surface through angles outside the $f/2$ cone of the collection optics.
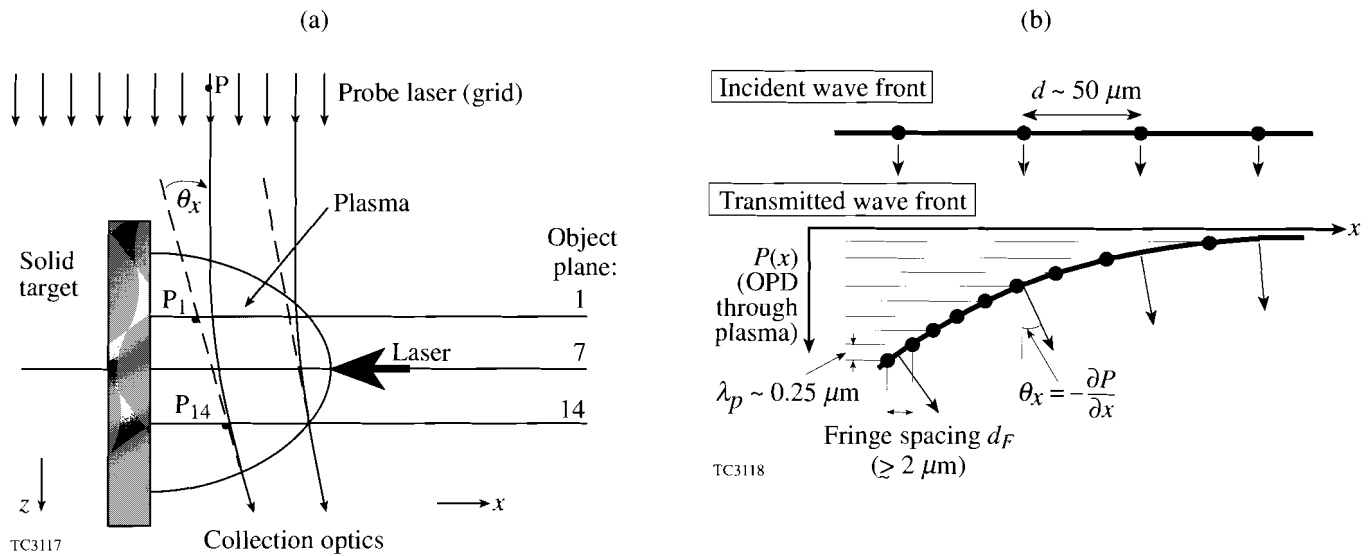
(a)

(b)

Figure 57.7

(a) Principle of GIR. The apparent position of each probe ray P must be measured for at least two object planes, thereby enabling its deflection angles (θ_x in the x, z plane and θ_y in the y, z plane) to be obtained. (b) Relationship between GIR and interferometry (simplified to omit effects due to strong refraction). In GIR the wavefront $P(x)$ transmitted through the plasma is sampled at uniform intervals (the grid spacing d) in x while, with interferometry, data are obtained each time $P(x)$ changes by the probe wavelength λ_p.

object plane being imaged, the ray will appear to come from points such as P_1 or P_{14}. Provided that images are obtained in a minimum of two such object planes, the angles θ_x and θ_y are calculated very simply by dividing the measured differences of x and y coordinates in the images by the (known) distance between the object planes.

In the present experiment, in which the use of holographic recording provided images for multiple object planes, a more accurate determination of θ_x and θ_y was possible using a least-squares fit to the positions P_i. However, holography shares many of the problems of interferometry, in particular the need for short exposure times to avoid blurring the interference pattern, so that for applications to plasmas with longer scale lengths, such as plasmas anticipated for the OMEGA Upgrade, holography is best avoided. A preferable system would include, instead, a means for directly recording two (or more) images on each shot corresponding to different object planes. This could be accomplished by the insertion of a beam splitter near the film plane of Fig. 57.5(a) and the use of two cameras focused to different object planes. It should be noted that the ability of the holographic system to handle multiple, time-staggered probe pulses[15] would be lost with the GIR system proposed here, which would accommodate a single probe pulse.

The close relationship between GIR and interferometry is illustrated in Fig. 57.7(b) for the case where curvature of the ray path through the plasma can be neglected. (This approximation will be discussed in the following two paragraphs.) Here, the plasma converts a plane incident wave front into a curved transmitted wave front $P(x)$, where $P(x) = \int (1 - \mu)ds$ is the optical path difference through the plasma of a ray entering the plasma with impact parameter x. [The refractive index μ in the plasma is equal to $\left(1 - n_e/n_{cp}\right)^{1/2}$, where n_{cp} is the critical electron density corresponding to the probe wavelength, and s measures distance along the ray path.] The difference between the two techniques lies in the way this wave front is sampled. With GIR, sampling occurs every grid spacing d in x; with interferometry, data are obtained every time $P(x)$ changes by λ_p. (It is assumed that, with interferometry, it is feasible to extract only the fringe locations and not information based on intensity variations between fringes.) With GIR the phase-front normal, $\left(\theta_x, \theta_y\right) = \left(-\partial P/\partial x, -\partial P/\partial y\right)$, is measured directly; with interferometry, θ_x is given from the local fringe spacing d_F by $\theta_x = \tan^{-1}\left(\lambda/d_F\right)$. With GIR the phase P is obtained by integrating θ_x along x from vacuum, or by integrating θ_y along y; with interferometry, this integration is performed simply by counting fringes from the outermost fringe. The maximum plasma density that is in principle accessible is

14

the same in both cases, and a function solely of the f number of the collection optic. In both cases the field of view should be sufficient, to allow a clear zero for the integration of (θ_x, θ_y) in GIR and to allow for the identification of the first fringe in interferometry.

The picture shown in Fig. 57.7(b) is slightly simplified since it is really the emerging phase front as projected back to the appropriate object plane that is imaged onto the plane in which the interferogram is formed. As with grid images such as those of Fig. 57.6, interferograms are dependent on the object plane. This problem has been known for a long time[3,12] and has led to considerable difficulties in the interpretation of experimental interferograms, especially those showing profile steepening and other features around the critical density for 1-μm laser irradiation.[13,29] The problem is minimized by focusing on the plane containing the plasma axis,[3] and it is notable that the difficulties associated with focusing conventional interferometers to the necessary accuracy led to the introduction of holographic interferometry for laser-produced plasmas[30] because then, as with the GIR experiment described in this article, the object plane can be varied during reconstruction.

Even correct focusing is not a complete solution to the problem of reconstructing the density profile. Regardless of whether GIR or interferometry is being used, further errors are introduced by the Abel inversion procedure. This is always carried out in a two-dimensional plane, usually perpendicular to the irradiating laser axis (assumed to be an axis of symmetry). Usually it is assumed, with some justification,[3] that $P(x)$ corresponds to an integral of $(1-\mu)$ along a straight-line path in this plane. Refraction in this plane could be included exactly if the experimental measurement were the refraction angle as a function of impact parameter,[31] but this is not usually the case. However, significant error can arise due to refraction out of the plane of Abel inversion, the dominant refractive effect for steep density profiles, and it may then be preferable to simulate the interferogram directly.[17] Fortunately, Abel inversion is applicable to a good approximation to the experiment reported in this article and to long-scale-length plasmas in general since the lateral displacement of the ray is smaller than the plasma-density scale length (see Ref. 1, Appendix B).

Data Reduction

The data reduction proceeded in two stages: first, the refraction angles (θ_x, θ_y) were extracted; then the plasma density was obtained under the assumption of cylindrical symmetry.

The first stage is illustrated in Fig. 57.8; a typical hand-digitized grid image [corresponding to Fig. 57.6(b)] is shown in Fig. 57.8(a). (The grid-point centers were located by eye on the original photographs and entered into a computer using a digitizer pad.) After the photographs were digitized, it was discovered that two were identical. Their digitizations are superposed in Fig. 57.8(a). The close correspondence indicates that the photographs could be repeatably digitized, even though the image quality and contrast degraded around the periphery. Even though diffractive effects were evident in the images, the locations of the cell centers could be accurately found. In order to register all images on a common coordinate system (x',y'), it was assumed that three grid points, labeled A–C and easily identified in each image, were invariant— points A and B because they were behind the target and point C because it was sufficiently far to the right of the plasma. In this way the varying orientations and translations of the images as placed on the digitizer pad and the varying magnifications of the images could be accounted for. At a later stage it became apparent that the experimental field of view was too small and the ray through point C must have had a non-zero deflection angle. A value of $\theta_x = 0.75°$ was adopted as a plausible deflection for this point (see later). A more accurate registration of the images would obviously have been possible had comparison images been obtained from a reference, plasma-free shot.

Each point in each image was assigned unique (i,j) coordinates. For each (i,j) point it was then possible to plot the apparent (x',y') position in the image as a function of object plane position z and extract the slopes (θ_x, θ_y) using a least-squares fit [see Fig. 57.8(b)]. These angles were obtained without knowing which value of z corresponded to the center of the plasma; it was sufficient to know the spacing between images ($100\,\mu$m). With the exception of a few points around the periphery of the image where the probe-beam intensity was weak, good straight-line fits were obtained for all (i,j) points. Results with nearly the same accuracy could evidently have been obtained from just two images separated by ~1 mm.

The (x',y') coordinates of Fig. 57.8(a) are arbitrary, and for comparison to be made with *SAGE* simulations a translated coordinate system (x,y) was defined. The choice $x = x'-100\,\mu$m enabled the closest comparison to be made with the simulations below, and the choice $y = y'-850\,\mu$m was made so that $y = 0$ corresponded to the axis of symmetry as could best be determined experimentally. The uncertainty in the horizontal shift would of course have been removed if
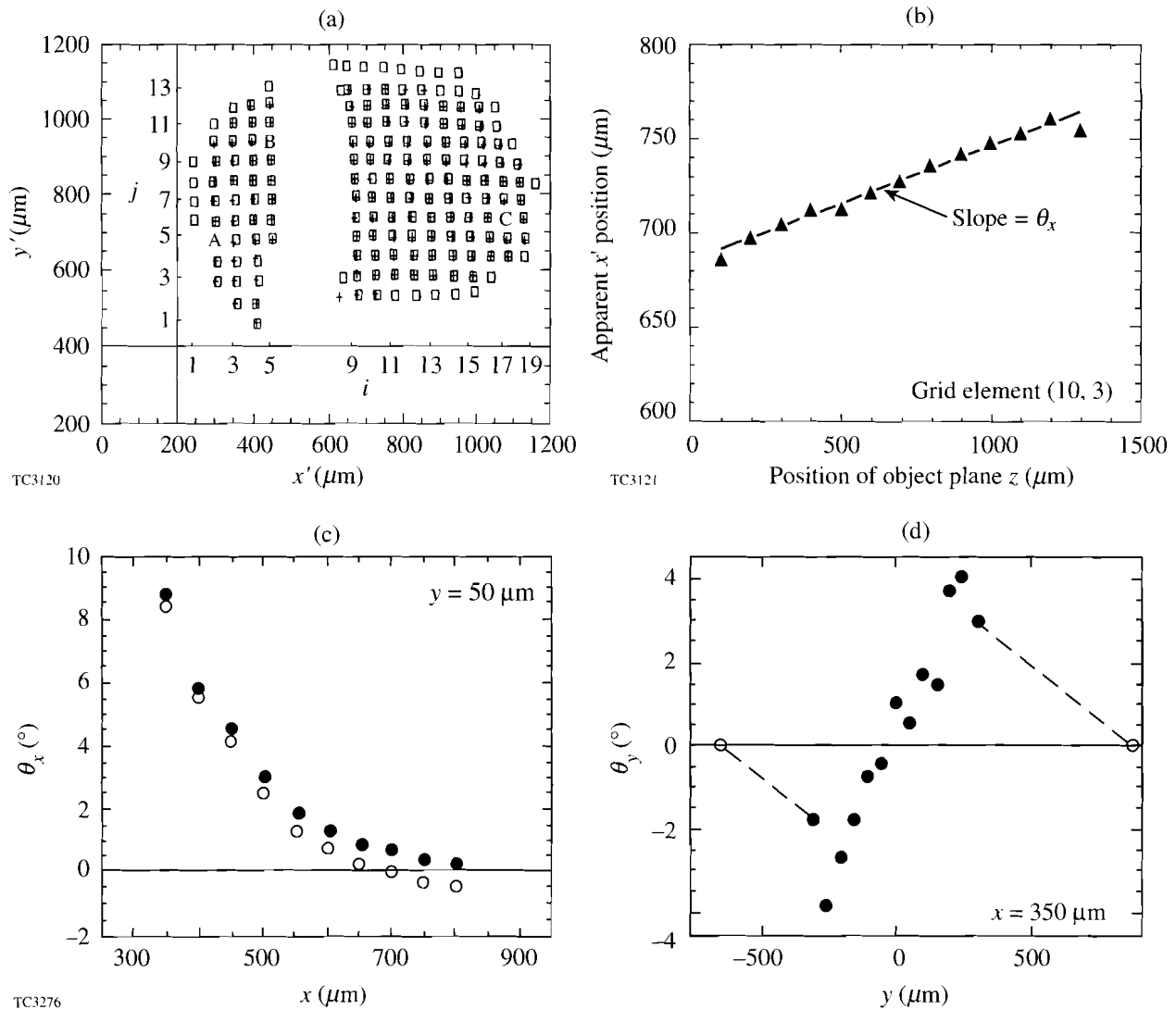
Figure 57.8

Extraction of deflection angles from the grid images. (a) Typical digitized image, with two identical images superposed to illustrate the repeatability of the digitization. All 13 images were then scaled to a common coordinate system $\left(x', y' \right)$ using reference points A, B, and C. (b) Apparent x' position as a function of object plane position z for a typical grid element. A least-squares fit to the 13 points yields the slope of the ray, θ_x. (c) Lineout of θ_x as a function of x for $y = 50\ \mu m$. Solid (open) points were obtained assuming $\theta_x = 0.75°$ (0°) at reference point C. (d) Lineout of θ_y as a function of y for $x = 350\ \mu m$. Dashed lines indicate extrapolations used outside the experimental field of view.

reference images (of the target and grid in the absence of a plasma) had been available.

Typical lineouts of $\theta_x(x)$ and $\theta_y(y)$ are shown in Figs. 57.8(c) and 57.8(d), respectively. The θ_x lineout, taken approximately along the laser axis, shows why it was necessary to assign a finite deflection angle to point C: the resulting curve (solid circles) asymptotes to zero. If point C were assumed to have no deflection angle (open circles), unphysical negative values of θ_x would be found at large x. The largest standard deviation obtained from least-squares straight-line fits is $\pm 0.25°$ in θ_x

for the point with $\theta_x \approx 9°$, and $\leq \pm 0.5°$ for the leftmost and rightmost solid θ_y points. The standard deviation for all other points is less than the symbol size used in the plots. The θ_y lineout, taken at the smallest x (350 μm) at which data existed, reveals an inadequate experimental field of view in the y direction: while θ_y should tend to zero at large |y|, the maximum θ_y is observed near the edge of the image. (Further discussion of this problem follows.)

Contour plots of θ_x and θ_y are shown in Fig. 57.9, where experimental and simulated contours are compared. All con-
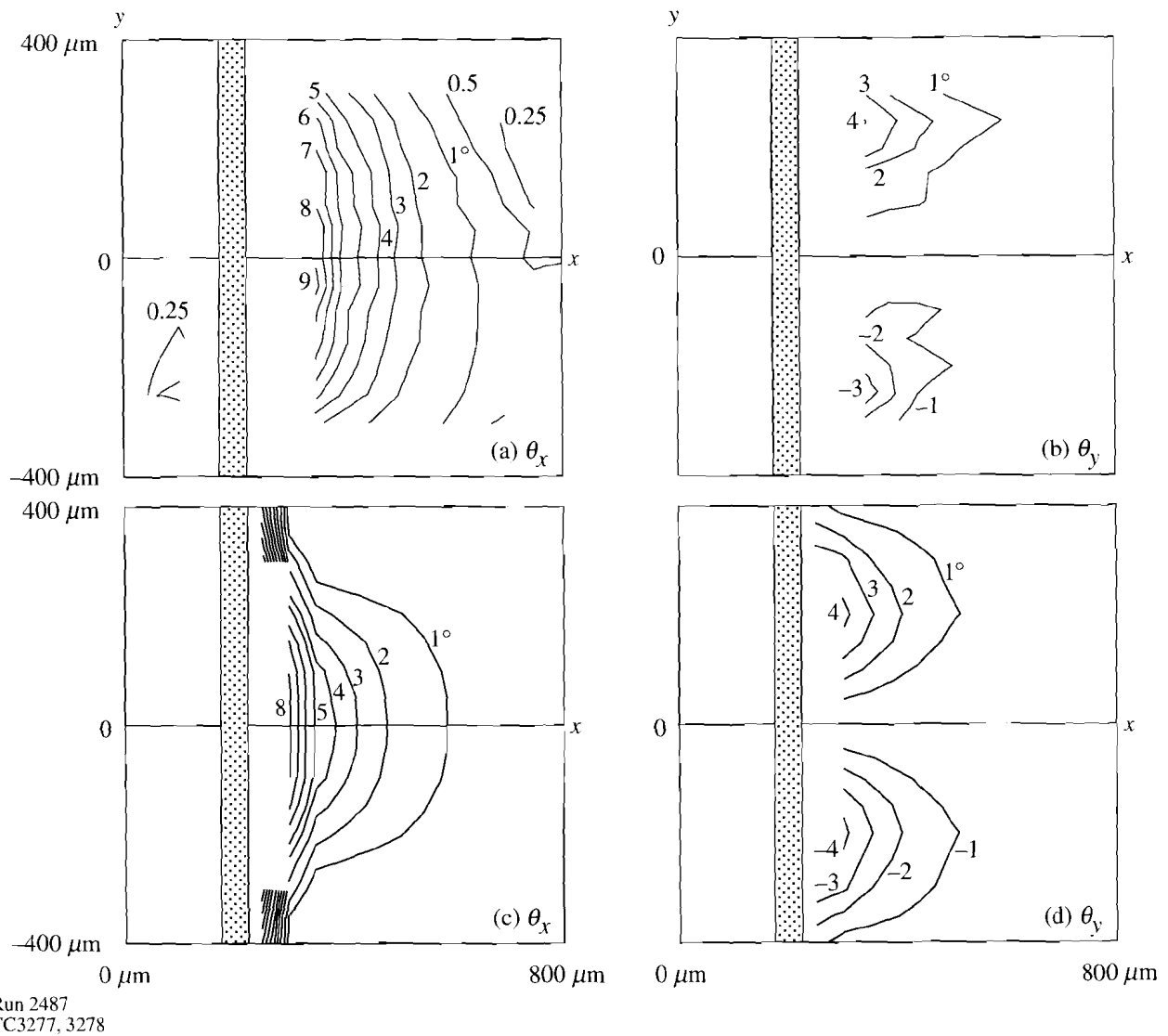
Figure 57.9

Comparison of measured and calculated refraction angles: (a) θ_x and (b) θ_y from GIR; (c) θ_x and (d) θ_y from SAGE. The actual positioning of the experimental data relative to the initial solid target (shaded area) and the x axis is unknown. The simulations were performed in cylindrical geometry with x and y the axial and radial coordinates, respectively.

tours are in 1° intervals, except for two additional experimental contours at 0.5° and 0.25°. Reasonable agreement is found for many features of the contours. The main difference appears to be that the experimental contours extend further in the radial (y) direction. The experimental asymmetry seen especially in the 0.5° and 0.25° contours is probably not due to a plasma asymmetry, as discussed above. The least-squares fitting procedure was also applied to the undistorted grid points behind the target, and the 0.25° contour behind the target thus indicates the error associated with the digitization process as applied to the current experimental data.

The second stage of data reduction is illustrated in Fig. 57.10. The phase P was calculated in two ways: integrating θ_x along x to yield P_x, and integrating θ_y along y to yield P_y. Ideally, both P_x and P_y should be equal. However, as observed above, values of θ_y were not available at sufficiently large y, and integration of θ_y from the largest y for which data existed ($y = y_{edge}$, say) yielded values of P_y that in some cases were as low as $0.5 P_x$. To resolve this problem, a constant was added to each such integral to represent the integral from y_{edge} to ∞, such that P_y matched P_x at $y = 0$.
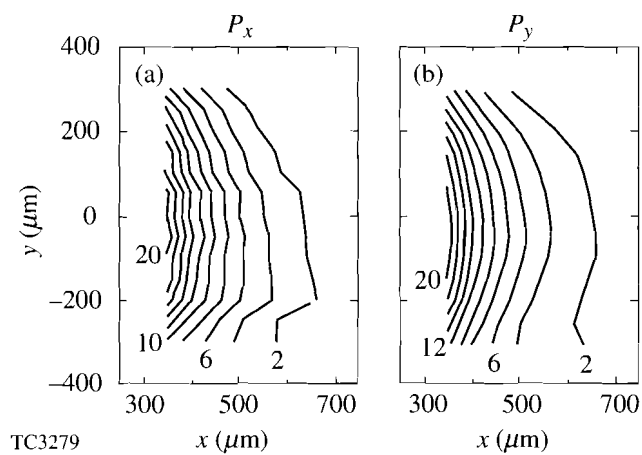
TC3279
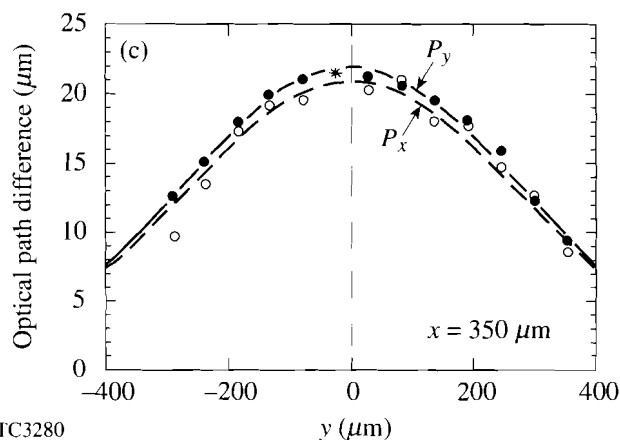
TC3280
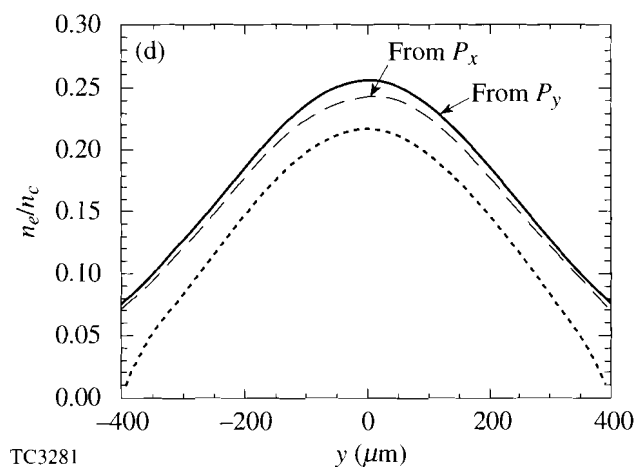
TC3281

Figure 57.10

Extraction of density profile from θ_x and θ_y. (a) and (b): Contours of phase (optical path difference in microns) obtained by integrating θ_x with respect to x to obtain P_x and θ_y with respect to y to obtain P_y. For each value of x, a Gaussian was found to provide a good fit to the y dependence of P_x and P_y. (c) P_x (open circles) and P_y (solid circles) as functions of y for $x = 350$ μm, together with Gaussian fits about $y = 0$. P_y was forced to equal P_x at the maximum (asterisk) by the appropriate choice of dashed line in Fig. 57.8(d), but the x and y data were otherwise totally independent. (d) Electron-density profile from Abel inversion of the Gaussian fits to P_x and P_y. The dotted curve results from truncating the Gaussian for P_x to zero at $|y| \geq 400$ μm.

Contours of P_x, for which the field of view was (just) adequate, and P_y, adjusted as described, are shown in Figs. 57.10(a) and 57.10(b). The contours have been forced to agree at $y = 0$, but otherwise their shapes correspond very closely. This is notable since, aside from the adjustment, P_x and P_y have been obtained independently from the x and y coordinates of the digitization. This correspondence confirms the self-consistency that the digitized data should possess. It is also worth noting that an interferogram could be simulated simply by plotting contours every 0.26 μm (the probe wavelength) in P rather than every 2 μm. The fringe count at the center would be 80, substantially more than has previously been reported for the interferometric determination of a laser-produced plasma-density profile.

The correspondence between P_x and P_y is shown in Fig. 57.10(c) for the line $x = 350$ μm (the line corresponding to the highest densities that could be probed). Solid circles correspond to P_y and open circles to P_x. The asterisk indicates

the point at which P_y was forced to equal P_x. The solid and dashed lines indicate least-squares Gaussian fits to P_y and P_x, respectively. These fits were obtained for each line on the grid, and good symmetry was found with respect to $y = 0$. These curves were then Abel-inverted to yield the density profiles shown in Fig. 57.10(d). By fitting the phase data to smooth curves (Gaussian and truncated Gaussian), problems associated with the differentiation of experimental data were avoided.[4] It is questionable whether the Gaussian fits of Fig. 57.10(c) should be extrapolated to ∞ [leading to the upper curves of Fig. 57.10(d)] or truncated to zero at $|y| = 400$ μm (giving the dotted curve) since $|y| = 400$ μm was in any case outside the field of view. It is likely that the actual density profile lies somewhere in between. This uncertainty was the greatest for the value of x shown here, but even so it did not make a large difference in the density of ~ 0.25 n_c obtained for $y = 0$. The Abel inversions were carried out numerically in all cases, although the Gaussian inverse is known analytically to be a Gaussian.

One interesting difference between the contours of P_x and P_y shown in Fig. 57.10 may be noted: the P_x contours include some fine structure, correlated along horizontal lines, similar to the fine structure in the contour plot of θ_x [Fig. 57.9(a)]. Integration of θ_x along horizontal lines preserves this structure, whereas integration of θ_y perpendicular to these lines evidently does not. It is probable that this structure is physical and results from hot spots in the laser, as similar structures can be seen in interferograms obtained on the CHROMA laser reported in Ref. 32 (and reproduced in Ref. 17). Also, the experimental determination of θ_x is carried out independently for each grid point, so that it would be hard to explain the θ_x correlations seen in Fig. 57.9(a) as noise resulting from the data-reduction process.

Comparison with Simulations

Contours of electron density resulting from the Abel inversion are compared with the predictions of five SAGE simulations in Fig. 57.11. The simulations included the SESAME equation of state,[33] a multigroup diffusion model for radiation transport (which led to some minor heating of the target surface as seen near $y = 400$ μm),[34] and ray tracing for the incident laser.[20] The experimental contours, shown as heavy lines, are the same in each case: the dashed lines corresponding to extrapolation of the Gaussian fit for $P(y)$ to infinity and the solid lines to truncation at $|y| = 400$ μm. As discussed above, the difference between these lines should be indicative of the experimental uncertainty associated with the restricted field of view in the y direction. In each figure it is the contours
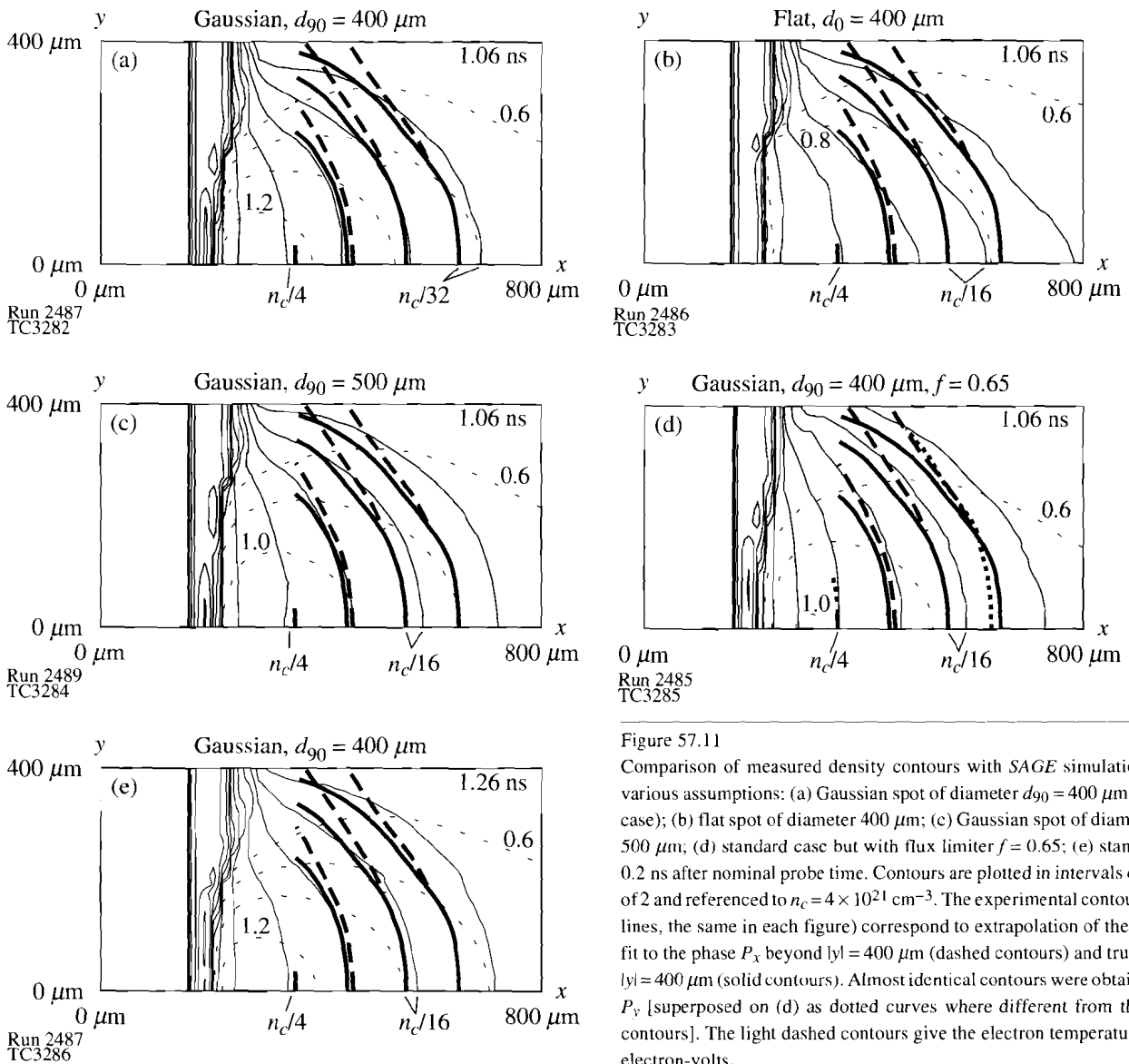
Figure 57.11

Comparison of measured density contours with SAGE simulations under various assumptions: (a) Gaussian spot of diameter $d_{90} = 400$ μm (standard case); (b) flat spot of diameter 400 μm; (c) Gaussian spot of diameter $d_{90} = 500$ μm; (d) standard case but with flux limiter $f = 0.65$; (e) standard case 0.2 ns after nominal probe time. Contours are plotted in intervals of a factor of 2 and referenced to $n_c = 4 \times 10^{21}$ cm^{-3}. The experimental contours (heavy lines, the same in each figure) correspond to extrapolation of the Gaussian fit to the phase P_x beyond $|y| = 400$ μm (dashed contours) and truncation at $|y| = 400$ μm (solid contours). Almost identical contours were obtained using P_y [superposed on (d) as dotted curves where different from the dashed contours]. The light dashed contours give the electron temperature in kilo-electron-volts.

based on P_x that are plotted. The contours based on P_y were almost identical, as is seen in Fig. 57.11(d) where they are superposed, where different, as dotted curves.

Starting with Fig. 57.11(a), for a "standard" simulation with a Gaussian focal spot of diameter $d_{90} = 400$ μm, agreement with experiment is for the most part very close. As discussed above, the lack of an experimental determination of the target location relative to the grid allowed the contours to be moved in the x direction (through the transformation from x' to x) to provide the best fit. However, the contour spacing and shapes match remarkably well. A minor discrepancy is seen at the $n_c/32$ contour, where the experimental contour interval (between $n_c/16$ and $n_c/32$) seems to be smaller than predicted. Since this could be related to the choice of 0.75° assumed for θ_x at the reference point C, it is impossible in the absence of a reference shot to say whether or not this discrepancy is real. The main discrepancy is seen at the larger radii, where the experimental plasma seems to have a greater radial extent, even if the solid experimental contours are used. The greatest discrepancy is seen at radii beyond 300 μm, the largest radius in the experimental field of view. It is of interest to ascertain whether or not such a discrepancy could yield insight into physical processes such as thermal transport, and it is worth noting that a similar motivation for comparing simulated and experimental interferograms is found in Ref. 17. The following plots of Fig. 57.11 are included to show that there could be a variety of explanations for the discrepancy aside from thermal transport modeling.

The simulation of Fig. 57.11(b) assumes a flat focal spot, also of diameter 400 μm. The predicted blowoff in this case is strongly peaked in the direction of the target normal, and the match at low densities, especially around $n_c/32$, is much poorer. The reason for the different coronal shape may be readily understood from the temperature contours, shown as light dashed lines. For the flat focal spot the plasma temperature and expansion are fairly uniform in y, and the expansion velocity is initially in the $+x$ direction. Not until the combination of a rarefaction wave and a thermal wave feeds in from the edge of the spot does the plasma near the x axis see a non-zero radial pressure gradient and start to expand radially. For the Gaussian spot, radial temperature (and pressure) gradients are always present.

In Fig. 57.11(c) results are given for a simulation with a Gaussian beam of slightly bigger diameter (500 μm). Here the discrepancy at large y has almost vanished, especially for the solid experimental curves. Unfortunately the precise focal intensity distribution in the experiment was not known; thus it is entirely possible that the observed discrepancy is due primarily to an insufficiently precise knowledge of the focal spot.

Figure 57.11(d) presents the standard simulation but with a flux limiter[35] f of 0.65. (A value of 0.04 was used in the other simulations.) This led to the desired increase in the radial plasma size but also produced a more extended plasma in the x direction. One other possibility—a timing discrepancy of 0.2 ns between simulation and experiment—is investigated in Fig. 57.11(e). At the later time (1.26 ns) the predicted plasma is bigger, as expected, and has density contours comparable to those produced by the larger flux limiter. Thus, in order to make a strong statement about thermal transport, a good timing fiducial and an accurate knowledge of experimental parameters, such as the focal spot profile, are essential.

Conclusions

A new technique—grid image refractometry (GIR)—has been proposed for the determination of density profiles in underdense plasmas. The method has much in common with classical Schlieren techniques and other forms of refractometry, but includes some unique features that make it especially applicable to laser-produced plasmas where ray deflection angles can be large. GIR has significant advantages over interferometry for long-scale-length plasmas such as will be produced on the OMEGA Upgrade and, in particular, does not depend on probe-beam coherence and does not require inconveniently short probe times. (The probe duration for GIR should not exceed the time scale of plasma hydrodynamic motion, which is much greater than the fringe-blurring time.) The price paid is the loss of spatial resolution on the micron scale length, but, for the plasmas of interest, this is not particularly important. The feasibility of the method has been demonstrated by an experiment carried out on the CHROMA laser.

Even though experimental data were available just for a single shot, it has been possible to extract two-dimensional density profiles that extend up to $n_e = 10^{21}$ cm^{-3} and compare very well with hydrodynamic simulations. Few, if any, such detailed comparisons have been previously reported. For future applications to long-scale-length plasmas, it is proposed to replace the holographic system with a beam splitter and a recording system that will enable two (or more) images, corresponding to different object planes, to be recorded directly on a single shot. This should eliminate problems associated with temporal smearing of the holographic pattern.

GIR can in principle be used to investigate physical processes such as electron thermal transport, but only if an accurate knowledge of laser and target conditions is available. In addition, if a measurement were made of probe-beam attenuation across the same field of view (resulting from inverse bremsstrahlung), it would be possible to determine the electron-temperature profile in the plasma as well as the electron-density profile.

A knowledge of the density profile of long-scale-length plasmas is very important to the understanding of plasma physics issues relevant to inertial-confinement fusion. GIR seems to be a very attractive method with considerable promise for the diagnosis of millimeter-scale-length plasmas.

ACKNOWLEDGMENT

REFERENCES

1. R. S. Craxton, F. S. Turner, R. Hoefen, C. Darrow, E. F. Gabl, and Gar. E. Busch, Phys. Fluids B **5**, 4419 (1993).

2. F. B. Hildebrand, *Methods of Applied Mathematics*, 2nd ed. (Prentice-Hall, NJ, 1965), p. 276.

3. C. M. Vest, Appl. Opt. **14**, 1601 (1975).

4. M. Deutsch, Appl. Phys. Lett. **42**, 237 (1983).

5. D. T. Attwood, D. W. Sweeney, J. M. Auerbach, and P. H. Y. Lee, Phys. Rev. Lett. **40**, 184 (1978).

6. A. Raven and O. Willi, Phys. Rev. Lett. **43**, 278 (1979).

7. C. B. Darrow *et al.*, Phys. Fluids B **3**, 1473 (1991).

8. W. Seka, R. S. Craxton, R. E. Bahr, D. L. Brown, D. K. Bradley, P. A. Jaanimagi, B. Yaakobi, and R. Epstein, Phys. Fluids B **4**, 432 (1992); see also Laboratory for Laser Energetics LLE Review **47**, Quarterly Report No. DOE/DP/40200-166, 1991 (unpublished), p. 109.

9. B. J. MacGowan *et al.*, Bull. Amer. Phys. Soc. **38**, 1934 (1993), paper 3E 1.

10. H. Azechi *et al.*, Phys. Rev. Lett. **39**, 1144 (1977).

11. R. E. Turner and L. M. Goldman, Phys. Rev. Lett. **44**, 400 (1980).

12. G. J. Tallents, M. D. J. Burgess, and B. Luther-Davies, Opt. Commun. **44**, 384 (1983), and Erratum **45**, 420 (1983).

13. M. D. J. Burgess, G. B. Gillman, and B. Luther-Davies, J. Appl. Phys. **54**, 1787 (1983).

14. R. Fedosejevs, M. D. J. Burgess, G. D. Enright, and M. C. Richardson, Phys. Rev. Lett. **43**, 1664 (1979).

15. Gar. E. Busch *et al.*, Rev. Sci. Instrum. **56**, 879 (1985).

16. J. A. Tarvin *et al.*, Laser Part. Beams **4**, 461 (1986).

17. M. K. Prasad, K. G. Estabrook, J. A. Harte, R. S. Craxton, R. A. Bosch, Gar. E. Busch, and J. S. Kollin, Phys. Fluids B **4**, 1569 (1992).

18. R. R. Johnson *et al.*, Phys. Rev. A **41**, 1058 (1990).

19. R. P. Drake *et al.*, Phys. Fluids **31**, 1795 (1988).

20. R. S. Craxton and R. L. McCrory, J. Appl. Phys. **56**, 108 (1984).

21. L. A. Vasil'ev, *Schlieren Methods* (Israel Program for Scientific Translations, New York, 1971).

22. V. Gurfein *et al.*, Opt. Commun. **85**, 147 (1991).

23. N. Miyanaga, Y. Kato, and C. Yamanaka, Opt. Commun. **44**, 48 (1982).

24. R. Benattar and J. Godart, Opt. Commun. **49**, 43 (1984).

25. O. Kafri, Opt. Lett. **5**, 555 (1980).

26. J. E. Trebes *et al.*, Bull. Am. Phys. Soc. **38**, 2044 (1993).

27. I. Ghozeil, in *Optical Shop Testing*, 2nd ed., edited by D. Malacara (Wiley, New York, 1992), p. 367.

28. J. A. Sell *et al.*, Appl. Phys. Lett. **55**, 2435 (1989).

29. G. Gillman, Opt. Commun. **35**, 127 (1980).

30. D. T. Attwood, IEEE J. Quantum Electron. **14**, 909 (1978).

31. P. W. Schreiber, A. M. Hunter, and D. R. Smith, Plasma Phys. **15**, 635 (1973).

32. G. Charatis *et al.*, J. Phys. (Paris) **47**, C6-89 (1986).

33. B. I. Bennett *et al.*, Los Alamos National Laboratory Report LA-7130 (1978).

34. W. F. Huebner *et al.*, Los Alamos National Laboratory Report LA-6760-M (1977).

35. R. C. Malone, R. L. McCrory, and R. L. Morse, Phys. Rev. Lett. **34**, 721 (1975).

Transport and Sound Waves in Plasmas with Light and Heavy Ions

Ion-transport coefficients are important in various aspects of plasma physics. Some of the most commonly used transport formulas have been derived by Braginskii.[1] They are obtained by assuming a fully ionized, single-ion-species plasma. Typical laboratory plasmas, however, may involve more than one species of ions. For example, in magnetic-fusion devices, high-Z impurities can be present within the DT fuel. In inertial-confinement fusion plastic materials are commonly used as ablators, which then give rise to carbon and hydrogen ions. To calculate the transport of ions in such plasmas, within the framework of single-fluid theory, it is usual to employ an average-ion model in conjunction with the Braginskii formulas. The aim of this article is to show that such a simple procedure can considerably underestimate the levels of thermal diffusion, viscosity, and joule heating for a mixture of light and heavy ions. Implications for the damping of ion-acoustic waves will be shown.

We start by recalling the formulas for the ion thermal conductivity and viscosity coefficients in an unmagnetized single-ion-species plasma. They are, respectively (in cgs units),[1]

$$\kappa_i = \gamma_i \frac{n_i T_i \tau_i}{m_i} \tag{1}$$

and

$$\eta_i = \mu_i n_i T_i \tau_i , \tag{2}$$

where $\gamma_i = 3.91$, $\mu_i = 0.96$, n_i is the number density, m_i is the mass, and T_i is the temperature (in ergs). The ion-ion collision time for 90° angular scattering is given by

$$\tau_i = \frac{3\sqrt{m_i}\, T_i^{3/2}}{4\sqrt{\pi} e^4 n_i \left(Z_i^2\right)^2 \ln \Lambda_i} , \tag{3}$$

where e is the magnitude of the electron charge and $\ln\Lambda_i$ is the Coulomb logarithm.

Let us now consider a fully ionized plasma composed of approximately equal numbers of light and heavy ions (identified by l and h, respectively). It is clear from the above equations that if $Z_h \gg Z_l$, the transport will be dominated by the light species. However, since it is convenient to use a single-ion-species formalism, rather than treat the transport of each species separately, it is common to use Eqs. (1)–(3) with some appropriate average (denoted here by $\langle \ \rangle$) for m_i and Z_i. A popular approach is to use

$$\langle m_i \rangle = \left(n_l m_l + n_h m_h\right)/n_i ,$$

$$\langle Z_i \rangle = \left(n_l Z_l + n_h Z_h\right)/n_i ,$$

and

$$\langle Z_i^2 \rangle = \left(n_l Z_l^2 + n_h Z_h^2\right)/n_i ,$$

where

$$n_i = n_l + n_h .$$

To investigate the accuracy of this averaging procedure we need to recalculate the transport coefficients. The linearized Fokker-Planck equation, written in the frame of the light-ion species with mean velocity $\mathbf{u}_l$ (obtained by expanding the distribution function as $f = f_0 + \mathbf{w}\cdot\mathbf{f}_1/w$, where $\mathbf{w} = \mathbf{v} - \mathbf{u}_l$ is the intrinsic velocity), is given by[2]

$$\left(\mathbf{C}_1^{ll} + \mathbf{C}_1^{lh} \right) = w\nabla f_0^l + \left(\frac{Z_l e}{m_l}\mathbf{E} - \frac{d\mathbf{u}_l}{dt} \right) \frac{\partial f_0^l}{\partial w} , \tag{4}$$

where $d/dt = \partial/\partial t + \mathbf{u}_l \cdot \nabla$, f_0 is the isotropic Maxwellian distribution, $\mathbf{f}_1$ is the anisotropic part of the distribution (responsible for the transport), $\mathbf{E}$ is the electric field, and $\mathbf{C}_1^{ll}$ and $\mathbf{C}_1^{lh}$ are the anisotropic parts of the collision operators acting on $\mathbf{f}_1$. Equation (4) has been derived with the standard assumptions of strong collisionality (which imply that $|\mathbf{f}_1| \ll f_0$) and

negligible contribution from electron momentum exchange. Indeed, in the absence of *l-h* collisions, Eq. (4) predicts the classical single-ion-species thermal conductivity of Eq. (1). In our case, however, $C_1^{lh}/C_1^{ll} \sim n_h Z_h^2/n_l Z_l^2 \gg 1$ means that *l-h* collisions dominate over *l-l* collisions. Furthermore, the collision operator C_1^{lh} may be considerably simplified in the limit $m_h \gg m_l$ to become[2]

$$C_1^{lh} \approx -\frac{n_h Y_{lh}}{w^3}\left[\mathbf{f}_1^l + \left(\mathbf{u}_h - \mathbf{u}_l\right)\frac{\partial f_0^l}{\partial w}\right],$$

where

$$Y_{lh} = \frac{4\pi Z_l^2 Z_h^2 e^4 \ln \Lambda_{lh}}{m_l^2}$$

and $\mathbf{u}_h$ is the mean velocity of the *h* species (necessary to ensure momentum conservation).

Substituting this simplified collision operator back into Eq. (4) and expanding the right-hand side of that equation yields

$$\mathbf{f}_1^l = -\frac{w^4}{n_h Y_{lh}}\left[\left(\frac{m_l w^2}{2T_l} - \frac{5}{2}\right)\frac{\nabla T_l}{T_l}\right.$$

$$\left.+\frac{1}{p_l}\left(\nabla p_l - Z_l e n_l \mathbf{E} + n_l m_l \frac{d\mathbf{u}_l}{dt}\right)\right]f_0^l - \left(\mathbf{u}_h - \mathbf{u}_l\right)\frac{\partial f_0^l}{\partial w}. \quad (5)$$

We note that this equation is equivalent to the one used for modeling electron transport in high-*Z* plasmas.

Substituting Eq. (5) into the heat flow formula,

$$\mathbf{q}_l = \frac{2\pi}{3}m_l\int_0^\infty dw\, w^5 \mathbf{f}_1^l, \quad (6)$$

and using the velocity moment $\int dw\, w^3 \mathbf{f}_1^l$ to substitute for $\left(\nabla p_l - Z_l e n_l \mathbf{E} + n_l m_l d\mathbf{u}_l/dt\right)$, we obtain

$$\mathbf{q}_l = -\kappa_{lh}\nabla T_l + \beta_0 n_l T_l(\mathbf{u}_l - \mathbf{u}_h)$$

and the momentum exchange rate,

$$\mathbf{R}_{lh} = -\beta_0 n_l \nabla T_l - \alpha_0 \frac{n_l m_l}{\tau_{lh}}\left(\mathbf{u}_l - \mathbf{u}_h\right)$$

$$= m_l n_l \frac{d\mathbf{u}_l}{dt} + \nabla p_l + \nabla \cdot \pi_l - Z_l e n_l \mathbf{E}. \quad (7)$$

Here the thermal conductivity is

$$\kappa_{lh} = \gamma_0 \frac{n_l T_l \tau_{lh}}{m_l}, \quad (8)$$

where

$$\tau_{lh} = \frac{3\sqrt{m_l}T_l^{3/2}}{4\sqrt{2\pi}e^4 n_h Z_l^2 Z_h^2 \ln \Lambda_{lh}}, \quad (9)$$

$\alpha_0 = 3\pi/32$, $\beta_0 = 3/2$, and $\gamma_0 = 128/3\pi$. The stress tensor π_l, which has been added to Eq. (7), will be subsequently evaluated. By analogy with electron-transport theory we identify α_0, β_0, and γ_0 as the resistivity, thermoelectric, and electron thermal diffusion coefficients, respectively (in the high-*Z* limit). (Note the extra $1/\sqrt{2}$ factor in our definition of τ_{lh}.) These results are in close agreement with the work of Hirshman,[3] who derived the thermal transport and momentum transfer coefficients numerically (via a Sonine polynomial expansion) for plasmas of arbitrary composition.

By comparing Eq. (1) with Eq. (8) we note a significant increase in the conductivity coefficient γ. Differences with regards to the mass and *Z* dependencies are also apparent. The ratio between the conductivities is given by

$$\frac{\kappa_{lh}}{\langle \kappa_i \rangle} = \frac{\gamma_0}{\gamma_i}\sqrt{\frac{\langle m_i \rangle}{2m_l}}\frac{\langle Z_i^2 \rangle^2}{Z_l^2 Z_h^2}\frac{n_l}{n_h}\frac{\ln \Lambda_i}{\ln \Lambda_{lh}}. \quad (10)$$

If we consider a fully ionized CH plasma, where $m_l = m_p$ is the proton mass, $\langle m_i \rangle = 6.5 m_p$, $n_l = n_h$, $\langle Z_i^2 \rangle = 18.5$, $Z_l^2 = 1$, and $Z_h^2 = 36$, we obtain $\kappa_{lh}/\langle \kappa_i \rangle \approx 60$. The thermal conductivity contribution from the *h* species is expected to be negligible since

$$q_h/q_l \sim (n_h/n_l)(m_l/m_h)^{1/2}(Z_l^2/Z_h^2) \ll 1.$$

Comparisons with the conductivity of a pure-H plasma (κ_l) and a pure-C plasma (κ_h) show that $\kappa_h : \kappa_{lh} : \kappa_l = 1 : 306 : 4500$.

The same type of analysis can be used to calculate the viscosity coefficient. The linearized Fokker-Planck equation describing the stress tensor contribution to the distribution function, which is now expanded as

$$f = f_0 + \mathbf{w} \cdot \mathbf{f}_1 / w + \mathbf{w}\mathbf{w} : \mathbf{f}_2 / w^2 ,$$

is given by[2]

$$\mathbf{f}_2^l = \frac{w^4}{6 n_h Y_{lh}} \frac{\partial f_0^l}{\partial w} \mathbf{U}_l , \qquad (11)$$

where

$$\mathbf{U}_l = \nabla \mathbf{u}_l + \left(\nabla \mathbf{u}_l \right)^T - \frac{2}{3} \mathbf{I} \nabla \cdot \mathbf{u}_l$$

is the rate-of-strain tensor of the l species (superscript T denotes the transpose and $\mathbf{I}$ is the unit dyadic). From the definition of the anisotropic part of the pressure tensor,

$$\boldsymbol{\pi}_l = -\eta_{lh} \mathbf{U}_l = \frac{8 \pi m_l}{15} \int_0^\infty \mathbf{f}_2^l w^4 dw , \qquad (12)$$

we find that

$$\eta_{lh} = \mu_0 n_l T_l \tau_{lh} , \qquad (13)$$

where $\mu_0 = 256 / 45\pi \approx 1.81$. Note that this value of μ_0 extends the electron viscosity given by Braginskii [i.e., $\mu_0(Z=1) = 0.73$] to the high-Z limit.

As before, we can compare Eq. (13) with the averaged version of the standard formula [Eq. (2)] to obtain

$$\frac{\eta_{lh}}{\langle \eta_i \rangle} = \frac{\mu_0}{\mu_i} \sqrt{\frac{m_l}{2 \langle m_i \rangle}} \frac{\langle Z_i^2 \rangle^2}{Z_l^2 Z_h^2} \frac{n_l}{n_h} \frac{\ln \Lambda_i}{\ln \Lambda_{lh}} . \qquad (14)$$

Using the example of a CH plasma we then find that $\eta_{lh}/\langle \eta_i \rangle \approx 5$. The viscosity contribution from the h species is expected to be small since

$$\pi_h / \pi_l \sim \left(n_h / n_l \right) \left(m_h / m_l \right)^{1/2} \left(Z_l^2 / Z_h^2 \right) \ll 1 .$$

To illustrate the importance of these results we calculate the damping of collisional ion-acoustic waves in a CH plasma. Writing $\mathbf{u}_i = \left(\delta u_i, 0, 0 \right) \exp\left(ikx - i\omega_i t \right)$ etc., the linearized single-species ion fluid equations, assuming collisionless and isothermal electrons, become

$$-\omega_i \delta n_i + n_i k \delta u_i = 0 , \qquad (15)$$

and

$$\omega_i m_i n_i \delta u_i = kT_i \delta n_i + k \delta T_i n_i + k \delta \pi_{ixx} + k \delta \phi n_i Z_i e , \qquad (16)$$

and

$$-\frac{3}{2} \omega_i n_i \delta T_i + k n_i T_i \delta u_i = -k \delta q_i . \qquad (17)$$

The perturbed electric potential, assuming quasi-neutrality and neglecting Landau damping, is given by $\delta\phi = \delta n_i T_e / e n_i$.

Equations (15)–(17) yield a cubic dispersion relation, with roots ω_i corresponding to two counter-propagating and decaying ion-acoustic waves and a zero-frequency entropy wave (e.g., Ref. 4). By requiring strong collisionality, i.e., $\omega_i \tau_i \ll 1$, we are able to simplify the dispersion relation and obtain the following expressions for the ion-acoustic mode:

$$\frac{\left| \mathrm{Re}\left(\omega_i \right) \right|}{k} = v_i \sqrt{\frac{5}{3} + \frac{Z_i T_e}{T_i}} \equiv c_s , \qquad (18)$$

$$\frac{\mathrm{Im}\left(\omega_i \right)}{k v_i} = -\frac{2}{3} \left(\mu_i + \frac{\gamma_i}{5 + 3 Z_i T_e / T_i} \right) k \lambda_i , \qquad (19)$$

where $v_i = \left(T_i / m_i \right)^{1/2}$ is the ion thermal velocity, $\lambda_i = v_i \tau_i$ is its mean free path, and c_s is the sound speed.

To generalize these results to a plasma with light and heavy ions we would strictly need separate fluid equations for each species, and the resulting dispersion relation would be a sixth-order polynomial in ω. Instead, however, we can use the fact that $\left| \mathrm{Im}(\omega) \right| \ll \left| \mathrm{Re}(\omega) \right|$ to calculate the damping directly from the rate of entropy production. This approach,

described in detail by Braginskii,[1] is simpler than solving the dispersion relation and provides further physical insight into the damping processes.

The dissipative processes (thermal conduction, viscosity, and joule heating) are much weaker for the heavy particles than for the light, so we consider only the entropy of the light particles. We start with the entropy balance equation

$$\frac{\partial S_l}{\partial t} + \nabla \cdot \left(S_l \mathbf{u}_l + \frac{\mathbf{q}_l}{T_l} \right)$$

$$= \frac{1}{T_l} \left[-\frac{1}{2} \pi_l : \mathbf{U}_l - \mathbf{q}_l \cdot \nabla \ln T_l + Q_{lh} \right] , \qquad (20)$$

where $S_l = s_l n_l$ is the specific entropy, and (to lowest order in τ_{lh}) $Q_{lh} = -\mathbf{R}_{lh} \cdot \left(\mathbf{u}_l - \mathbf{u}_h \right)$ represents the heating of the light particles resulting from collisions with the heavy particles. To calculate the damping of a small-amplitude sound wave, we define the average over the wavelength L by example

$$\bar{S}_l = \frac{1}{L} \int_0^L S_l dz . \qquad (21)$$

Averaging Eq. (20) we then obtain an expression for the rate of entropy production in the wave:

$$\frac{d\bar{S}_l}{dt} = \frac{4}{3} \mu_0 n_l \tau_{lh} \overline{\left(\nabla \cdot \mathbf{u}_l \right)^2}$$

$$+ \gamma_0 \frac{n_l \tau_{lh}}{m_l T_l} \overline{\left| \nabla T_l \right|^2} + \alpha_0 \frac{m_l n_l}{T_l \tau_{lh}} \overline{\left| \mathbf{u}_l - \mathbf{u}_h \right|^2} . \qquad (22)$$

We represent the amplitude of the wave by

$$\delta n_l / n_l = \delta n_h / n_h = \xi \sin(kx - \omega t) ,$$

so that to lowest order in τ_{lh} we have

$$T_l = T_h \cong T_i ,$$

$$\delta T_i / T_i = 2 / 3 \xi \sin(kx - \omega t) ,$$

and

$$\delta u_l = \delta u_h = \xi c_s \cos(kx - \omega t) .$$

Using Eq. (7) to evaluate $\delta u_l - \delta u_h$ to first order in τ_{lh} then yields

$$\frac{d\bar{S}_l}{dt} = k^2 n_l \tau_{lh} \left[\frac{2}{3} \mu_0 c_s^2 + \frac{2}{9} \gamma_0 \frac{T_i}{m_l} + \frac{1}{2\alpha_0} \frac{T_i}{m_l} \right.$$

$$\left. \left(\frac{2\beta_0}{3} + \frac{5}{3} + \frac{Z_l T_e}{T_i} - \frac{m_l c_s^2}{T_i} \right)^2 \right] \xi^2 . \qquad (23)$$

The amplitude damping rate is given by

$$\mathrm{Im}(\omega) = -\frac{T_i}{2\bar{\varepsilon}} \frac{d\bar{S}_l}{dt} ; \qquad \bar{\varepsilon} = \frac{1}{2} n_i m_i c_s^2 \xi^2 .$$

This expression gives the rate at which the energy of the wave, ε, is degraded to heat. The resulting damping rate formula is

$$\frac{\mathrm{Im}(\omega_{lh})}{kv_l}$$

$$= -\frac{2}{3(5 + 3\langle Z_i \rangle T_e / T_i)} \left\{ \gamma_0 + \mu_0 \left(\frac{m_l}{\langle m_i \rangle} \right) \left(5 + 3\langle Z_i \rangle T_e / T_i \right) \right.$$

$$+ \left(\frac{3}{2} \right)^2 \frac{1}{\alpha_0} \left[\frac{2\beta_0}{3} + \left(\frac{5}{3} + \frac{Z_l T_e}{T_i} \right) \right.$$

$$\left. \left. - \left(\frac{5}{3} + \frac{\langle Z_i \rangle T_e}{T_i} \right) \left(\frac{m_l}{\langle m_i \rangle} \right) \right]^2 \right\} \left(\frac{n_l}{n_i} \right) k \lambda_{lh} , \qquad (24)$$

where $\lambda_{lh} = v_l \tau_{lh}$ and $v_l = \left(T_l / m_l \right)^{1/2}$. Here we can readily identify contributions due to thermal diffusion, viscosity, and joule heating by the coefficients γ_0, μ_0, and α_0, respectively.

An interesting feature of Eq. (24) is that it predicts the dominance of thermal diffusion over viscous effects for $\left(m_l / \langle m_i \rangle \right) \left(5 + 3\langle Z_i \rangle T_e / T_i \right) < 15 / 2$ (i.e., $T_e / T_i < 4.2$ for a

CH plasma, where $\langle Z_i \rangle = 3.5$ and $\langle m_i \rangle / m_l = 6.5$); whereas in the conventional formula the viscous damping is always dominant. More important, however, is the emergence of a joule-damping mechanism that is not present in the single-fluid model. It is easily shown for the case of CH plasma that this mechanism is dominant and at least three times larger than the thermal-diffusion mechanism. In terms of overall damping rate, a comparison between Eqs. (19) and (24), for CH, shows that

$$\frac{\mathrm{Im}\left(\omega_{lh}\right)}{\mathrm{Im}\left(\langle \omega_i \rangle\right)} \approx \frac{101 + 34\, T_e/T_i + 2.77\left(T_e/T_i\right)^2}{0.86 + T_e/T_i}. \qquad (25)$$

This predicts an increase in the damping rate by at least a factor of 58.

Another interesting feature of Eq. (24) is that the joule-damping mechanism becomes independent of T_e/T_i for plasmas in which both species of ions have the same charge-to-mass ratio, so $\langle Z_i \rangle / \langle m_i \rangle = Z_l / m_l$. In such a plasma the electric field, which is the only mechanism by which the electron pressure can affect the ions, cannot drive a velocity difference in the two species, and so cannot contribute to joule heating. In this case, the viscous damping can eventually dominate for sufficiently large T_e/T_i.

In summary, the ion-transport coefficients have been calculated for a fully ionized unmagnetized plasma composed of light and heavy ions. The results show that using standard single-ion formulas with averaged ion masses and ionizations can lead to significant underestimations of the thermal conductivity, viscosity, and joule dissipation. The implications for the collisional damping of ion-acoustic waves are that joule heating and thermal diffusion can become the dominant damping mechanisms and the overall damping rate increases.

ACKNOWLEDGMENT

REFERENCES

1. S. I. Braginskii, *Reviews of Plasma Physics* (Consultants Bureau, New York, 1965), Vol. 1, p. 205.

2. I. P. Shkarofsky, T. W. Johnston, and M. P. Bachynski, *The Particle Kinetics of Plasmas* (Addison-Wesley, Reading, MA, 1966).

3. S. P. Hirshman. Phys. Fluids **20**, 589 (1977).

4. M. D. Tracy, E. A. Williams, K. G. Estabrook, J. S. DeGroot, and S. M. Cameron, Phys. Fluids B **5**, 1430 (1993).

Three-Halves-Harmonic Radiation
from Long-Scale-Length Plasmas Revisited

Introduction

Starting with the very early experiments relating to laser fusion, observations have shown a characteristic spectral emission near the 3/2 harmonic of the irradiating laser wavelength.[1] For simplicity we will name this emission "3/2 self-emission" to distinguish it from similar spectral features that may be induced by a separate probe beam. This spectral signature was immediately recognized as being related to the underlying two-plasmon-decay[2–5] (TPD) instability near quarter critical density. The detailed generation mechanism for this emission is, however, still a subject of considerable controversy and active research. This article represents another attempt to explain the detailed origin of this emission and its consequences for diagnostic applications. These conclusions can be succinctly summarized as follows: (1) The observed threshold for this 3/2 emission is not a good indicator of the threshold of the underlying TPD instability; (2) the absence of 3/2 emission is not a reliable indicator of the absence of the TPD instability; and (3) the value of the spectral features as a temperature diagnostic is very limited at best.

These conclusions are contrary to the majority of published work.[6–9] On the other hand, LLE's position on this subject has been one of caution for quite some time,[10,11] clearly de-emphasizing the diagnostic value of this signature. More recently, Meyer and Zhu[12] reported on Thomson scattering experiments on CO_2-laser-plasma interactions that showed broadening of the k-vector spectrum of TPD plasma waves well above threshold. Their conclusions are essentially similar to ours, although they did not discuss the detailed 3/2-harmonic spectra and their relevance to shorter wave interaction physics.

The continued interest in the TPD instability lies primarily in its potential for generating energetic electrons,[13] which could prove detrimental for laser fusion. The energetic electrons are produced as a consequence of the large-amplitude plasma waves generated by the TPD instability. The threshold of the TPD instability is a few times 10^{13} W/cm^2 for typical laser-fusion applications.[11] In long-scale-length plasmas this instability is apparently not influenced significantly by current laser-beam-smoothing schemes, such as smoothing by spectral dispersion (SSD).[11] Contrary results were obtained in experiments with induced spatially incoherent[14] (ISI) beams. However, these experiments were single-beam, solid-target experiments with short density scale lengths and may therefore lead to different interaction results.

Experimental Setup and Data

The experiments were carried out on the 24-beam OMEGA UV (351-nm) laser system using eight beams to explode mass-limited targets (6-μm-thick, 600-μm-diameter CH targets). Another set of eight beams was delayed by 0.6 ns and maintained the electron temperature at ≥ 1 keV over periods of ~1 ns. An additional interaction beam was then incident on the plasma perpendicular to the original target surface and could be timed within a few nanoseconds of the heating beams. All beams were outfitted with distributed phase plates (DPP) for increased average irradiation uniformity (ignoring the high-frequency DPP speckle pattern). The plasma produced in this way has been carefully characterized[15] and modeled using the two-dimensional hydrodynamic code *SAGE*.

Streaked 3/2-harmonic spectra were taken primarily in the backscatter direction at ~30° with respect to the interaction beam. Details of these and other data have been reported in Ref. 11. Here we would like to discuss in more detail the 3/2 self-emission, which was only perfunctorily dealt with in Ref. 11.

In Fig. 57.12 we have reproduced two typical streaked spectra. The upper streak was taken with secondary heating beams, while the lower streak was taken without secondaries. The weak signal around 1 ns is due to the primary heating beams and is of no interest in this discussion. The typical, split 3/2 emission of interest is located between 1.4 and 2.1 ns in this figure. The temporal pulse shape of the secondary heating beams is shown superposed in the upper half. (The primary heating beams have the same pulse width and peak at 1 ns but are not shown in this figure.) The dotted line superposed on
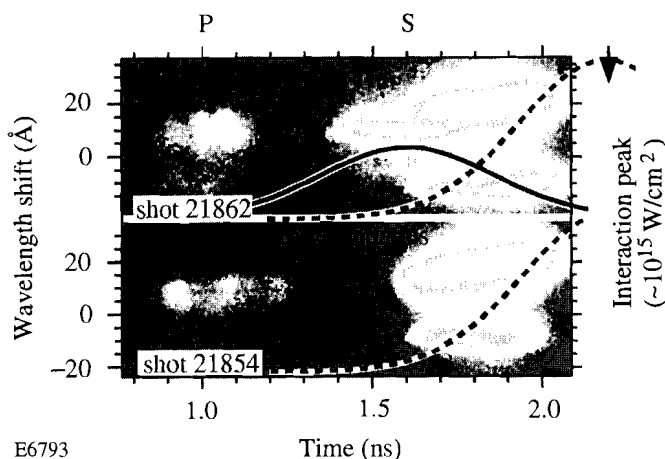
Figure 57.12

Streaked, 3/2-harmonic self-emission spectra from long-scale-length laser plasmas. Upper streak: spectrum in the presence of primary (P), secondary (S), and interaction (I) beams timed at $t = 1$ ns, 1.6 ns, and 2.2 ns, respectively. The intensities of the individual primary and secondary beams are ~5 to 6 × 10^{13} W/cm^2; that of the interaction beams is ~10^{15} W/cm^2. Lower streak: same as above but without secondary heating beams.

both streaks represents the normalized interaction beam intensity, which peaks at 2.2 ns. Note that the two curves are not drawn to scale; the on-target peak intensity of the interaction beam is ~10^{15} W/cm^2, while the peak intensity of each of the secondary (and primary) beams lies around $5-6 \times 10^{13}$ W/cm^2.

There is one obvious difference between the two streaks shown in Fig. 57.12. The upper trace contains an additional spectral component that starts at ~1.4 ns, well before the onset of the main 3/2 emission, and exhibits a smaller frequency shift relative to $3\omega_0/2$. This component has been discussed in detail in Ref. 11, where it was tentatively identified as due to Thomson scattering off TPD plasmons excited by one particular secondary heating beam. In this case the interaction beam plays only the role of a Thomson probe. Separate experiments have since verified this identification. This Thomson-scattering feature is thus a very sensitive diagnostic for the TPD threshold. The threshold was found to be ~2-3 × 10^{13} W/cm^2 for the following plasma conditions near $n_c/4 : T_e \approx 1$ keV, density scale length $L_n \approx 250$ μm, $\lambda_L = 351$ nm. The theoretical TPD threshold[4] is given by

$$I_{th}^{2\omega_p} \approx 5.2 \times 10^{15} T_{keV} / \left(L_{n,\mu m} \lambda_{\mu m} \right)$$

$$\approx 6 \times 10^{13} \ W/cm^2 .$$

This intensity is ~2-3 times higher than the experimental threshold but is consistent with the intensity distribution of a typical DPP speckle pattern in which ~60% of the energy is found at intensities above the peak of the smooth Airy enve-lope. The latter is the generally accepted nominal beam intensity, but significant energy content is found right up to ~3 times the nominal peak intensity.

By contrast, the main 3/2-harmonic, self-emission feature exhibits larger frequency splitting (~18-Å red shift and ~12-Å blue shift) and has a threshold of a few 10^{14} W/cm^2 (see Fig. 57.12). This threshold is 5-10 times higher than the TPD threshold determined above. Thus the 3/2 self-emission threshold is not a good measure of the TPD threshold nor is the absence of 3/2 self-emission proof that the TPD instability is not excited. Here we make the usual assumption that all 3/2 emission is due to some form of Thomson scattering involving incident photons of the interaction beam and plasmons of frequency close to $\omega_0/2$, which are in some way related to the TPD instability. The problem with this assumption is the difficulty of satisfying the required phase-matching conditions.

Interpretation of Data

Reference 11 pointed out that the frequency splitting of the self-emission spectra is consistent with Thomson scattering of the interaction beam off TPD plasmons near the Landau cutoff. However, the phase-matching conditions for this scattering process are not easily satisfied, as will be discussed below. In addition, the theoretically predicted, maximum TPD growth occurs closer to $n_c/4$ with correspondingly smaller frequency splitting between the plasma waves, yet we find no evidence of these plasmons in the 3/2-harmonic self-emission spectra. However, it should be kept in mind that the growth rates drop off only very slowly with decreasing electron density.[4]

In Fig. 57.13 the TPD decay diagram is shown in k-vector space with $k_\parallel$ aligned with the density gradient prevailing in the interaction region. All TPD decay triangles terminating on a given horizontal line result in plasma waves with the same frequencies, $\omega_0/2 \pm \Delta\omega$. The TPD growth rate has its maximum along the hyperbola shown in the graph and drops to zero near the Landau cutoff, and also for $k_\perp = 0$. The growth rate[4] decreases quite slowly as one moves away from the hyperbola of maximum growth, as is also shown in Fig. 57.13 ($\gamma \approx 0.6 \, \gamma_{max}$ at edge of shaded area).
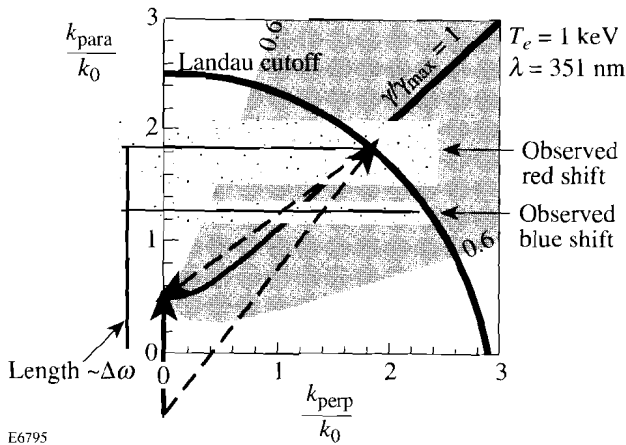
Figure 57.13
Two-plasmon decay diagram in k-space with $k_\parallel$ aligned parallel to incident beam and local density gradient. The Landau cutoff is given by $k\lambda_D = 0.3$. The frequency shifts of the two TPD daughter waves are proportional to the ordinate of the apex of the decay triangle as shown. The shaded areas correspond to the observed shifts for the red and blue components of the 3/2-harmonic self-emission.

The upper, stippled, horizontal area indicates the range of 3/2-harmonic red shifts seen in the experiments. The observed blue shifts are smaller and correspond to the lower stippled area as though the two 3/2-harmonic features originated from different decays. This difficulty can be removed as follows: First we assume that the primary TPD decays occur near the Landau cutoff and close to the maximum growth rate hyperbola. Second, to approach the phase-matching conditions for Thomson scattering involving an incident photon (wave vector k_0) and a "blue" plasmon, we must invoke a secondary electron plasma wave (EPW) decay of the "blue," i.e., longer k-vector plasmon. This results in a reduced blue-shifted secondary plasmon whose direction is parallel to that required for phase matching for Thomson scattering (see lower half of Fig. 57.14). The blue shift of this plasmon from

$\omega_0/2$ also corresponds closely to that observed for the blue 3/2-harmonic feature as was already pointed out in Ref. 11. This kind of secondary decay process has been variously invoked experimentally[16,17] and theoretically[18] but was usually combined with propagation of plasmons in the density gradient. However, the importance of a threshold of these secondary decays has not been recognized.

E6796
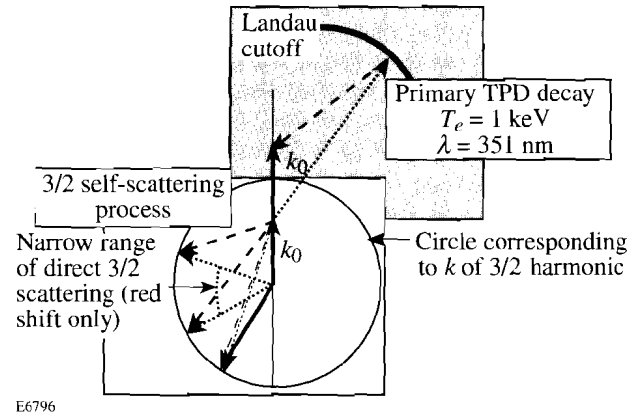
Figure 57.14
k-vector diagrams of the primary TPD decay and the secondary Thomson scattering process leading to 3/2-harmonic self-emission. The upper part of the figure shows the primary TPD decay, while the circle in the lower part represents the locus of the 3/2-harmonic em wave generated by summing an incident photon (k_0) with a plasmon. With the exception of a small range of "red" plasmons giving rise to near-90°-sidescattering, 3/2-harmonic radiation, all plasmons participating in the Thomson-scattering process must first undergo a secondary electron plasma wave decay for the "blue" plasmons or must be scattered by appropriate ion waves ("red" plasmons).

Invoking the secondary EPW decay has a number of interesting consequences: (1) It explains the higher threshold for the 3/2 self-emission compared to the TPD threshold since the plasma waves have to build up to where their intensity exceeds the threshold of the EPW decay instability. (2) The EPW decay growth rate is proportional to k and thus maximizes near the Landau cutoff. This could explain why the dominant 3/2 emission reflects TPD decays just below the Landau cutoff density. Furthermore, the decay process, while peaking in back direction, is not restricted to exact backscattering. It can thus generate the plasma waves with the proper direction for phase matching to Thomson scattering as discussed above (see Fig. 57.14). (3) Once the EPW decay instability is above threshold, ubiquitous ion waves are produced, which has been variously reported in PIC code simulations[19,20] and in experiments on 3/2-harmonic generation.[21,22]

Direct experimental evidence for the TPD instability near the Landau cutoff is shown in Fig. 57.15. The scattering configuration for this streaked spectrum is indicated at the top of the figure. One of the secondary beams was selected as the "interaction beam" while the nominal interaction beam was delayed to peak 1 ns later as indicated in the figure. The very strong Thomson signal exhibits exactly the predicted shift and is only visible in the presence of the secondary beam acting as interaction beam. (Note that the polarization was chosen to optimize this signal and that experimental constraints forced us to probe TPD decays below the maximum growth rate hyperbola. The exact decay triangle probed was located in the lower stippled area (see Fig. 57.13) and very near the Landau cutoff.

The spectral splitting of the 3/2-harmonic self-emission is of very dubious diagnostic value for estimating the coronal temperature. The above model for generating this 3/2 self-emission involves two competing effects: the spectral splitting increases with temperature for any given plasmon k-vector length $\left(\Delta\omega \sim k^2 T_e\right)$, but this effect is counterbalanced by the k-vector cutoff set by Landau damping:

$$\left(k_{\text{cutoff}} \sim 1/\lambda_D \sim T_e^{-1/2}\right).$$

Thus, one would not expect any significant temperature dependence of the 3/2 spectral splitting, which corresponds well to most of our observations. The lower streaked spectrum in Fig. 57.12 is a notable exception: here, the intense interaction beam is incident on a very cold plasma (no secondary heating beams), and very strong heating (and filamentation) is expected.

Conclusions

In this article we propose a new interpretation of the ubiquitous 3/2-harmonic emission from laser-produced plasmas. This emission is a consequence of the strongly driven TPD instability whose plasma waves (daughter waves) undergo secondary electron plasma wave decays above a certain threshold. The plasma waves produced in this process can then be Thomson scattered using again photons of the interaction beam. The resulting spectral shifts are in accord with experimental observations. On the other hand, the 3/2 self-emission threshold reflects the threshold of the EPW decay instability rather than that of the primary TPD instability. While the existence of the 3/2-harmonic emission is always associated with the TPD instability, its absence is not conclusive proof for the absence of the TPD instability. Within the framework of this model the 3/2 self-emission spectra are not a useful temperature diagnostic.
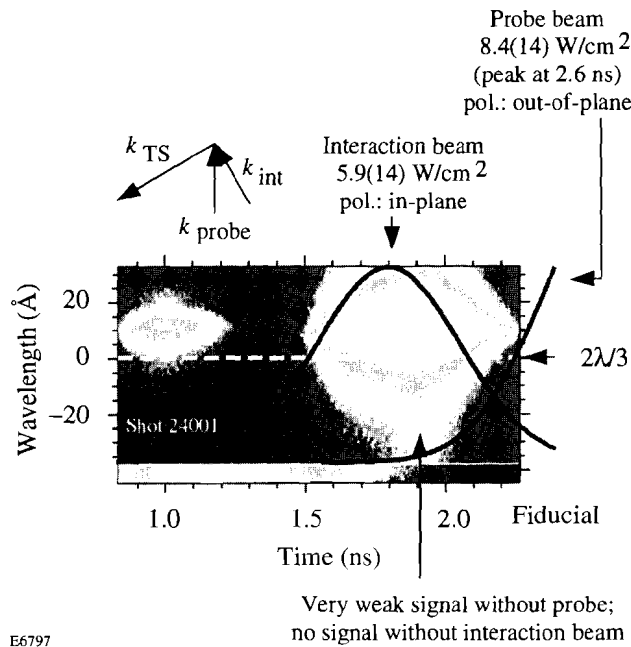
Figure 57.15

Direct evidence of TPD decay near the Landau cutoff using Thomson scattering. The TPD decay was driven by a particular secondary beam focused to ~6 × 10^{14} W/cm² (averaged over the DPP speckle pattern). The Thomson probe beam was delayed to peak at 2.6 ns to avoid any accidental 3/2-harmonic generation from the probe beam itself.

ACKNOWLEDGMENT

REFERENCES

1. J. L. Bobin *et al.*, Phys. Rev. Lett. **30**, 594 (1973); P. Lee *et al.*, Appl. Phys. Lett. **24**, 406 (1974); H. C. Pant *et al.*, Opt. Commun. **16**, 396 (1976).

2. C. S. Liu and M. N. Rosenbluth, Phys. Fluids **19**, 967 (1976).

3. A. Simon, R. W. Short, E. A. Williams, and T. Dewandre, Phys. Fluids **26**, 3107 (1983).

4. W. L. Kruer, The *Physics of Laser Plasma Interactions* (Addison-Wesley Publ. Co., Redwood City, CA. 1988), pp. 81 ff.

5. H. A. Baldis, E. M. Campbell, and W. L. Kruer, *Handbook of Plasma Physics*, edited by N. M. Rosenbluth and R. Z. Sagdeev (Elsevier Science, Amsterdam. 1991), Vol. 3, pp. 397–408.

6. A. I. Avrov *et al.*, Sov. Phys. JETP **45**, 507 (1977); V. Yu. Bychenkov *et al.*, Beitr. Plasma Phys. **23**, 331 (1983); R. L. Berger and L. V. Powers, Phys. Fluids **28**, 2895 (1985).

7. J. Meyer, Y. Zhu, and F. L. Curzon, Phys. Fluids B **1**, 650 (1989).

8. P. E. Young *et al.*, Phys. Rev. Lett. **61**, 2766 (1988).

9. P. E. Young *et al.*, Phys. Fluids B **2**, 1228 (1990).

10. W. Seka, B. B. Afeyan, R. Boni, L. M. Goldman, R. W. Short, K. Tanaka, and T. W. Johnston, Phys. Fluids **28**, 2570 (1985).

11. W. Seka, R. E. Bahr, R. W. Short, A. Simon, R. S. Craxton, D. S. Montgomery, and A. E. Rubenchik, Phys. Fluids B **4**, 2232 (1992).

12. J. Meyer and Y. Zhu, Phys. Rev. Lett. **71**, 2915 (1993).

13. N. A. Ebrahim *et al.*, Phys. Rev. Lett. **45**, 1179 (1980); D. W. Phillion *et al.*, Phys. Rev. Lett. **49**, 1405 (1982); D. M. Villeneuve, R. L. Keck, B. B. Afeyan, W. Seka, and E. A. Williams, Phys. Fluids **27**, 721 (1984); R. L. Keck, L. M. Goldman, M. C. Richardson, W. Seka, and K. Tanaka, Phys. Fluids **27**, 2762 (1984).

14. T. A. Peyser *et al.*, Phys. Fluids B **3**, 1479 (1991).

15. W. Seka, R. S. Craxton, R. E. Bahr, D. L. Brown, D. K. Bradley, P. A. Jaanimagi, B. Yaakobi, and R. Epstein, Phys. Fluids B **4**, 432 (1992).

16. F. Amiranoff, F. Brian, and C. Labaune, Phys. Fluids **30**, 2221 (1987).

17. A similar secondary decay process was proposed for the strongly driven parametric decay instability by K. Tanaka, W. Seka, L. M. Goldman, M. C. Richardson, R. W. Short, J. M. Soures, and E. A. Williams, Phys. Fluids **27**, 2187 (1984).

18. H. C. Barr and G. A. Gardner, in the *1984 International Conference on Plasma Physics*, edited by M. Q. Tran and M. L. Sawley (Ecole Polytechnique, Lausanne, 1984), Vol II, p. 265; S. J. Karttunen, Laser and Particle Beams **3**, 157 (1985).

19. A. B. Langdon, B. F. Lasinski, and W. L. Kruer, Phys. Rev. Lett. **43**, 133 (1979).

20. D. F. DuBois and H. A. Rose, Bull. Phys. Soc. Am. **38**, 1913 (1993), paper 2Q 6.

21. P. E. Young *et al.*, Phys. Rev. Lett. **61**, 2766 (1988).

22. D. M. Villeneuve, H. A. Baldis, and C. J. Walsh, Phys. Fluids **28**, 1454 (1985); H. A. Baldis and C. J. Walsh, Phys. Scr. **T2/2** (1982); H. A. Baldis and C. J. Walsh, Phys. Rev. Lett. **47**, 1658 (1981).

OMEGA Upgrade Status Report

The completion (and acceptance by the Department of Energy) of the final design of the upgrade to the OMEGA laser system marks the beginning of the system-integration phase of the project. System integration is the manufacturing and installation of the various subassemblies that constitute the laser system. It began during this reporting period with the delivery and installation of the major structures. By the end of December, nearly all of the support structures were installed in the laser and target bays.

In November, all of the main target bay structures were installed, including the F-ASP monoliths, both end mirror structures, and the target mirror structure (TMS). During that time, the target chamber had to be installed within the TMS. To be completed are the personnel platform for the TMS and the periscope mirror assembly.

In the laser bay, nearly all of the structures were installed, including all the splitters, the amplifier and spatial filter structures for stages A through E, and the structures for the frequency converters. Left to install are four structures: one for the stage-F amplifiers and three for the stage-F spatial filters.

This issue of the LLE review continues the series begun in the last issue—the system description as excerpted from the Executive Summary provided to DOE as part of the review documentation of the OMEGA Upgrade design. This issue contains descriptions of subsystems including power conditioning, controls, optomechanical systems (both laser and target areas), and major structures.

Power Conditioning

The power-conditioning subsystem converts utility ac electrical power into the high-voltage, high-current electrical pulses used to fire the flash lamps that supply optical pump energy to the laser amplifiers. To create these pulses, large capacitors are charged to high voltage (7 kV) and then dis-charged through a pulse-forming network (PFN) comprising that capacitor, an inductor, and a flash-lamp pair.

The number of flash lamps used in each amplifier is dependent upon the size of the amplifier. Each PFN is connected to one, two, or five flash lamps, depending on whether it feeds a 15-cm, 20-cm, or rod amplifier, respectively. An assembly consisting of the PFN's, a charger, and the control circuitry needed to power one laser amplifier is referred to as a power-conditioning unit (PCU). This is a complete unit requiring only command instructions from the power-conditioning control computer and ac input power. A charging power supply in each PCU allows adjustment of the energy output of each amplifier; this level of control is required for balancing the power of the laser system.

In addition to the main discharge circuitry, many PCU's will have preionization and lamp check (PILC) circuits. This circuitry provides a lower energy pulse (higher voltage, lower current) that is fired 250 μs before each normal system shot (preionization). This pulse ionizes the gas in the lamp in preparation for the large current pulse that will follow. The preionization provides a near full-bore discharge that reduces the production UV line radiation that is detrimental to amplifier lifetime. In addition, the acoustic shock from the electrical discharge is reduced when a PILC is used. The PILC discharge is also used alone after a shot to check for lamp failures on that shot (lamp check). The PCU has the circuitry required to monitor each lamp during this PILC discharge and detect any that do not conduct current; faulty lamps will be replaced prior to the next shot.

To ensure safe operation, each PCU has an extensive array of hard-wired logical interlocks and self-checks. This is complemented by a local microprocessor used to monitor the interlocks and the status of various voltages and currents. This PCU control module (PCM) is based on the Neuron® Chip

from Echelon Corporation. The module contains LON (local operating network) interface circuits, a trigger input receiver, a logic power supply, and fiber-optic transceivers for communication. The PCM is housed in a steel enclosure with an eight-character alphanumeric display to indicate the status of the PCU.

Because of the high voltages present in the power-conditioning subsystem, safety was a major concern during design. The PCU's are computer controlled for normal operation, but for safety there are a number of "hard-wired" interlocks that do not rely on computers for activation. For instance, each of the enclosures is interlocked, and the capacitor is immediately discharged when the interlock is violated.

At the normal operating voltages the power-conditioning system will be capable of storing 42 MJ of electrical energy. The system is rated for even higher voltages, storing 46.2 MJ at full rated voltages. The extra capability will accommodate future needs as amplifiers (and other components) degrade and require more pump energy to obtain the nominal stage gains.

The Upgrade power-conditioning system consists of 120 disk amplifier PCU's and 97 rod amplifier PCU's. There are two types of disk amplifiers and, hence, two styles of disk PCU's. The difference is the number of individual flash-lamp circuits (PFN's) required. The 20-cm SSA (single-segment amplifier) PCU requires 16 PFN's, while the 15-cm SSA PCU requires only 12 PFN's. Other than the number of PFN's the units are identical. The PCU's will store a maximum of 368 kJ (20 cm) or 276 kJ (15 cm) at 14.8 kV.

There will be two styles of PCU's for the rod amplifiers. One type will power the stage-D and the laser driver ampli-

fiers and will use existing OMEGA power-conditioning units with modern controls and new components. A new charging power supply will replace the 12-head chargers formerly used in the OMEGA units. These PCU's will not have PILC circuits and will store a maximum of 78 kJ at 7.5 kV. The second type of rod PCU will be used for the A, B, and C stages of rod amplifiers. These are basically a cross between the disk amplifier PCU and the stage-D rod amplifier PCU. These totally new units will also store 78 kJ at 7.5 kV (maximum voltage) and will have PILC circuits similar to the disk amplifiers.

All PCU's will require a timing signal to synchronize firing of the amplifiers. This signal will originate in the master timing system (located in the pulse-generation room) and be distributed throughout the capacitor bays to each PCU. The initiation of this signal is commanded by the power-conditioning control computer. This signal will be delayed individually at each PCU by an amount set by the power-conditioning control computer. This delay is adjusted to synchronize the peak of the amplifier gain to the arrival of the laser pulse at that amplifier. The performance of the power-conditioning system is outlined in Table 57.I.

Upgrade Control System

The Upgrade Control System (UCS) will provide operators with remote control of subsystems, displays of sensor data, and safe, automatic sequencing of key processes. The control system will also collect and record information about each shot.

1. Control System Functions

The following eight functions have been assigned to the UCS as the design of the OMEGA Upgrade system has progressed:

Table 57.I: PFN Specifications

	Disk Amps	Rod Amps
Pulse width (μs)	550	475
Linear resistance (mΩ)	120	100
Inductance (μH)	180	55
Capacitance (μF)	210	460
Charging voltage (kV)	14.1	7.3
Stored energy/PFN (kJ)	20.9	12.3
Total energy (MJ)	35.1	7.1
TOTAL ENERGY (MJ)	42.2	

1. Control of the electric power and the fluid facilities that support the beamline amplifiers
2. Routine operational alignment of the beamline optics
3. Control of the laser drivers subsystem
4. Diagnosis of the laser system's performance
5. Control of personnel access to the laser bay, target bay, capacitor bays, and the rooms under the target bay
6. Control of the vacuum system that services the spatial filters
7. Control and, where appropriate, data-acquisition support of the instruments that sense shot-event parameters
8. Control of the vacuum systems that service the target chamber and the target diagnostic instruments

These have been allocated to six top-to-bottom "functions" within the UCS:

1. The power-conditioning function will provide the power conditioning and fluid control for all of the single-pass amplifiers in the system, including those in the laser drivers subsystem.
2. The alignment function will implement beamline alignment processes, beamline energy control, and beam-to-beam timing control.
3. The laser drivers function will provide control and monitoring of the initial pulse generation and amplification processes. This includes the multipass lasers at the start of the system and the appropriate alignment and beam diagnostic elements.
4. The beamline diagnostics function will control the op-

eration and data-acquisition functions of the instruments that measure the characteristics of the laser pulse produced by the beamlines.
5. The facility interlock function will control personnel access and the main electric power source as a function of system status.
6. The experimental system function will control the target chamber subsystems and the data-acquisition systems for the target diagnostic instruments.

An additional **seventh function**, the shot executive, is also required. This function will serve to coordinate the activities of the other functions when it is necessary for them to work together to conduct a target shot.

2. Operations Timing

The activities that make up these functions take place during the operational periods that preceed and follow the brief high-energy shot event. (Figure 57.16 illustrates this relationship.) The control system activities support maintaining the system, preparing it for the shot, and recording the shot results. The timing resolution necessary to implement these requirements is of the order of tens of seconds.

The shot executive function initiates the "pre-shot" processes that must take place in the hour before a shot, verifies that the other functions are ready for the actual shot, and initiates the "shot" preparations. Thereafter, the power-conditioning function controls the laser system to within ten seconds of the shot and then enables the key system elements to

Figure 57.16
The flow (in time) of the system control operation for routine shots and maintenance. When the capacitor power supply is enabled, the system is termed active. The shot cycle is a heightened readiness state involving all of the control functions.

proceed on the basis of the electrical master timing signal. The events synchronized by the master signal include generation of the optical pulses in the laser drivers subsystem, the electrical pulses that drive the flash lamps in the laser amplifiers, and the operation of diagnostic instruments. The timing and duration requirements for the flash-lamp current are in the 100-μs range and are implemented by the electronic circuits in the PFN's. The submicrosecond characteristics of the optical pulses are achieved by electro-optical techniques.

3. General Architecture

The general hardware/software architecture that will implement each of these functions is illustrated in Fig. 57.17. Separate "executive" processes for each function will run on

workstations installed in the control room. These are referred to as "host processors" and will be connected to each other and to other OMEGA Upgrade system computers via a dedicated Ethernet local area network.

Each function's executive process will provide the operator interface for the function and will exert control over and receive information from devices in the bays by communicating with one or more "intermediate" processors over the Ethernet. These intermediate computers serve to relieve the executive of routine computation and downward communication tasks. Communication between the executive processes is necessary primarily for coordination of shot-related events.
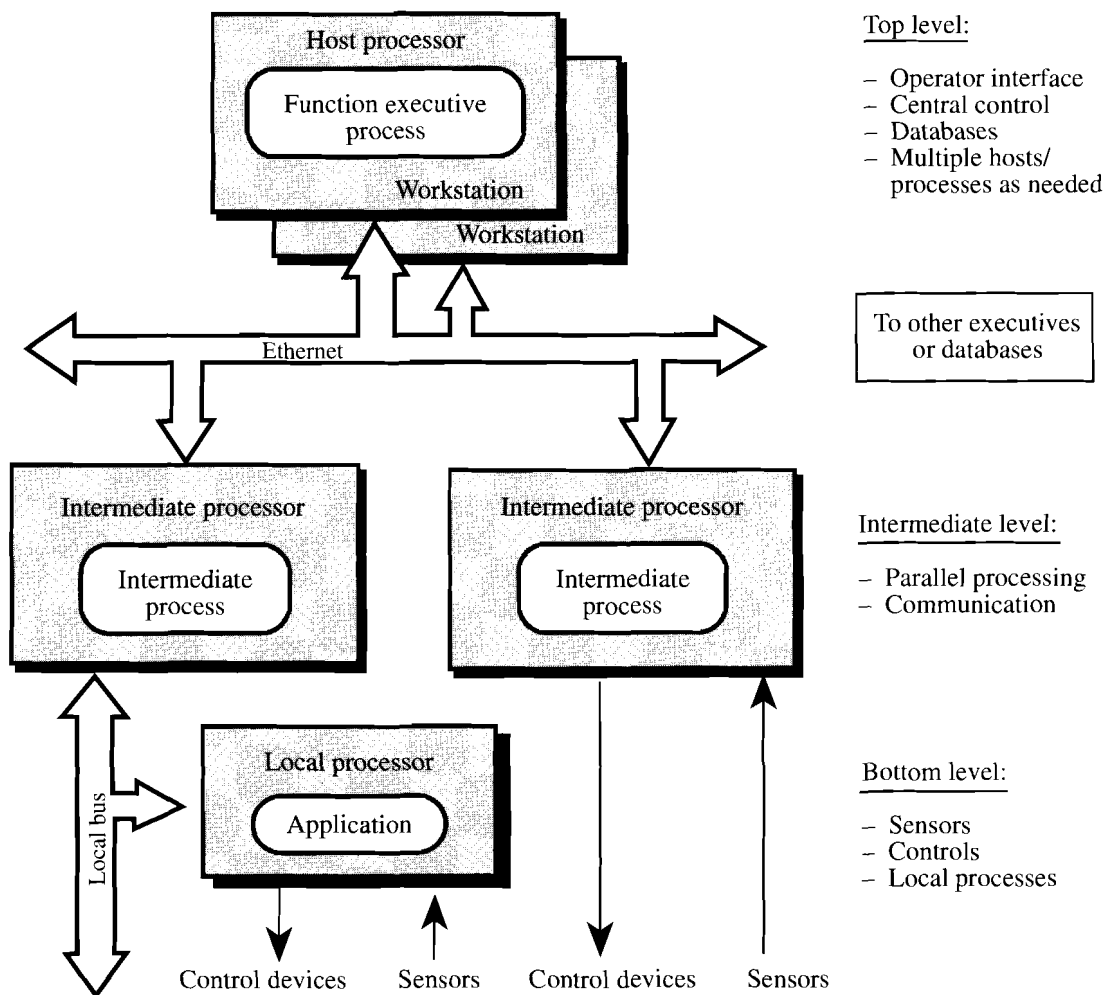
Figure 57.17
The top-level architecture of the OMEGA Upgrade control system. Three levels of computers are used to provide a system with distributed intelligence. Personnel interact with a host processor, which commands, via two local networks, numerous microprocessor-controlled devices.

At least two variations of the intermediate and bottom architectural levels will be employed in the UCS. In many situations, a third layer of computer control based on a Neuron® Device Control will be used. The Neuron is an inexpensive, single-chip, multiprocessor system that implements a local area network protocol called a local operating network (LON) and provides for control of devices and acquisition and communication of data. In the UCS, nearly 2000 Neurons will be used to integrate simple control actuators and feedback sensors under software control to produce more-sophisticated, local control devices. Neurons will also be used to acquire and digitize data from diagnostic sensors. Where the Neurons are used, the primary function of the intermediate process is to act as interpreter between the Ethernet and the LON. In this case the intermediate processor is called a LON Ethernet Network Adapter (LENA). Each LENA will service four LON's (channels), each of which will support 50 to 150 Neurons. (This configuration is illustrated on the left side of Fig. 57.17.)

Another architectural variation (illustrated on the right side of Fig. 57.17) is used to control the alignment video cameras and to acquire and process video frame data. This configuration is referred to as a digital expandable still camera (DESC). Here the intermediate process controls up to five cameras directly, rather than via a network. The DESC process also performs the digital image processing necessary to convert frames of video data into two-axis error data that is transmitted to the alignment function executive process. Similar configurations will be used to control diagnostic devices in the laser drivers, laser diagnostics, and experimental system functions.

4. Facility Interlocks

Personnel safety is of primary importance in the design of the OMEGA Upgrade System. Three major classes of hazards are addressed at a fundamental level by interlock functions built into the utilities that are part of the laboratory facility supporting the laser system. These are

- control of the power source for the high voltages inherent in the laser amplifiers;

- control of the warnings issued when the presence of alignment laser emissions could constitute an eye hazard; and

- active and passive monitoring of the location of personnel in the bays.

These and other basic facility-monitoring features are included in the following specific facility interlock subsystems:

- The electric power source for all the laser amplifiers is a commercial power substation formally designated Unit Substation #2 and commonly referred to as "the 750-kVA power source." This equipment is located at the west end of Capacitor Bay 1 on the lower level of the slab. No electric power will be available to the power-conditioning units unless a relay in the substation is closed by logic built into facility interlock hardware.

- Five laser sources and 79 beam-train shutters will be monitored to control lighted warning signs at seven locations. A voice enunciator will provide audible warnings of status changes.

- Approximately 30 surveillance video cameras will provide operators with views of the bays.

- Approximately 44 passive infrared motion sensors will alert operators to movements at times when there should be no activity.

- The open/closed status of 28 doors will be remotely sensed and monitored; 16 of these doors will also be equipped with remotely controlled locks.

- During normal operations, the identity of the occupants in each of five controlled zones will be monitored by means of a combination of badge readers and door-lock controls at the entrances.

- Bells and light beacons will warn of impending capacitor charging.

- Manual "dump buttons" are provided at numerous locations in the bays. These will directly disable the 750-kVA power and short-circuit all of the high-voltage capacitors in the system.

- The interlock logic will control grounding isolation features that ensure both personnel safety for routine operations and hardware safety during the shot events.

- The interlock logic will be able to override other controls and turn off the bay lighting.

5. Beamline Diagnostics

Acquisition of beamline diagnostic data is a major branch of the overall Upgrade control system architecture. One of the five control system executive workstations (beamline diagnostic executive) is dedicated to operating the laser diagnostics configured on the 60 beamlines located in the laser bay. These diagnostics include the following measurement systems:

- Harmonic energy detection (IR, green, and UV energy measurements)

- Full-aperture, high-flux calorimeters

- Beamline-to-beamline IR energy balance (splitting ratios, wave-plate settings)

- UV-on-target energy transport (3ω to target, beam-balance compensation)

At the highest level of the control architecture, the executive workstation first issues commands to the acquisition subsystems and then collects and processes the data for the laser system operators to evaluate. Below the executive workstation in this hierarchy are the local data-acquisition nodes that contain the specialized hardware used to interface to the laser diagnostics. These nodes reside on a combination of Versa Module Europa (VME) and Computer Automated Measurement and Control (CAMAC) platforms, depending on the application. In either case, these nodes communicate with the executive workstations through an Ethernet link. The local data-acquisition VME platform nodes contain embedded SPARC computers. These computers handle the lower-level input/output control and acquisition sequencing required to collect diagnostic data. The CAMAC platforms are interfaced to the VME platforms through high-speed, ~1.5-Mb/s bus adapters and have no local intelligence. This interface allows data to flow from CAMAC into the VME system at, or near, CAMAC backplane speeds. At the lowest level of the acquisition architecture are transient digitizing oscilloscopes and CCD (charge coupled device) camera arrays, discrete photodiodes, etc. These are used to capture electrical waveforms, two-dimensional optical data, pulsed events, etc. The oscilloscopes are interfaced to the intelligent VME nodes through dedicated general purpose interface bus (GPIB) communication lines. The CCD cameras have local video controllers and digitizing frame grabbers to buffer the images before uploading the data to the executive workstations.

Diagnosis and adjustment of the beam arrival time at the target is another critical control-system function. The responsibility for the associated tasks is shared by two of the top-level control-system functions. The beam arrival times will be measured using a photodiode at the target location and an rf interferometric technique. This system will determine the time differential between the arrival of a laser pulse at that location and the arrival of the same pulse at a reference location. The laser pulses will originate at the IR alignment table (IRAT) and be propagated through the beamlines from the stage-A splitter to the target chamber. The arrival time for each of the 60 beams is acquired sequentially. The resolution of the measurement is expected to be better than 1.5 ps.

This process must be performed as a special activity separate from normal shot operations. The alignment function will configure the IRAT and the beamlines to provide the pulses to the photodiode sensors. The experimental system function will position and control the sensor at the target location and acquire/reduce the time-differential data. The alignment function will process the timing data to determine the path adjustments required and then control the path length adjustment systems (PLAS's) to implement any required changes.

Optomechanical Systems
1. Optical System Design

The optical design of the system was constrained primarily by two factors: the need to fit the upgraded laser into the existing building and the desire to reuse as much hardware as possible (spatial filters, in particular). The top-level requirements for the total energy and the number of beams dictated the amplifier staging and the beam splitting required. Optical damage thresholds dictated the minimum beam diameters in each stage, which in turn fixed the magnification between stages. From these baselines the system was designed to incorporate image relaying as required by the implementation of SSD (smoothing by spectral dispersion) and by sound laser design practices.

Given the above, the layout of the laser system was then refined to ensure that no damage occurs from "ghost" reflections, provide equal path lengths in all beamlines, and provide an accessible and manageable system. The configuration has undergone several changes since the preliminary design. These changes were dictated by performance issues and ultimately resulted in a simpler configuration.

Once the system configuration was determined, error budgets were performed for energy, wavefront, alignment, and polarization. Each of these budgets was then distributed to the individual components in the system to formulate the requirements. For example, the wavefront budget was used to specify that the wavefront error contributed by each optical component not exceed $\lambda/10$. This value is relatively small because the disk amplifiers consume a major portion of the error budget. The pointing error in the system is driven by the requirement to point beams onto target with a precision of ~5% of the target radius. Given a minimum target radius of 300 μm and a 1.8-m-focal-length final lens, the total pointing error budget is 8.33 μrad. The distribution of this error affected the design of the alignment sensor packages, the optical mounts, and the various structures supporting the laser. It was this pointing error budget that necessitated the implementation of the epoxy/granite structures for the stage-F alignment sensor packages (ASP's), which act as the optical alignment references for the system.

The energy budget specified the fluences at various points in the system, thereby impacting the choice of substrate material, typically BK-7 or fused silica. The energy-balance constraints drove a requirement for identical beam sizes at all the frequency-conversion cells, to match the intensity and hence the conversion efficiency. This requirement forced a tight specification ($\pm0.5\%$) for the focal length of the spatial filter lens. About that absolute specification, all lenses of a given type are corrected during fabrication such that all focal lengths are matched to $\pm0.2\%$.

The polarization budget suggested the contrast of the polarization required for efficient splitting and amplification. The requirements for balanced beam-to-beam frequency conversion dictated the need for Brewster-angle polarizers ahead of the FCC's. Because of the precision needed, these are required in spite of the (50:1) polarization contrast the Brewster-angle disk amplifiers provide at the end of the amplifier stages. The disk amplifiers provide a relative insensitivity to depolarization early in the system.

The resultant design is a system that fits into the existing building and maximizes the use of equipment from OMEGA. (Over 90% of existing OMEGA spatial filters were used in the upgraded system.) The system includes path-length adjustments that can provide simultaneous arrival of beam pulses at the target to within ±3 ps. Individual beams can be intentionally mistimed to ±5 ns with respect to $t = 0$. Mapping the UV beams to the spherical target chamber was performed to minimize the sensitivity to variations in performance of the individual amplifiers. This mapping (discussed under *Target Area*) uses two mirrors per beam, ensures that incident angles on the mirrors are less than 60°, maintains equal path lengths from the FCC's to the target, and fits within the existing space. The system design will deliver beams with sufficient energy, quality, and alignment accuracy to attain the ultimate goal of 1%–2% nonuniformity on target.

2. Optical Components

Optical components for the OMEGA Upgrade are being procured through several major contracts with five leading optical fabrication vendors. This section summarizes the engineering effort that led to these components being specified and purchased (at budget), with their performance meeting Upgrade requirements.

The top-level requirements for the laser performance and uniformity dictated an array of lesser requirements for appropriate beam profiles and energy levels at the target while minimizing fluences throughout the chain that could potentially damage optical components. From the requirements and configuration constraints, computer simulations of beam transport allowed determination of such parameters as fluence, B-integral, allowable wavefront and alignment error, and the required power balance.

Once the on-target error allowances were determined, optical engineers statistically apportioned the error among the components in the system. Budgets were made for the various types of error and used to establish surface finish and transmitted wavefront tolerances for each optical component. Once the fluences in the system were known, the optical material for each component could be chosen. The choice was typically between BK-7 for fluences below 2.0 J/cm^2 and fused silica for fluences above that.

Compilations of these parameters resulted in a specification control drawing (SCD) and statement of work (SOW) for each type of optical component in the Upgrade. These documents served as the basis for quotation requests from the optics vendors and as the measure of achievement for contractual obligations.

Specifications were written for the following categories of optical components:

- Spatial filter lenses

- Mirrors and beamsplitters

- Polarization control optics

- Aspheric focus lenses

- ASP optical components

The procurement cycle for each of these components required the vendor to generate plans for manufacturing, processing, cleaning, and testing of each component prior to the start of manufacturing. Source inspection, or at a minimum examination of vendor test data, has ensured that all optical components meet specifications. Typical specifications for these components (all measured at 1054 nm) are

transmitted wavefront error:	±1/10 wave
flatness (mirrors):	±1/20 wave
surface roughness:	<10 Å (rms)

3. Optical Coatings

The requirements for the OMEGA Upgrade optical coatings are discussed in the Preliminary Design Document[1] and in detail in the Optics Coating Requirements document.[2] The development of Upgrade coatings, in general, and the transport mirror coating, in particular, is described in several reports in the LLE Review.[3,4] A coating specification[5] also outlines the required tests and inspection criteria for all coated optics. A summary of the coating requirements is given in Table 57.II. The coating designations in the left column of this chart are discussed below. All the coatings have been designed, fabricated onto prototype substrates, and tested for both optical and damage specifications.

a. *IR coatings.* The coatings used in the IR (1054-nm) portion of the laser system comprise antireflection and reflector coatings. The substrates for the antireflection coatings are either BK-7 glass or fused silica depending on the incident fluence. The BK-7 substrates receive a vacuum-evaporated dielectric coating using an yttrium-oxide/silicon-dioxide design (1ωAR, 1ωAR45), while the fused silica optics are coated

Table 57.II: Coating Requirements for the OMEGA Upgrade.

Coating Designation	LC Gap	Wavelength	Incident Angle	Control Value	Reflectance		Transmittance		Max. Fluence* (J/cm^2)
					S%	P%	P%	P/S	
1ωHRSP45		1054 nm	45°	R	99.5	>99.5			5.4
1ωRSTP45		1054 nm	45°	R	>99.5	<4.0	>96		5.4
1ω99RS45		1054 nm	45°	R	99±0.5				5.4
1ω99RP45		1054 nm	45°	R			99±0.5		4.5
1ωStressAR		1054 nm	45°	R	<1.0	<0.5			5.4
1ωAR		1054 nm	0	R	<0.5	<0.5			5.6
1ωRSTP57		1054 nm	57°	T			95	500/1	5.1
1ωAR45		1054 nm	45°	R	<1.0	<0.5			5.4
LCS6.5	6.5 μ								
LCS6.5	13 μ	No Optical Requirements							
LCS9	>18 μ								
1ωARALIGN		1054 nm	0	R	<1.0	<1.0			2.9
		351 nm	0	R	>10	>10			2.9
SG1/2ωAR		703 nm (cwl)	0	R	<1.0	<1.0			2.9
SG1ωAR		1054 nm	0	R	<0.5	<0.5			5.4
SG3ωAR		351 nm	0	R	<0.5	<0.5			2.9
SG3ωAR/DPP		351 nm	0	R	<0.5	<0.5			3.6
SG3/1ωAR		351 nm/1054	0°–8°	R	<0.5	<0.5			3.6
3ωHRSP(ANG)		351 nm	0°–60°	R	>99.5	>99.5			2.9
3ωStress		No Optical Requirements							
1/2/3ωAR		351/527/1054	0	R	>85	>85			low power

cwl = center wavelength

*Note: Fluences assume 7-ns foot (F) pulse and 1.1-ns main (M) pulse.

with a porous-silica sol-gel (SG1ωAR). This high-damage-threshold (but delicate) coating was chosen on the basis of the fluence levels at the optics. The design may be modified after some experience on the glass development laser. The reflector coatings include high-reflectivity mirrors, partial reflectors, 45°-incidence polarizing beamsplitters, and 57°-incidence polarizers. These coatings are all based on a vacuum-evaporated dielectric coating using tantalum-oxide/silicon-dioxide designs. These materials have been extensively developed for high damage threshold and optical performance.

During initial manufacture of the reflector coating, stresses from the coating deformed the optic, causing these optics to fail optical surface figure testing. After several remedies were investigated, it was discovered that the best solution is a coating (1ωStressAR) that when applied to the back side of the optics produces similar stresses. This rear-side coating will be applied to all substrates coated with dielectric multilayers.

A coating process was developed to produce spacers of evaporated material for the liquid crystal devices in the system. These spacers provide better control of wedge tolerance (1.5 arc/s) in the assembled device, more accurate thickness of the liquid crystal layer (6.5 μm$\pm$0.5 μm), and faster assembly methods than the mylar spacers previously used.

The coating for the frequency-conversion crystals is a single-layer sol-gel design for the three wavelengths (SG1ωAR, SG1/2ωAR, and SG3ωAR). When applying these coatings, much of the effort is in the tooling and process development required for the dipping and spinning deposition processes. New polishing methods under consideration for these components also require developing cleaning methods to remove polishing oils.

b. UV optics. The UV (351-nm) transport optics are coated with a sol-gel antireflection coating (SG3ωAR) for the transmissive optics and a high-reflector coating [3ωHRSP(ANG)] for the transport mirrors. These sol-gel coatings have been designed, developed, and tested, and the production processes have been determined for all optics. For each application, the composition and design of the coatings will vary depending on the incidence angle of the beam and the orientation of the electric vector with respect to the coated surface. Optics having a low incidence angle and predominantly s-polarized light will use a design based on hafnium oxide/silicon dioxide. Optics that combine high incidence angle and predominately p-polarized light use a design containing more costly scan-

dium-oxide/silicon-dioxide coatings. For a given angle, each design will provide the specified reflectance with the minimum number of layers to improve damage characteristics. These designs will also be modified to reduce the time-averaged electric field in the upper layers of the coatings.

A great deal of effort has gone into the design of the substrate cleaning and storage tooling, coating tooling, testing tooling, and handling tooling to ensure that no process degrades the high-quality substrate surfaces. Preliminary results from the newly installed 1.8-m coating chamber indicate that all uniformity requirements for the Upgrade optics will be met. A substantial effort went into establishing a sol-gel coating capability for the 650 optics to be coated as well as the facility needed to clean the 2000 optics for the Upgrade.

4. Optomechanical Design

Four key design constraints drove the Upgrade's optomechanical design. The first was strain-free mounting of all optical components. The mounts generally consist of three-point, 6°-of-freedom, exact-constraint designs that prevent typical mount manufacturing, assembly, and environmental tolerances from distorting the precision optical components. The second key feature is precision pointing and centering control of optical components. These include fixed mounts, manual drives, and motorized drives that typically have microinch and/or microradian accuracy and stability requirements. The third constraint is to provide an adjustment range adequate to acquire the laser beam within the optic's clear aperture. The range must be sufficient to compensate for typical fabrication and structure installation tolerances. Finally, all optical components must be packaged within the space constraints allocated by the 60-beam OMEGA Upgrade configuration. Examples of Upgrade optomechanical designs are the periscope mirror assembly (PMA), focus lens assembly (FLAS), transport mirror mount, spatial filters, and path length adjustment system (PLAS).

5. System Alignment

The alignment of the beamline segments is performed using an IR cw alignment laser and various references (typically crosshairs) located throughout the system. These references define the beam path upon which the laser system components are located. Once the system is aligned, the alignment beam propagates through the system and defines the location and direction the pulsed beam will travel during a shot. All of the optical components in the IR system are installed and aligned using this alignment beam.

End-to-end alignment of a frequency-tripled, IR laser system such as OMEGA presents a difficult alignment problem because the relatively low-power, cw IR alignment laser will not be converted to UV by the conversion crystals. This, along with the low IR reflectivity of the Upgrade's UV transport mirrors, means that a single alignment beam cannot be used to align the system from source to target.

The Upgrade alignment system therefore uses two wavelengths, unlike the previous system that was aligned from the oscillator to the target using IR light. While two wavelengths increase the system complexity, they eliminate the two disadvantages of single-wavelength alignment: the transport mirrors no longer need dual-function (IR/UV) coatings (because UV light is used to align these optics), and the focus lenses will not have to be translated after IR alignment to compensate for chromatic shift. The former dramatically improves the damage threshold of the UV coating, and the latter improves the operational accuracy of alignment. The IR portion of the laser is aligned using a 1054-nm Nd:YLF laser, together with alignment sensor packages located at the driver and stages A, C, and F within each beamline. For alignment of the UV portion of the system, a full-aperture, 351-nm cw laser is injected into the beam after the FCC's and just before the omnichromatic F-ASP's. This is done with movable mirrors located in the target bay. Co-alignment of this injected beam to the IR pulsed beam is performed using the F-ASP. An alignment sensor package located on the UV alignment table (UVAT) measures the alignment of the injected UV beams.

a. IR alignment. The following basic processes will be necessary to routinely align the IR beamlines:

1. Laser drivers and IR alignment laser injection
   (1 beamline segment)
2. Stage A–C pointing and centering
   (15 beamline segments)
3. Stage C–F pointing and centering
   (60 beamline segments)

Each process involves five steps: setup, image analysis, action determination, action implementation, and confirmation.

Process 1 requires the alignment laser and driver to be aligned into the A-splitter area by using an alignment sensor package in the A splitter (A-ASP). The ASP has pointing and centering references to ensure that the beam entering the stage-A splitter has the correct direction and position to propa-

gate down the laser beamline. The driver injection is done after the alignment of the laser driver (not part of this procedure) and is necessary to propagate a driver beam into the laser chain. The backlighter driver is injected into the middle A–C segment and is aligned by the stage-A ASP. This injection is a somewhat manual process and is not part of the automated alignment routine. The following hardware is required: laser drivers, infrared alignment table (IRAT), and A-ASP.

Process 2, the alignment of the segment from the stage-A splitter to stage-C ASP, involves the alignment of the beams propagating from east to west in the laser bay and is performed using the alignment laser after it has been injected. This process is depicted in Fig. 57.18. Process 3 aligns the last portion of the IR system, the stage-C splitter to F-ASP, and is depicted in Fig. 57.19.

When all three sections are complete, the operator is assured that the centering reference at the end of the driver line has been transferred (within tolerances) to the centering fiducials at the F-ASP. This, coupled with the intermediate centering checks, ensures that the beam will not be vignetted on any optics in the laser chain. Similary, the beam pointing in all stages is checked, corrected, and verified. The final IR pointing and centering positions are recorded by the F-ASP to be used as a reference for the UV alignment process.

b. UV alignment. The periscope mirror assembly (PMA) and the F-ASP are the major elements in the UV scheme. The PMA includes the UVAT and a system that positions a set of mirrors near the face of the shield wall in front of the F-ASP's. In each position, these mirrors form a periscope that injects a UV alignment beam, which originates in the UVAT, into one of the 60 beamlines at the input end of its F-ASP. After the UV beam is correctly aligned to the fiducial in the F-ASP, it is transmitted to the target chamber and retro-reflected to a video camera that is part of the UV-ASP on the UVAT. (The beam may also be transmitted back to the UVAT via the opposing beamline that has also been accessed by the PMA.) The video signal is processed to provide position-error data that is used to drive the motorized end-mirror and target-mirror mounts to correct the pointing and centering of the beam or to adjust the focus lens in the FLAS. The PMA mirrors are then re-positioned to inject the alignment beam into another beamline.

The following basic processes will be necessary to routinely align the UV optical trains to correctly deliver the shot pulse to the target:
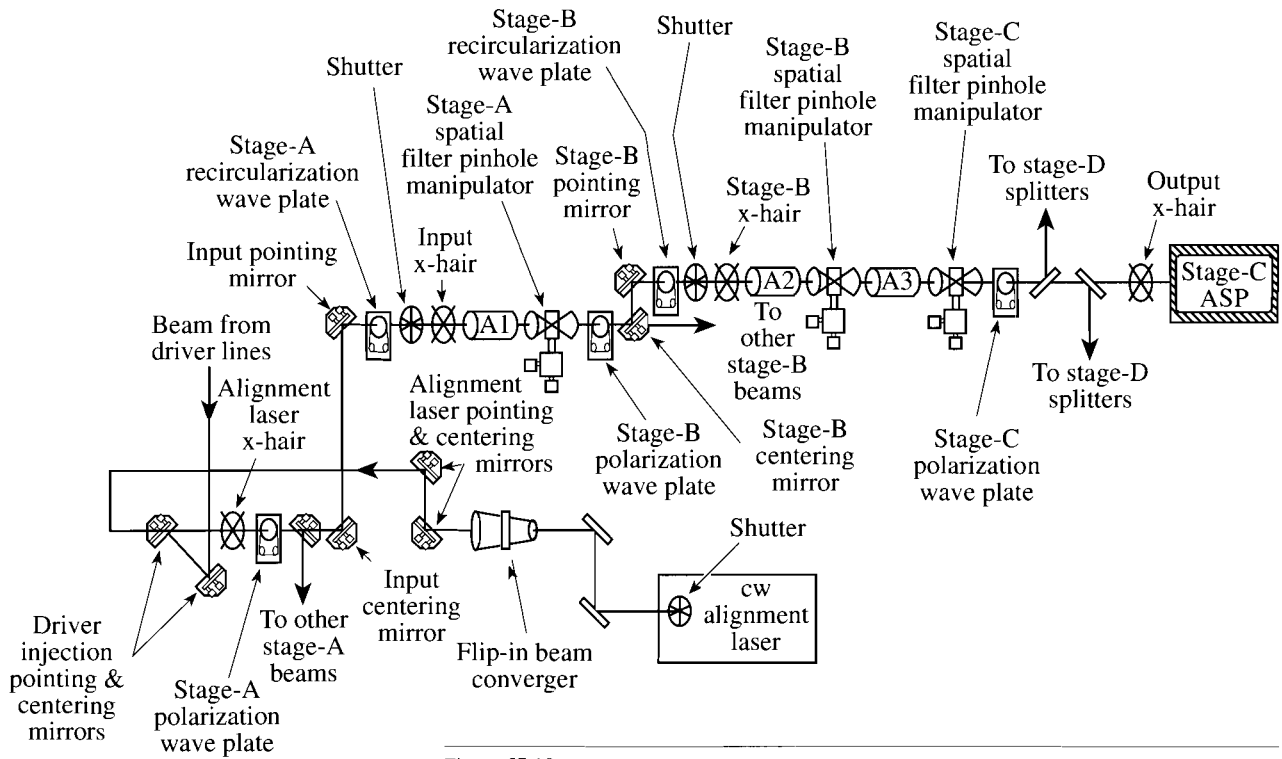
Stage-B
recircularization
Shutter   wave plate   Shutter   Stage-B   Stage-C
                                                  spatial   spatial
Shutter   Stage-A   filter pinhole filter pinhole
               spatial   manipulator   manipulator
Stage-A   filter pinhole Stage-B   To stage-D
recircularization manipulator pointing   Stage-B   splitters   Output
wave plate   mirror   x-hair   x-hair

Input pointing   Input
mirror   x-hair

Beam from   To
driver lines   Alignment   other
        Alignment   laser pointing   stage-B
        laser   & centering   beams   Stage-B
        x-hair   mirrors   Stage-B   centering   Stage-C
                                                         polarization   mirror   polarization
                                                         wave plate   wave plate

Driver   Input   To stage-D
injection   To other   centering   splitters
pointing &   stage-A   mirror   Flip-in beam
centering   Stage-A beams   converger
mirrors   polarization
            wave plate

                                                              Shutter

                                                         cw
                                                         alignment
                                                         laser

Figure 57.18
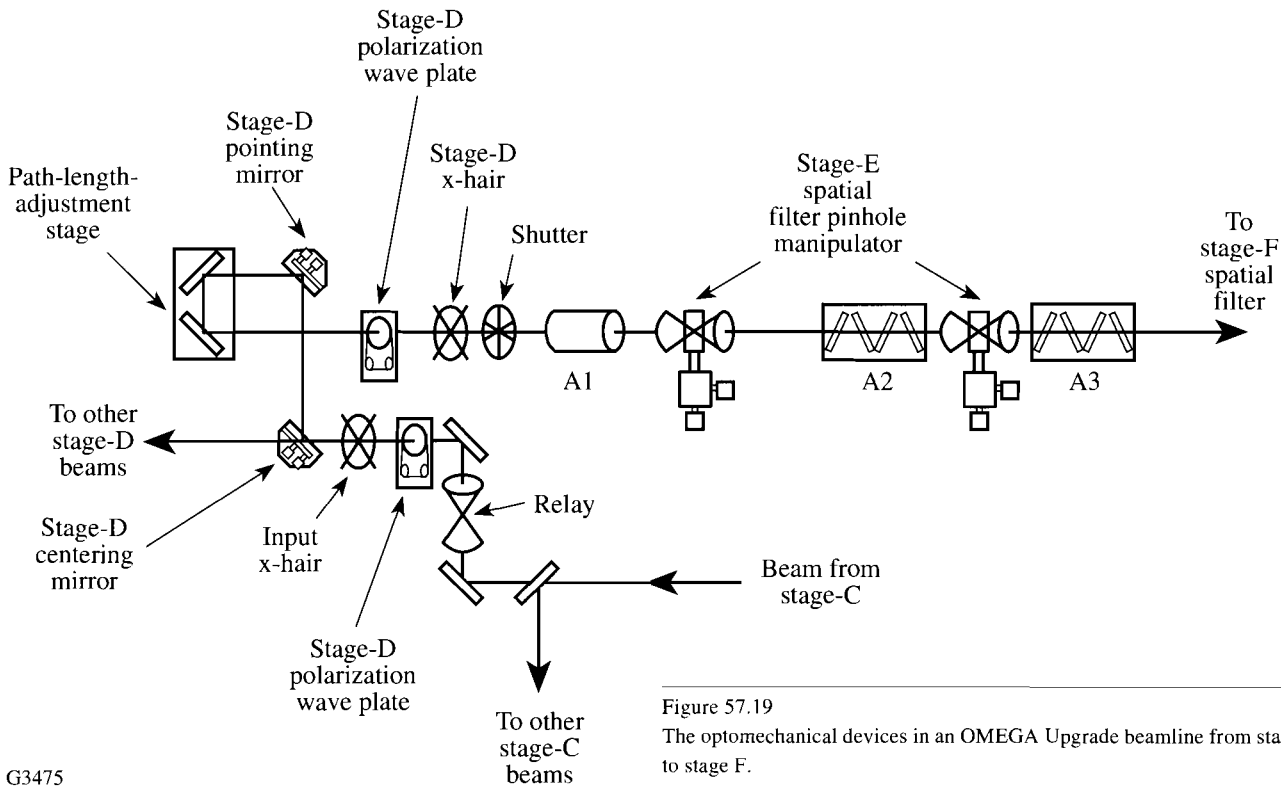The optomechanical devices in an OMEGA Upgrade beamline from the laser driver to stage C.

G3473

Stage-D
polarization
wave plate

Stage-D
pointing   Stage-D   Stage-E
Path-length-   mirror   x-hair   spatial
adjustment   filter pinhole   To
stage   Shutter   manipulator   stage-F
                                                                   spatial
                                                                   filter

                            A1   A2   A3

To other
stage-D
beams

Stage-D   Relay
centering
mirror   Input
            x-hair
                                           Beam from
                                           stage-C

Stage-D
polarization
wave plate   To other   Figure 57.19
                stage-C   The optomechanical devices in an OMEGA Upgrade beamline from stage C
G3475   beams   to stage F.

1. UVAT laser injection
2. UV transport system pointing and centering
3. Focusing

As with IR alignment, each process involves the five steps: setup, image analysis, action determination, action implementation, and confirmation. Here each process will be performed on the 60 separate beamlines, and the set-up step includes positioning and adjusting the PMA mirrors. Figure 57.20 depicts the optical configuration to perform alignment of the UV transport system. The UV alignment system will also be used to align the 60 FCC assemblies to their respective beamlines.

c. Propagation of centering errors. During the injection alignment, the alignment table and driver fiducials are centered on the system fiducial. In the A to C split alignment, the system fiducial is centered to the A fiducial and the A to the B fiducial.

To minimize the accumulation of errors, the C split to F-ASP alignment will center the A-splitter fiducial to the D-splitter fiducial and confirm the A-splitter fiducial to the F-ASP fiducial for final IR centering.

The UV targeting will center the F-ASP fiducial to the target mirror fiducial creating a total of four stages where centering errors can occur: (1) driver to system, (2) system to

cluster, (3) cluster to PMA, and (4) PMA to target mirror. The first transfer is done so that the driver line is not used for beam alignment, and the injection need not be done at the C-ASP's. The second is necessary because the system fiducial is not at an image plane and cannot be expected to have sufficient image quality for alignment past the A-split. The third transfer is necessary because targeting cannot be done in the IR. The final transfer is used to center the target mirror and the FLAS.

Wherever possible, alignment will be performed in parallel steps across the beamlines to minimize the time needed to align the entire system. It is intended to utilize the parallel structure of the control network and the image processing to minimize the time required for each alignment step. The capability to align individual or subgroups of the beamlines is still required, even though it does not use the alignment hardware to its maximum efficiency.

d. Alignment sensor packages. The alignment sensor packages (ASP's) are stable optical telescopes used to view an alignment beam propagating in a laser beamline. They monitor the alignment stability of the system by sensing the pointing of the alignment lasers, and the position of the laser beam on optical components by sensing the position of alignment fiducials (e.g., crosshairs). These fiducials can be automatically inserted into the beamline or manually attached to optomechanical assemblies such as amplifiers and spatial filters. The ASP's are also used to view the position of the
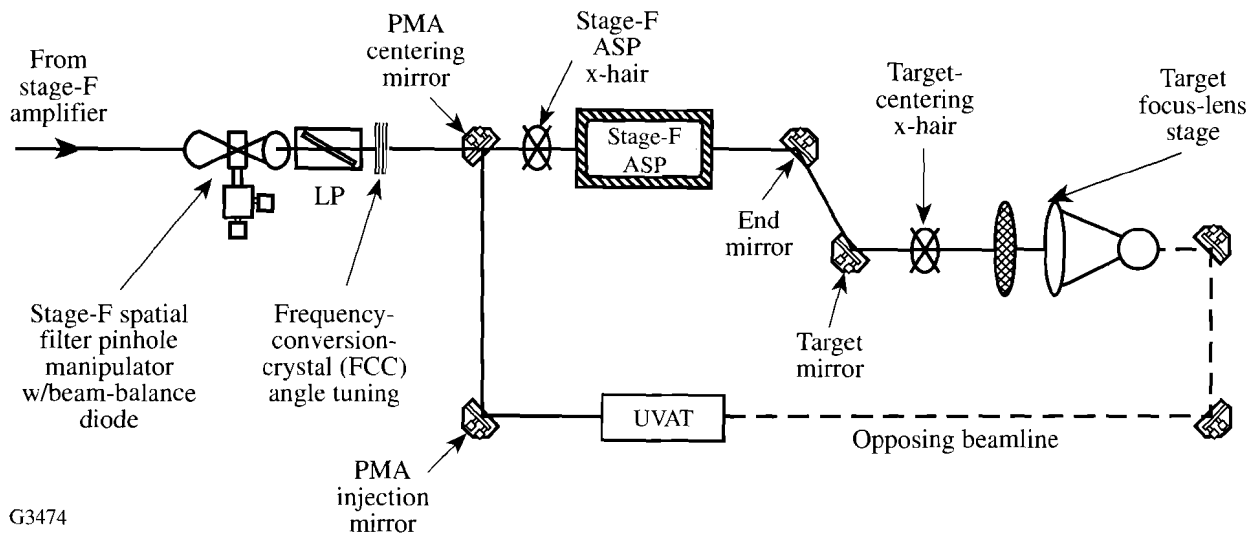
G3474

Figure 57.20
The optomechanical devices in an OMEGA Upgrade beamline from stage F to the target.

spatial filter (SF) pinholes to allow the automated alignment system to center the SF pinholes onto the beam.

The ASP's are the primary sensors for the beamline alignment system and typically reside at the ends of the beamline segments. Each ASP contains a solid-state image sensor (CCD) to view either the focus of the telescope objective (beam pointing) or the output image of the telescope, which shows the position of alignment fiducials (beam centering). Two-state devices move components within the ASP's to allow either of these functions to be performed by a single image sensor. The ASP's contain no moving or adjustable components between the entrance pupil and the point where the beam focuses on an alignment reticle. This feature provides long-term stability of the pointing reference for the beam.

To establish and maintain the beam path, the ASP's are used to view flip-in fiducials (FIF's) at the start and end of each beamline. These FIF's are surveyed into place during laser system construction and then become the reference for subsequent alignments. The ASP's locate the end fiducial relative to the image of the start fiducial to monitor beamline centering stability and maintain the beamline geometry of the laser system. Misalignments are corrected using mirrors located just before the start fiducials.

Four sets of ASP's are employed in the OMEGA laser system. A single-driver ASP resides at the end of the laser driver. A single stage-A ASP resides within the stage-A splitter. Fifteen stage-C ASP's reside at the end of the 15 beamlines that run from the B splitter to the C splitter. Sixty stage-F ASP's reside at the end of the 60 beamlines that run from the D splitter through to the FCC's. These four sets are made up of two basic types of ASP's: the driver, stage-A, and stage-C ASP's are nearly identical; the stage-F ASP is significantly different.

The driver, stage-A, and stage-C ASP's are all existing OMEGA beam diagnostic packages (BDP's) modified to sense pointing and centering with a single, solid-state detector. The top-level performance requirements for the driver, A, and C alignment sensor packages were derived from the pointing error budget, which dictated the pointing sensitivity, short-term stability, and long-term stability (drift) for these instruments. Where possible, the requirements for the driver, A-, and C-ASP's were made similar to allow common modifications to the existing BDP's and to minimize design time.

The primary function of the driver ASP is to monitor the driver alignment, particularly the coalignment of the foot and main pulses. The driver ASP must sense pointing to 1.3-μrad accuracy over a 10-mrad field of view.

The stage-A ASP monitors the injection of the driver line and IRAT beams into the laser system. It is mounted in the stage-A splitter structure and is also designed to sense pointing to 1.3 μrad over a 10-mrad field of view. This sensor must be able to diagnose beam centering (FIF position) to 0.13-mm accuracy and includes a collimation sensor to allow the collimation of the IRAT, foot-, and main-pulse drivers to be matched. This is important for the optical design (i.e., all three beams come to a common focus at the SF pinholes and at the target) as well as to maintain optimal frequency-conversion efficiency for the foot and main pulses.

The stage-C ASP monitors the alignment of the beamline segments from the B splitter to the C splitter. The stage-C ASP also must sense pointing to 1 μrad over a 10-mrad field of view and must diagnose beam centering (FIF position) and drift to 0.19-mm accuracy.

The requirements for the stage-F ASP were derived from the pointing-error budget—a systematic, top-down, allocation of the top-level pointing error of 8.33 μrad to the various components of the laser system. The driving considerations were for alignment precision (< 0.3 μrad) and pointing stability (<2.7 μrad/h). The instrument is required to meet all three of these specifications. It was also required that the F-ASP use a bare glass reflection rather than transmission through a "leaky mirror" to minimize polarization effects and maximize radiometric stability.

The precision requirement led to the choice of an effective focal length of the F-ASP objective matched to the pixel size of the detector. This, in combination with the requirement for complete absence of chromatic aberration, led to the selection of a three-mirror, off-axis, all-reflective telescope for the F-ASP objective. Although the use of a reflective telescope puts more stringent requirements on the angular stability of the optomechanical system than a refractive system would, this is compensated by the complete lack of chromatic variation of optical performance provided by an all-reflective system.

The pointing stability requirement drove the mechanical design. In general, the requirement for extreme angular stabil-

ity leads the mechanical designer to strive for symmetry in all possible aspects of the mechanical structure. The beam-to-beam spacing caused adjacent F-ASP's to be nested together in such a fashion that individual one-beam instruments would, necessarily, have been highly asymmetrical. To avoid this, ten-beam F-ASP units were designed with modular subassemblies that can be removed for off-line service as required. To further improve the stability of these instruments, the main structure was made of Harcrete™, a cast epoxy/rock composite. This material's properties include high stiffness, low thermal conductivity, excellent vibration damping, excellent dimensional stability, and the ability to be cast into complex shapes. Figure 57.21 depicts two of the cast monoliths; the one on the right is sectioned to show the optic in a single F-ASP unit. Figure 57.22 shows in detail the beam paths through one of the F-ASP's.

To avoid the problem of post-adjustment drift, the critical optical mounts were designed to be nonadjustable. Adjustable installation fixtures permit the optics to be positioned correctly and then epoxied into place, using special low-shrinkage, high-stability epoxy. The installation fixtures are then removed from the F-ASP. This scheme provides the advantages of adjustability without the associated drift problems.

The moving parts of the F-ASP are components of modular subassemblies that can be removed for off-line service. The video camera, expected to be the least reliable component of the instrument, is contained in the relay subassembly, which mounts kinematically to the F-ASP. An off-line alignment fixture adjusts and tests the relay so that it will be correctly focused and aligned when inserted into the F-ASP structure.

6. Spatial Filters

Evacuated spatial filters are used after every amplifier stage in the OMEGA Upgrade to provide image relaying and various amounts of magnification. The filter sizes depend on the beam aperture and magnification; for instance, the stage-A filter is $f/50$ and 5.6 m long, and the stage-F is $f/22$ and 10.25 m long. Aspheric lenses are used in all the large-aperture spatial filters, thereby reducing the accumulated spherical error in the system.

The spatial filters comprise five subsections: the tube weldments, the lens cells, the lens spacers, the interface package, and the pinhole manipulator. The tube weldments are 316-stainless-steel tubes with flanges and are rated for

5×10^{-6} Torr. The nominal operation pressure for the spatial filters is 2 mTorr.

The lens cells and lens spacers are mounted on each end of the weldments. The cells are one-piece annular mounts for the lens and contain two O-ring grooves for vacuum seals, one on the spacer side and the other on the lens side. The cell contains a simple, spring-loaded retainer for the lens to facilitate installation and replacement. The lens spacer is an annular aluminum cylinder used to compensate for variations in the focal length of the lenses and manufacturing tolerances of the tube weldments. Custom sizing of each spacer for a specific tube and lens pair allows the collimation of each spatial filter to be strictly maintained. The length of the spacers will be determined to ≤ 125 μm using a special fixture and collimation detector, thereby providing collimation of each spatial filter to $\lambda/4$ @ 1.054 nm.

The pinhole manipulator positions the pinhole directly at the focal point of the spatial filter, requiring adjustment in three dimensions. The pinhole manipulators from the original OMEGA system will be used on the Upgrade for stages A–D. The size and close proximity of the stage-E and F spatial filters require a new manipulator that has the slides and motors located within the spatial filter tube. The mechanical and electrical components of these manipulators are vacuum compatible.

The interface between the spatial filter and the support structure will be an air bearing that will allow the entire filter to be moved out of the beam. This will allow for the necessary removal of the spatial filters during routine alignment; quick-disconnect pneumatic fittings will make this task easier.

7. Frequency Conversion Cells

The frequency-conversion crystals (FCC's) convert the fundamental wavelength of the OMEGA laser (1054 nm) to the second- (527-nm) and third- (351-nm) harmonic wavelengths. The frequency-conversion cells have been engineered to meet the requirements established in the OMEGA Upgrade Preliminary Design Document.[1] The following describes the engineering process that led to contracts with vendors capable of supplying high-quality, frequency-conversion components.

The parameters that contribute to uniform frequency conversion were established using simulations conducted by the
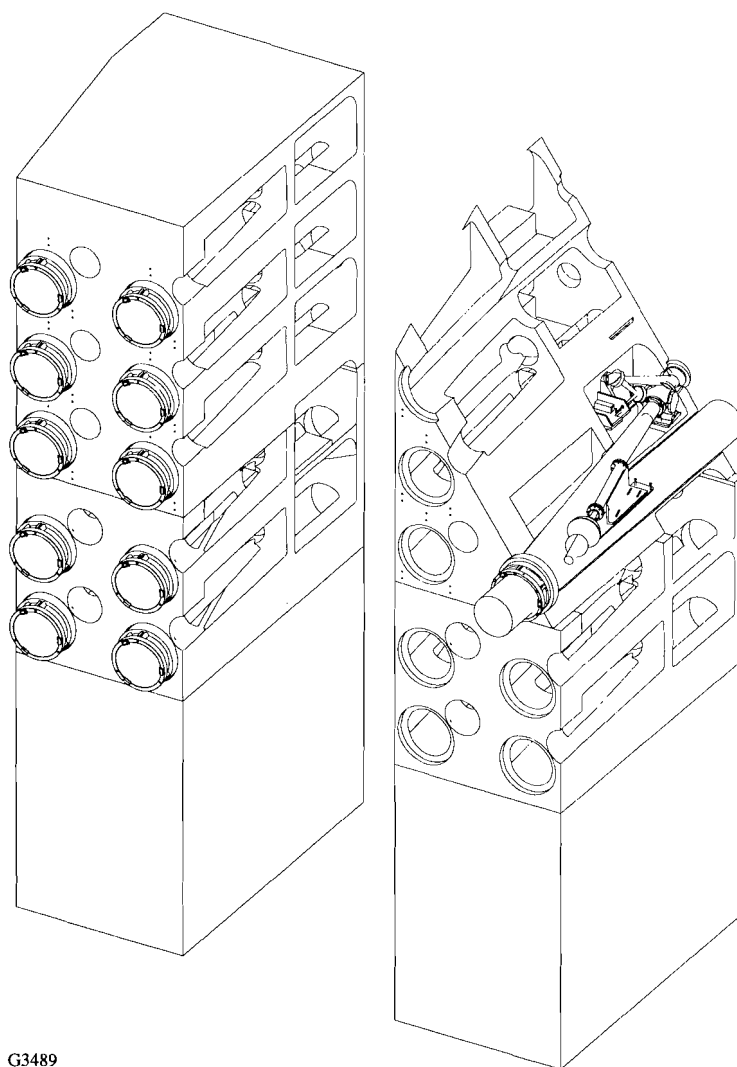
G3489

Figure 57.21
Two of the monoliths for the stage-F alignment sensor package (F-ASP), each containing ten beamlines.
A section through the right structure depicts the layout of the optics for a single beamline.

code "*MIXER*."[6] To keep losses below 0.5% of the conversion efficiency at the peak of the main pulse, where the crystals are the most sensitive to errors, the following tolerances (obtained from Table 7.4 of Ref. 1 with adjustment where appropriate by the crystal thickness ratio 12:7.6) must be achieved:

Doubler misalignment	142 μrad
Doubler wavelength shift	7 Å
Doubler temperature	0.6°C
Tripler misalignment	29 μrad
Tripler wavelength shift	0.2 Å

Tripler temperature	0.1°C
Polarization angle	±0.3°
Fraction in wrong polarization	3×10^{-5}

In the preliminary design, the doubling and tripling stages each used a thicker central crystal for efficient conversion of the foot pulse surrounded by a thinner, annular crystal for efficient conversion of the main pulse. During the detailed design, a thorough investigation and reevaluation of the required pulse shapes and the associated intensity distributions at the plane of the conversion crystals led to the selection of a single-thickness crystal, which efficiently converts both main
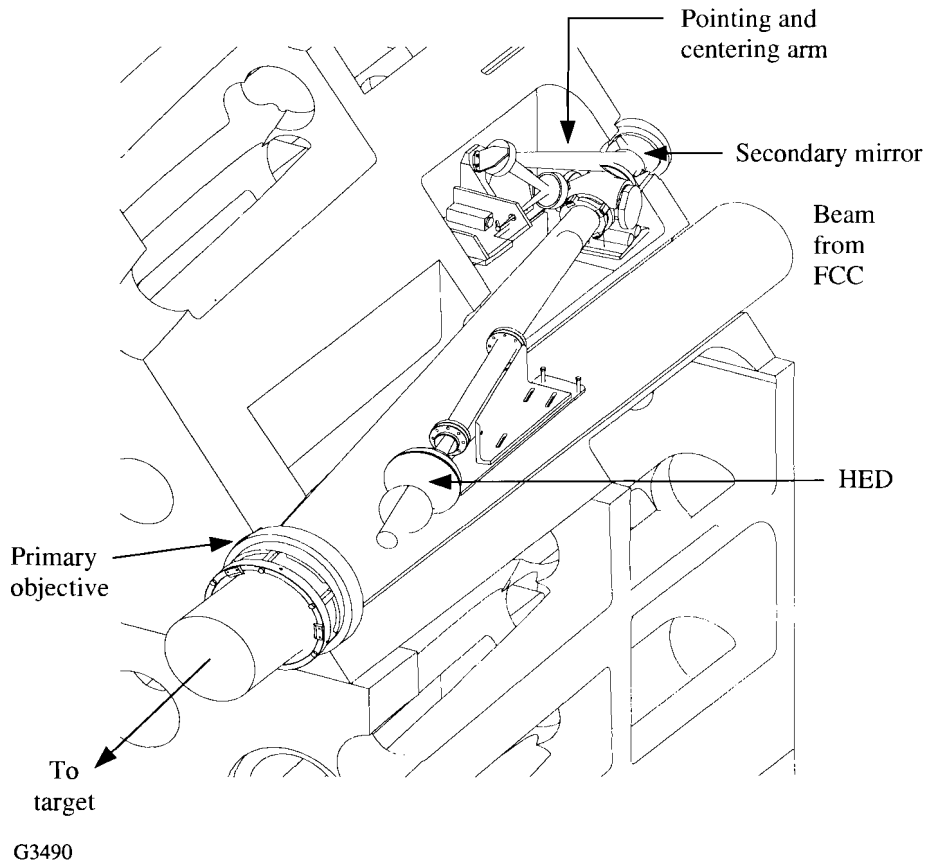
Figure 57.22
Major optical components in a stage-F alignment sensor package (F-ASP) for a single beamline.

and foot pulses and maintains the same operating parameters. This design utilizes 12-mm-thick crystals (30-cm diam) for both the doubler and tripler.

Once the crystal configuration was established, a complete specification and statement of work for the crystals was prepared using the system optical error budget. Since the crystal is a transmission optic, it should normally be subject to the same tolerances as any other optic in the system. In consideration of the different manufacturing techniques needed for these crystals, as compared with conventional optical glass elements, the error budget allocated to the FCC's was relaxed somewhat. For example, surface roughness was budgeted at 50 Å (rms) because of the difficulty in finishing KDP due to its water solubility. (However, the vendor contracted to polish the Upgrade KDP has produced a sample of KDP polished to 10-Å roughness.) The statement of work for crystals calls out the following specifications for finishing:

Transmitted wavefront error	±1/10 wave
Flatness	±1/20 wave
Surface roughness	<50 Å (rms)

The vendors were required to submit plans for manufacturing, processing, cleaning, and testing each crystal prior to the start of manufacturing. Source inspection, or at a minimum, examination of vendor test data, ensures that each crystal is produced according to specification.

Since frequency conversion is key to the efficient drive of fusion targets, the remainder of the frequency-conversion subsystem required careful design to meet the system requirements. A dielectrically coated, linear polarizer with 500:1 contrast will be placed ahead of the FCC to produce the required polarization contrast at the FCC. LLE's Optical Manufacturing section has demonstrated the ability to produce polarizers of this type. All of the optical mounts, for both the

crystals and the polarizer, will have the same stability and flexibility as the most critical optical mounts in the system. The FCC control design provides for better than 5-μrad tuning accuracy and provides for sensing of the crystal temperature, which facilitates control of the tuning angle as a function of temperature.

The FCC design includes an input window that serves two purposes: to absorb backscattered ultraviolet radiation (needed to protect the dielectric polarizer coating) and to act as a reflective alignment surface. Materials research at LLE helped determine the glass type to be used in this application; it is being manufactured to the same optical specifications as other optics.

8. Periscope Mirror Assembly

The primary function of the periscope mirror assembly (PMA) is to inject a full-aperture UV laser beam into the UV portion of the beamlines to facilitate alignment of these beams onto the target. This is necessary because the fundamental laser wavelength (1054 nm), which is used to align the IR beamlines, is not efficiently transmitted by the UV transport optics.

The 300-mm UV alignment beam originates on the UVAT and may be injected into any of the 60 OMEGA Upgrade beamlines by two sets of mobile mirrors. Two identical systems for the north and south halves of the target bay are used to reduce alignment time and, more importantly, to create a continuous optical path through opposing beams. The latter facilitates performing a multitude of alignment and calibration procedures that require reflected and transmitted UV beams. Each of the two mirror sets comprises two mirrors that move independently to inject the UVAT beam into any of the 30 beamlines located on the north or south sides of the target bay. Figure 57.23 illustrates the principal features of the PMA that services the north segment of beamlines. (The south assembly is identical.)

PMA requirements were derived from the system-level, shot-cycle time and the pointing error budget. The following key requirements have received the closest attention and have been the main drivers in the evolution of the PMA design approach:

1. Average time to position the periscope mirrors and settle transients: ≤ 15 s
2. Alignment beam coarse positioning tolerance (3 σ): pointing ≤ ±1.8 mrad, centering ≤ ±1.0 mm
3. Alignment beam fine pointing (1 σ) : ≤ ±3 μrad

4. Alignment beam pointing stability: angular drift due to PMA effects must limit total excursion to within ±3.0 μrad (1 σ) for a period of at least 40 s after acquiring the desired beam axis. Here, drift applies to
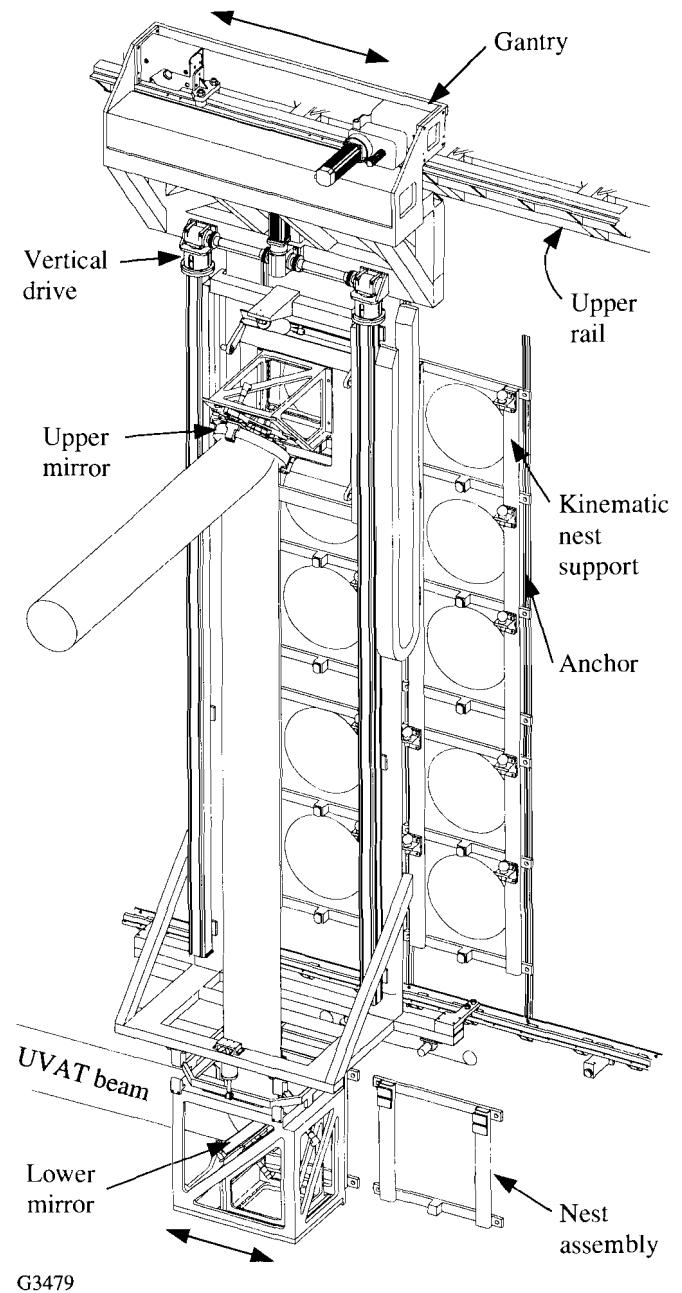

G3479

Figure 57.23
The major components for the north half of the periscope mirror assembly (PMA). The entire gantry (with the lower mirror attached) moves to each of the six columns of five beams. The upper mirror moves vertically to select a particular beamline.

beam displacements having frequency components less than 60 Hz.

Personnel safety was given highest priority followed by schedule, cost, and reliability. Also, target-bay space considerations mandated that the PMA be housed within a 1.2-m-wide corridor running along the west shield wall.

The pointing-stability requirement dictated most of this design. Based on a careful assessment of the expected shield-wall stability, kinematically ideal mounts were selected to support the periscope mirrors on the wall during alignment operations. This makes good use of the wall's great mass and intrinsic damping characteristics. Also, load paths from the periscope mirror through the mounts and into the wall were kept very short and stiff, thereby achieving high natural frequencies in spite of the large masses of the solid mirrors (5 cm × 35.5 cm × 51 cm). This avoids amplification of most wall-borne disturbances, thereby enhancing the mirror stability.

Two periscope mirror modules (PMM's), an upper and a lower, are carried by a gantry that is a major feature of each PMA system. The lower mirror directs the alignment beam to the upper mirror, which, in turn, reflects the alignment beam into the capture range of the F-ASP, i.e., into near coincidence with the desired beamline. Precision alignment with respect to the F-ASP is then accomplished by coordinated tip and tilt adjustments of both periscope mirrors using the F-ASP pointing and centering arms as references. The PMM's have built-in, two-axis micropositioners that operate under closed-loop servo control identical to those of the end and target mirrors.

A typical operational sequence for one of the gantries is as follows: Given a command from the host computer, the PMA local controller activates the horizontal drive and moves the gantry along the wall, stopping at the desired column of five beamlines. Centering and locking mechanisms are actuated to accurately position the gantry and lock it to the guide rails. While the gantry is traveling, the controller also activates a precision ball screw drive that moves the upper mirror vertically to the desired beamline. Both mirrors are then transferred to their respective kinematic nests on the shield wall and are released from mechanical contact with the gantry. This isolates the mirrors from disturbances that may otherwise be transmitted through the gantry structures. Using the F-ASP as a reference, the UV alignment beam is accurately coaligned with the primary beamline. Various alignment functions can then be performed on the UV transport system, many of which involve an ASP on the UVAT. When alignment opera-

tions at a particular beamline are complete, the mirrors are transferred back to their stowed positions aboard the gantry. The above sequence is repeated as needed for each of that gantry's 30 beamlines.

The time for repositioning at the next beamline is minimized (≤ 8 s) by using an efficient path through each 30-beam array. Although the array measures about 3 m by 6.7 m, maximum transport velocity and acceleration are only 23 cm/s and 15 cm/s^2, respectively. As a result, driving forces and transient disturbances are low despite the mass of the gantries (>900 kg each).

Coarse-positioning requirements will be met by surveying each kinematic nest into position using a surrogate mirror at each position in turn. The positional requirements in this case are well within the capabilities of current surveying practice.

For fine pointing, the PMM's incorporate the same design as the transport mirror mounts and TMM micro-positioners. To gain additional confidence, finite element analysis (TMM's) has been performed on those elements that differ somewhat from the TMM design. The deflection of the mirror surface figure is predicted to be less than 75 nm. A prototype is being constructed to verify mounting performance under PMA dynamic load conditions.

Many safety provisions have been factored into the PMA design: the PMA corridors will be fenced off with safety gates interlocked to PMA power; emergency stop lanyards will be installed inside the corridors; warning beacons and an audio alert will be activated during PMA transit; and mechanical sensors will be fitted on both sides of the gantries to provide emergency stops.

9. Focus Lens Assembly (FLAS)

The optomechanical requirements for the FLAS were determined by the optical design and the pointing error budget and are shown in Table 57.III.

The optical requirements for the FLAS were determined by the system requirements. The focus lens has a focal length of 1.8 m and functions at $f/6$. The lens and the separate vacuum window/blast shield produce less than a quarter-wave of aberration (at 351 nm) over a field of view (FOV) of ±2 mm. The FLAS design provides a location, just ahead of the lens, for a phase-conversion plate, expected to be a plane-parallel, fused silica component ~300 mm in diameter and 25.4 mm thick. The optical design must also ensure that damage-causing ghost

Table 57.III Summary of Requirements for Focus Lens Assembly

Centration of lens to port axis	0.25 mm
Maximum static tilt of lens	0.28 mrad
Blast-window thickness	25 mm
Focus range	10 mm
Maximum transverse motion (over focus range)	1.6 μm
Additional focal shift	+10 cm
Transverse vibration	<0.6 μm
Axial vibration	2.5 μm
Focus accuracy	25 μm
Surface deformation	<100 nm
Vacuum differential (supported by blast window)	760 Torr
Note: Positive motion is away from the chamber center.	

reflections do not fall on any optics for any focus lens position (over a range of ±10 mm).

The optical requirements were met with an aspheric singlet lens, designed to be free of spherical aberration when used in conjunction with a 25.4-mm-thick blast shield. The curvatures of the singlet were chosen to position the ghost reflections away from all optical components in the OMEGA Upgrade system. This selection of curvatures somewhat compromised the attainable FOV, as the lens shape that would maximize FOV (i.e., minimize coma) would have caused potentially damaging ghost reflections to fall on nearby optics. Despite this compromise, the FOV provided by the final design is ±4.5 mm, significantly exceeding the original requirement.

The FLAS subsystem is shown in Fig. 57.24. The left side depicts the entire assembly including the blast-shield retraction mechanism. The right side depicts a cutaway of the focus-lens barrels and shows the position of the focus lens and blast shield.

The optomechanical design of the FLAS was driven primarily by the transverse motion tolerance of 1.6 μm over the 10-cm focus range. Previous experience with OMEGA indicated that rolling bearings will not provide this accuracy. Designs incorporating flexures were found to possess insufficient stiffness to meet the requirements. The final design incorporates solid bearings consisting of polymer pads (i.e., Rulon™ or Vespel™) running against polished steel ways. Analysis shows that this design will provide sufficient stiffness and linearity of motion to satisfy the requirements.

To meet the centration requirements, as well as permit alignment of the focus axis to the center of the chamber, adjustments have been provided on the bearing pads. Datum surfaces on the end of the lens barrel will enable accurate location of the optical axis of the lens with respect to the axis of the focus motion on the mount, allowing alignment of both to the center of the chamber within tolerance.

One of the main challenges of this design was the additional requirement that the vacuum window, a 325-mm-diam × 25-mm-thick plano optic that also serves as the blast shield, be removed frequently for service. In operation, this optic will need to be changed or cleaned on a regular basis as it becomes contaminated and/or damaged. To achieve the necessary stiffness and pointing accuracy, the FLAS has to be fairly large; it nearly fills the space between the target chamber and the target mirror structure (TMS). As a result, space constraints in the vicinity of the target chamber make it impossible for one to reach in and remove the blast shield directly. A mechanism was designed that clamps and unclamps the blast-shield-to-target-chamber interface under remote control. This mechanism also transports the blast shield from the target chamber to the exterior of the TMS, where it can be grasped and removed. The mechanism works in reverse to return a blast shield from the outside face of the TMS to the target chamber, where it is correctly positioned and clamped to initiate the vacuum seal.

Major Structures Design

The major structures produced for the Upgrade include laser bay structures (23 unique designs, 74 total structures) and target bay structures (8 unique designs, 19 total structures).
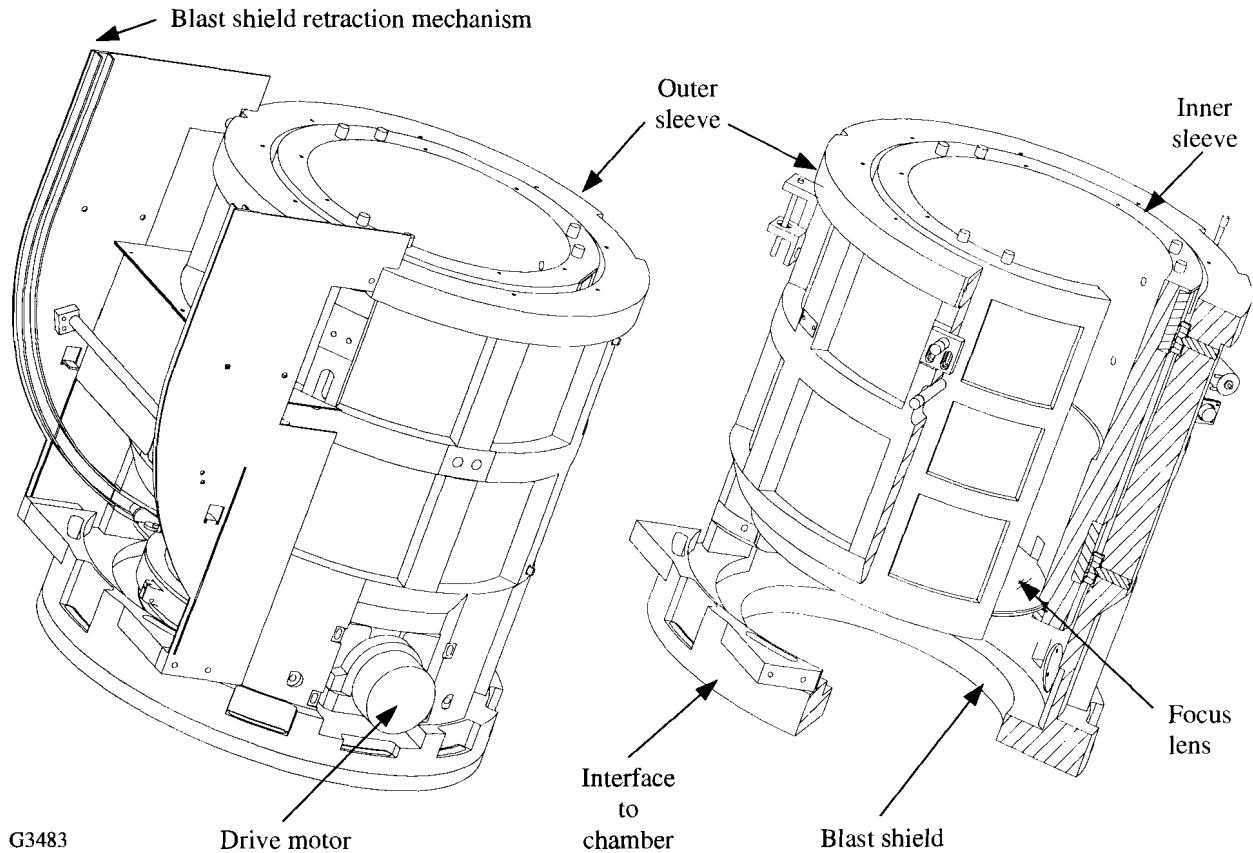
Figure 57.24
The focus lens assembly (FLAS) for the OMEGA Upgrade. On the left is the entire assembly including the blast-shield retraction mechanism. On the right is a section of the two sleeves showing the position of the focus lens and blast shield.

The key structural design requirements were

- accurately located mounting surfaces for the optical components, diagnostics, and instrumentation,

- microinch and microradian stability to the bay's thermal and vibration environments, and

- packaging and servicing of the optical components and diagnostics within the constraints of the 60-beam configuration.

The approach used to mount and accurately position the optical components is as follows: (1) The structures are typically designed to be manufactured with critical mounting surfaces located to ±3 mm relative to surveyor pads provided on the structures. (2) The structures will be surveyed into place to accuracies of ±3 mm. (3) Finally, the optical components have been typically designed to provide >±3-mm mounting

adjustment and/or excess clear aperture. This adjustment range/excess clear aperture is adequate to compensate for the structure's fabrication and installation tolerances, thus assuring that the optical system can be set up and aligned.

The requirements for pointing stability are among the most challenging. For reflective optics, allowable rotations of structural mounting surfaces are ±1.5 μrad, and for refractive optics, structural deflections must be within ~0.25 μm. These goals must be met given the following environmental conditions: ±1°C temperature variations and vibration accelerations of up to 20 μg, with major peaks at 15, 20, and 30 Hz. The basic structural approach uses massive, steel space-frame structures grouted to the floor and extensive finite element analysis. An example of this space-frame approach is the target mirror structure, which uses a 3-D "soccer ball" concept to accommodate the Upgrade's 60 laser beams and provide the needed stiffness and mounting surfaces.

One notable exception to the space-frame approach is the F-ASP structure. This unique structure serves as the pointing reference for the entire laser system and, as such, has exceptional stability requirements. Its off-axis optical system has also contributed additional unique requirements to the mechanical design. The approach has been to "cast" a structure around the optical system using a structural epoxy composite, a material commonly used for machine tool bases. This material and process provide a combination of high thermal and vibration damping with the ability to accurately mold critical off-axis optical mounting surfaces into the structure.

Servicing the laser and target systems is complicated by the requirement to package the Upgrade's 60-beam laser into the facility built for the original 24-beam OMEGA system. This has resulted in structures ranging in height from 3.6 m to 9 m bordered by long aisle ways 1.2 m or less wide. One of the most difficult challenges involved servicing the disk amplifiers,

which are 2 m long and weigh nearly 450 kg. Each amplifier has 32 high-voltage electrical cables, each about 13 mm thick, plus numerous cooling and nitrogen-purge lines attached. Since complete amplifiers must be replaced on a routine basis, safety, reliability, and ease of operation were essential requirements of the design. The resulting structure design is a combination of swinging doors and an overhead crane (both integral parts of the structure) for service and removal of the amplifiers (see Fig. 57.25).

A rather challenging design task was the three-level platform (see Fig. 57.26) for servicing the target mirror structure and target chamber. Key issues were to avoid obstructing the many crossing laser beam paths (see Fig. 57.29) and provide room for the diagnostics, crane-load landing areas, work areas, and storage areas. All these had to be accommodated while maintaining safe access and egress for personnel.
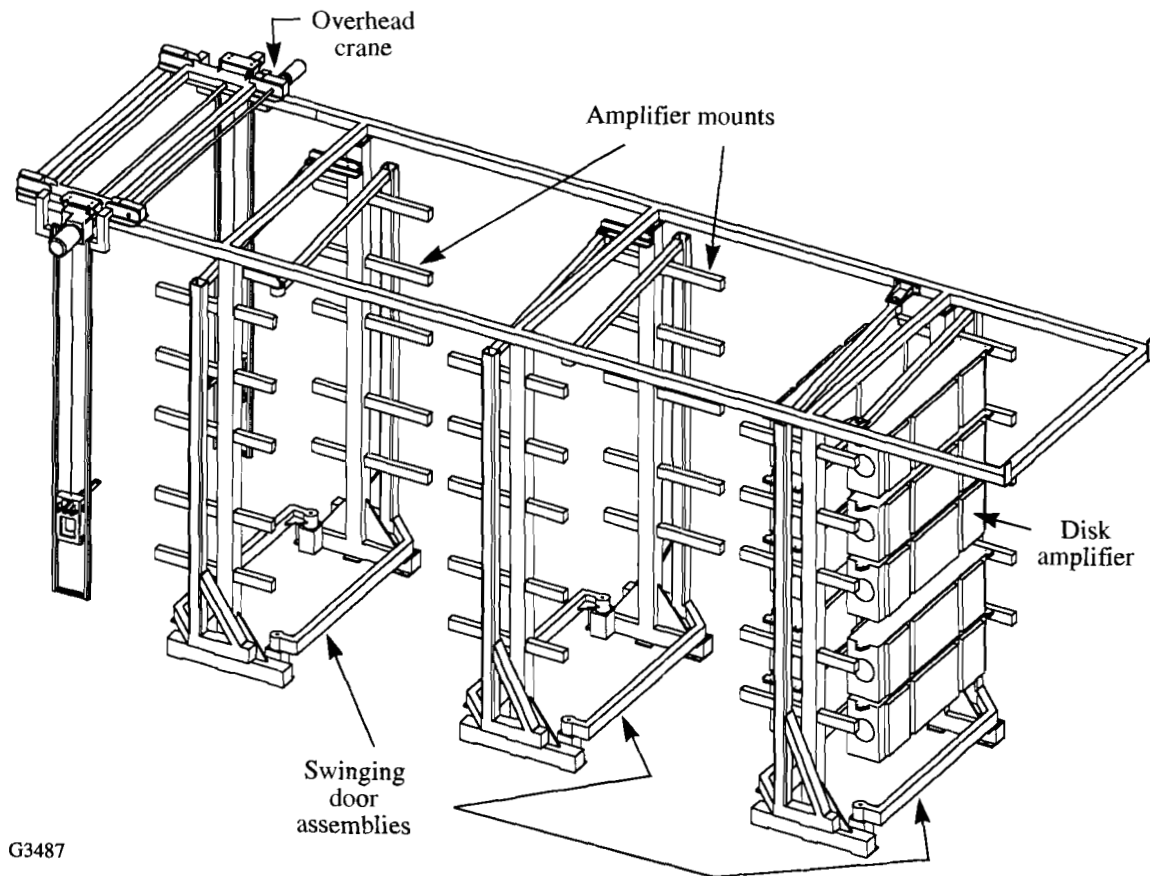

G3487

Figure 57.25
One of the four structures that support the stage-E and stage-F disk amplifiers. Each structure has six doors, each of which can swing out any or all of the five amplifiers, and a crane that lowers the amplifiers to floor level to facilitate routine maintenance.
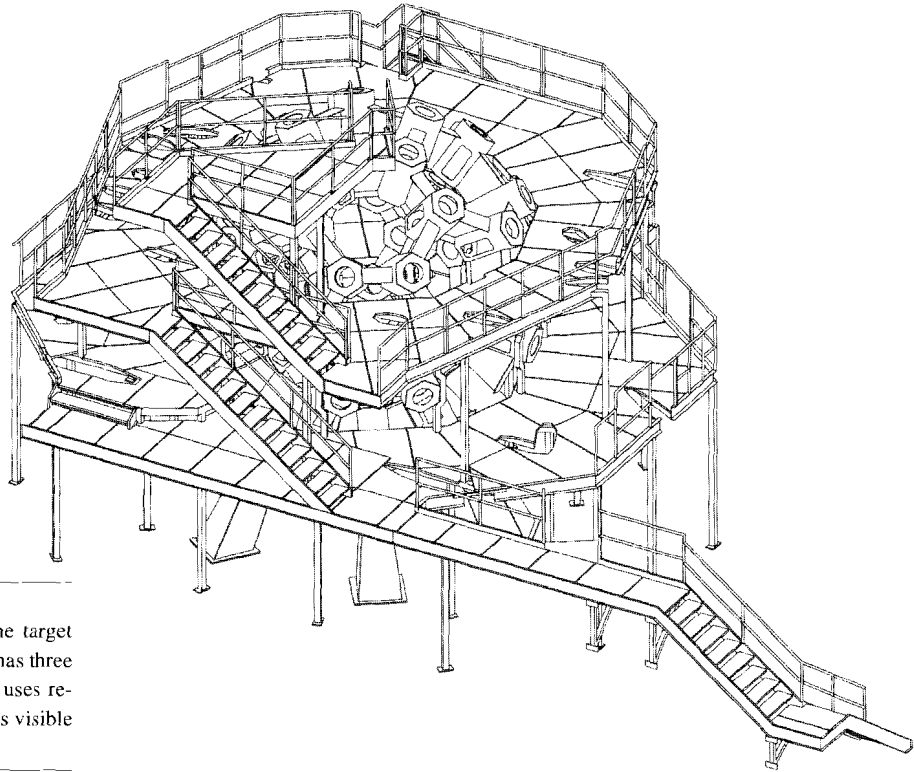
Figure 57.26
The personnel service platform for the target mirror structure (TMS). The platform has three levels, is isolated from the TMS, and uses removable grids for flooring. The TMS is visible within the platform structure.

Target Area

The layout of the target area was dominated by the requirements to deliver 60 UV beams to the target chamber and to provide access to the chamber for implementation of experimental devices on the target chamber. It is in the target bay where the use of the existing building constrained the design the most.

The target mirror structure (see Fig. 57.27) is highly modular, with five-fold rotational symmetry about the vertical axis reflecting the soccer-ball symmetry, i.e., 20 hexagons and 12 pentagons. The 60 laser beams are located at the vertices of those polygons. The laser beams are directed through hexagonal tubes that are part of the structure. The design provides for segmented personnel platforms and integrates the optical mounts with structurally rigid, hexagonal beam tubes. The target mirrors are mounted on the ends of these beam tubes. The structure has a 6-m diameter, with the target mirrors centered on a 7.2-m diameter. The beam-transport geometry is such that no angle of incidence, at either an end mirror or a target mirror, exceeds 60°. The end mirrors are held on two, separate, space-frame structures. Surrounding the TMS is a three-level personnel platform that provides access to the ports on the chamber, landing points for crane-hoisted mate-

rial, and mounting points for ancillary diagnostic support systems (see Fig. 57.26).

The Upgrade's target-area design actually allows a greater free volume for the placement of diagnostic instruments than was the case on OMEGA because in the Upgrade the beams are transported to the TMS from the outside rather than between the target mirrors and the target chamber.

The UV transport system utilizes two mirrors per beam to direct the beam to the target. The two-mirror configuration was chosen for economy and to reduce the in-air path length of the UV beam. The latter was needed to ensure that the intensity-length product for the beam was below the threshold for stimulated rotational Raman scattering (SRRS).[7] Since UV light is used to align the UV transport system, the optical coatings for the transport mirrors can be optimized for UV radiation only. In the previous system the mirrors had to reflect a nominal amount of IR energy. Relaxing this requirement has allowed the design of the mirrors to provide maximum damage resistance.

The task of mapping the 60 nearly parallel beamlines to the spherical target geometry had two fundamental constraints:
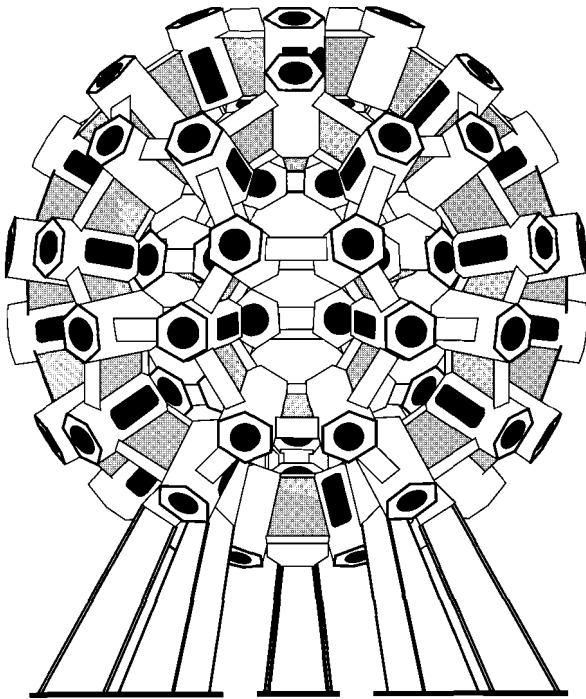
G3115

Figure 57.27
The target mirror structure (TMS) has the soccer-ball geometry defined by the beam positions. The target chamber is supported and enclosed by the TMS. Each of the 60 beams enters the TMS through the radial hexagonal tubes. The 32 diagnostic ports are located in the hexagons and pentagons of the TMS.

All 60 beams should have nearly equal path lengths, and no incident angle (on the mirrors) could be greater than 60°. Given these constraints it is a straightforward process to map a beam to a target port and then locate the end mirror along the beamline to obtain the proper path length.

For the sake of irradiation uniformity, an additional optimization was imposed upon the mapping. This entailed reducing the proximity of beams that share the same stage-A amplifiers. This is to reduce the effect any variation in the performance of a single, stage-A amplifier (distributed into 20 beams) has on target irradiation uniformity. A mapping that grouped many such beams in one area of the target would accentuate the effect a stage-A amplifier has on target performance. To mitigate this effect the beam mapping was arranged such that, for a given hexagon on the TMS, no more than three beams share the same stage-A amplifier. For the pentagons, only two such beams are allowed. Figure 57.28 is a sinusoidal projection of the beam

locations indicating which beams share each of the three stage-A amplifiers.

The beam paths, as mapped by the above constraints, are shown in Fig. 57.29. The convergence of 60 beams in the existing target bay leads to a high density of beams. The need to place structures and mirror mounts in that volume without obstructing any beam is a significant design constraint. Extensive 3-D CAD models were required for nearly every design task in this area.

1. Target Chamber
Located within the TMS is the 3.3-m-diam target chamber. The chamber was fabricated to high tolerance, which allows it to be used as an alignment reference for construction of the TMS and the installation and alignment of the target mirrors and FLAS. Post-fabrication measurements indicate that the target chamber ports are positioned to better than ±75 μrad, which is a factor of 2 better than the specification.

Note: The following systems are not part of the OMEGA Upgrade Project; rather, they will be completed as part of the LLE mission. A brief description of these systems is provided for completeness.

2. Target Chamber Vacuum System
During shot operations, the target chamber will be maintained at a vacuum $<6 \times 10^{-6}$ Torr. The vacuum system is fully redundant, with a pair of three-stage, 2000-CFM roughing pumps and three closed-cycle helium cryogenic pumps. When necessary, the chamber will be vented to atmosphere with dehumidified air. The vacuum system will be controlled by a programmable-logic-controller (PLC)-based, distributed control system interfaced to the experimental-system executive computer. The main vacuum system will be capable of pumping the target chamber from atmospheric pressure to shooting vacuum ($<9 \times 10^{-6}$) in under 60 min. The redundant design of this system will support experiments with extremely long durations at high vacuum.

3. Target Positioning/Viewing
Ambient-temperature targets of all foreseeable configurations will be positioned by a multiaxis, air-locked target positioner and a multiaxis, optical target-viewing system. Each of the two target-viewing systems features a variable-magnification telescope and an actively configurable reticle. Multiple image detectors on each channel will be supported.
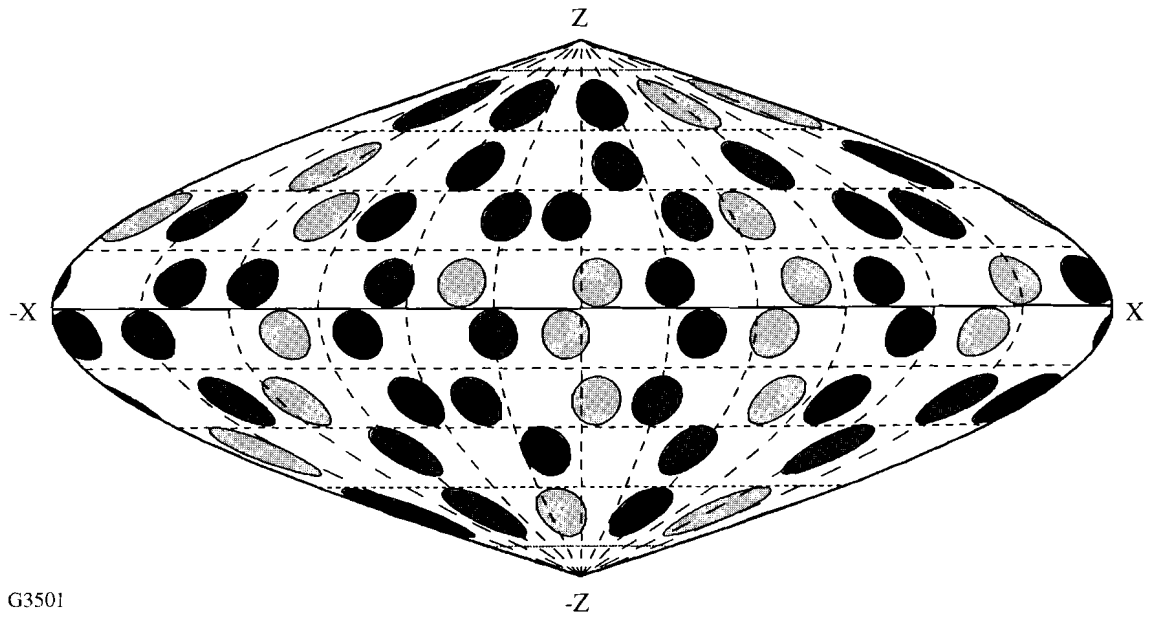
G3501

Figure 57.28
A sinusoidal projection of the beam locations on the OMEGA Upgrade target sphere. Each beam is identified by the stage-A amplifier (3 in total) from which it originates. The beam mapping was arranged so that any given TMS hexagon has at most three beams originating from the same stage-A amplifier; the pentagons have at most two beams.
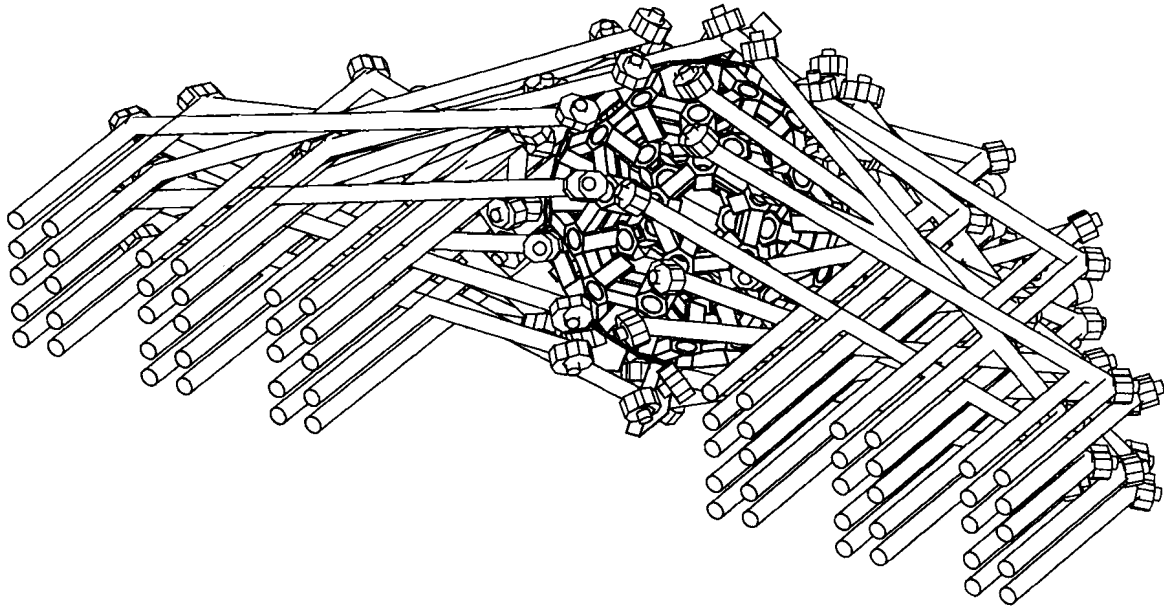
G3160

Figure 57.29
The beam paths of the UV transport system of the OMEGA Upgrade. Each beamline has two mirrors, an end mirror and a target mirror. Care was taken to ensure that all path lengths were nearly equal and that the angle of incidence on all mirrors was < 60°.

The target-viewing system will employ sophisticated image-processing techniques to provide enhanced-open-loop and automated-closed-loop target-positioner operation. The load/lock target positioner will allow selection of any target in the LLE inventory and thus will support long-duration, continuous experimental operations.

The integrated target-viewing and positioning system will allow placement of the target within a 5-μm radius of the designated center of the target chamber under either manual or automatic control.

4. Diagnostic Support Systems

Target diagnostic systems will be supported on the OMEGA Upgrade by an array of modular support systems, including mechanical interfaces, timing, vacuum, power, and control system support. The standardized interface scheme employed in the OMEGA Upgrade experimental support systems provides for simplified compatibility requirements for NLUF users and a readily reconfigurable experimental system to support future experimental programs. The <u>diagnostics to be used on the Upgrade are not within the scope of this project</u>. Information on these systems can be found in the LLE five-year plan.[8]

REFERENCES

1. R. S. Craxton, ed., *OMEGA Upgrade Preliminary Design*, Laboratory for Laser Energetics Report DOE/DP 40200-101, University of Rochester (1989).

2. Optics Coating Requirements Document, OMEGA Upgrade No. M-AA-G-05, Rev A, 12 October 1992.

3. LLE Review **44**, 219 (1990).

4. LLE Review **51**, 139 (1992).

5. Optical Coating Specification Document, OMEGA Upgrade No. M-AA-G-07, 28 April 1993.

6. R. S. Craxton, IEEE J. Quantum Electron. **QE-17**, 1771 (1981).

7. M. A. Henesian, C. D. Swift, and J. R. Murray, Opt. Lett. **10**, 565 (1985).

8. Proposal for Renewal Award for Cooperative Agreement DE-FC03-85-DP402000 (US DOE/LLE, October 1991), Chaps. 3.3 and 3.4.

PUBLICATIONS AND CONFERENCE PRESENTATIONS

---------------------------------- **Publications** ----------------------------------

S. Alexandrou, C.-C. Wang, T. Y. Hsiang, M. Y. Liu. and S. Y. Chou, "A 75-GHz Silicon Metal-Semiconductor-Metal Schottky Photodiode," Appl. Phys. Lett. **62**, 2507 (1993).

J. J. Armstrong and T. J. Kessler, "Large-Aperture High-Efficiency Holographic Gratings for High-Power Laser Systems," in *Laser Coherence Control: Technology and Applications*, edited by H. T. Powell and T. J. Kessler (SPIE, Bellingham, WA, 1993), Vol. 1870, pp. 47–52.

R. Betti, R. L. McCrory, and C. P. Verdon, "Stability Analysis of Unsteady Ablation Fronts," Phys. Rev. Lett. **71**, 3131 (1993).

Y.-H. Chuang, T. J. Kessler, and S. Skupsky, "Laser-Beam Pulse Shaping Using Dispersive Spectral Filtering," in *Laser Coherence Control: Technology and Applications*, edited by H. T. Powell and T. J. Kessler (SPIE, Bellingham, WA, 1993), Vol. 1870, pp. 34–46.

R. S. Craxton, F. S. Turner, R. Hoefen, C. Darrow, E. F. Gabl, and Gar. E. Busch, "Characterization of Laser-Produced Plasma Density Profiles Using Grid Image Refractometry," Phys. Fluids B **5**, 4419 (1993).

A. Denysenko, S. Alexandrou, C.-C. Wang, D. K. Bradley, W. R. Donaldson, T. Y. Hsiang, R. Sobolewski, and P. M. Bell, "Picosecond Electrical Characterization of X-Ray Microchannel-Plate Detectors Used in Diagnosing Inertial-Confinement-Fusion Experiments," Rev. Sci. Instrum. **64**, 3285 (1993).

T. Gong, Y. Kostoulas, L. X. Zheng, W. Xiong, W. Kula, R. Sobolewski, and P. M. Fauchet, "Femtosecond Optical Nonlinearities in $YBa_2Cu_3O_{7-x}$," in *Ultrafast Pulse Generation and Spectroscopy*, edited by T. R. Gosnell et al. (SPIE, Bellingham, WA, 1993), Vol. 1861, pp. 355–362.

D. Gupta, W. R. Donaldson, and A. M. Kadin, "Fast Optically Triggered Superconducting Opening Switches," in *Optically Activated Switching III*, edited by H. T. Powell and T. J. Kessler (SPIE, Bellingham, WA, 1993), Vol. 1873, pp. 139–143.

D. Gupta, W. R. Donaldson, and A. M. Kadin, "High-Temperature Superconducting Opening Switches," in the *Proceedings of the Fifth SDIO/ONR Pulse Power Meeting 1992* (Office of Naval Research, Arlington, VA, 1993), pp. 75–82.

M. Kauranen, A. L. Gacta, and C. J. McKinstrie, "Transverse Instabilities of Two Intersecting Laser Beams in a Nonlinear Kerr Medium," J. Opt. Soc. Am. B **10**, 2298 (1993).

J. H. Kelly, M. J. Shoup III, M. M. Tedrow, and K. Thorp, "Energy Transort in a Modern Disk Amplifier," in *Solid State Lasers III* (SPIE, Bellingham, WA, 1992), Vol. 1627, pp. 286–297.

T. J. Kessler, Y. Lin, J. J. Armstrong, and B. Velazquez, "Phase Conversion of Lasers with Low-Loss Distributed Phase Plates," in *Laser Coherence Control: Technology and Applications*, edited by H. T. Powell and T. J. Kessler (SPIE, Bellingham, WA, 1993), Vol. 1870, pp. 95–104.

L. E. Kingsley and W. R. Donaldson, "Numerical Analysis of Electric Field Profiles in High-Voltage GaAs Photoconductive Switches and Comparison to Experiment," IEEE Trans. Electron Devices **40**, 2344 (1993).

B. S. W. Kuo and A. W. Schmid, "Effects of Thin-Film Thermal Conductivity on the Optical Damage Threshold of a-Si Film on c-Si Substrate at 1064 nm," J. Appl. Phys. **74**, 5159 (1993).

Y. Lin, T. J. Kessler, J. J. Armstrong, and G. N. Lawrence, "Laser System Power Balance Effects from Stimulated Rotational Raman Scattering in Air," in *Laser Coherence Control: Technology and Applications*, edited by H. T. Powell and T. J. Kessler (SPIE, Bellingham, WA, 1993), Vol. 1870, pp. 14–25.

J. C. Mastrangelo and S.-H. Chen, "New Thermotropic Chiral Nematic Polymers. 3. Copolymers Containing Cyanobiphenyl Group and (S)-(-)-1-Phenylethanol or (S)-(–)-1-Phenylethylamine," Macromolecules **26**, 6132 (1993).

R. L. McCrory, J. M. Soures, C. P. Verdon, T. R. Boehly, D. K. Bradley, R. S. Craxton, J. A. Delettrez, R. Epstein, R. J. Hutchison, P. A. Jaanimagi, S. D. Jacobs, J. H. Kelly, R. L. Keck, T. J. Kessler, H. Kim, J. P. Knauer, R. L. Kremens, S. A. Kumpan, S. A. Letzring, F. J. Marshall, P. W. McKenty, S. F. B. Morse, W. Seka, R. W. Short, M. D. Skeldon, S. Skupsky, and B. Yaakobi, "Direct-Drive Laser Fusion Target Physics Experiments," in *Plasma Physics and Controlled Nuclear Fusion Research*, 1992 (IAEA, Vienna, 1993), Vol. 3, pp. 31–38.

C. J. McKinstrie, X. D. Cao, and J. S. Li, "Nonlinear Detuning of Four-Wave Interactions," J. Opt. Soc. Am. B **10**, 1856 (1993).

E. A. Murphy, H. E. Elsayed-Ali, K. T. Park, and Y. Gao, "Temperature-Dependent X-Ray Photoelectron Diffraction of Pb(100): Experimental Results and the Single-Scattering Cluster Model," J. Vac. Sci. Technol. A **11**, 3106 (1993).

J. Peatross and D. D. Meyerhofer, "Novel Gas Target for Use in Laser Harmonic Generation," Rev. Sci. Instrum. **64**, 3066 (1993).

L. Shi and S.-H. Chen, "New Thermotropic Liquid Crystal Polymers Containing High Birefringence Cyanotolan Moiety," Macromolecules **26**, 5840 (1993).

M. D. Skeldon and S. T. Bui, "Temporal Pulse-Width Control of a Regenerative Amplifier with Intracavity Etalons," in *Intracavity and Extracavity Control of Laser Beam Properties*, edited by R. L. Facklam, K. H. Guenther, and S. P. Velsko (SPIE, Bellingham, WA, 1993), Vol. 1869, pp. 120–127.

S. Skupsky and T. J. Kessler, "Strategies for Ultra-High Laser Uniformity Using Zero-Correlation Phase Masks," in *Laser Coherence Control: Technology and Applications*, edited by H. T. Powell and T. J. Kessler (SPIE, Bellingham, WA, 1993), Vol. 1870, pp. 112–119.

B. Soom, H. Chen, Y. Fisher, and D. D. Meyerhofer, "Strong K_α Emission in Picosecond Laser-Plasma Interactions," J. Appl. Phys. **74**, 5372 (1993).

M. Yu, C. J. McKinstrie, and G. P. Agrawal, "Instability Due to Cross-Phase Modulation in the Normal Dispersion Regime," Phys. Rev. E **48**, 2178 (1993).

Forthcoming Publications

S. Alexandrou, C.-C. Wang, R. Sobolewski, and T. Y. Hsiang, "Generation of Subpicosecond Electrical Pulses by Nonuniform Illumination of GaAs Transmission Line Gaps," to be published in the *IEEE Journal of Quantum Electronics*.

J. J. Armstrong and T. J. Kessler, "Holographic Generation of High-Efficiency, Large-Aperture, Transmission Diffraction Gratings," to be published in *Applied Optics A*.

D. P. Butler, W. N. Maung, W. Xiong, W. Kula, and R. Sobolewski, "Microwave Properties of Monolithic Y-Ba-Cu-O Transmission Line Devices Fabricated by the Laser-Writing Patterning Technique," to be published in SPIE Vol. 2156: *High-T_c Microwave Superconductors and Applications*.

X. D. Cao and D. D. Meyerhofer, "Soliton Collisions in Optical Birefringent Fibers," to be published in the *Journal of the Optical Society of America B*.

Y.-H. Chuang, T. J. Kessler, S. Skupsky, and D. L. Brown, "Shaping of Nanosecond, Linearly Chirped Pulses," to be published in the *IEEE Journal of Quantum Electronics*.

J. A. Delettrez, D. K. Bradley, and C. P. Verdon, "The Roles of the Rayleigh-Taylor Instability in Laser-Driven Burnthrough Experiments," to be published in *Physics of Fluids B*.

W. R. Donaldson and L. Mu, "Effect of Illumination Uniformity on GaAs Photoconductive Switches," to be published in

the *IEEE Journal of Quantum Electronics*.

H. E. Elsayed-Ali, J. W. Herman, and E. A. Murphy, "Ultrafast Laser Superheating of Metal Surfaces," to be published in the *Materials Research Society Symposia Proceedings*.

H. E. Elsayed-Ali and T. Juhasz, "Femtosecond Time-Resolved Thermomodulation of Thin Gold Films with Different Crystal Structures," to be published in *Physical Review B*.

E. M. Epperlein, "Fokker-Planck Modeling of Electron Transport in Laser-Produced Plasmas," to be published in *Laser & Particle Beams*.

E. M. Epperlein, "Implicit and Conservative Difference Scheme for the Fokker-Planck Equation," to be published in the *Journal of Computational Physics*.

E. M. Epperlein, "Effect of Electron Collisions on Ion-Acoustic Waves and Heat Flow," to be published in *Physics of Plasmas*.

E. M. Epperlein, R. W. Short, and A. Simon, "Transport and Sound Waves in Plasmas with Light and Heavy Ions," to be published in *Physical Review E*.

E. M. Epperlein and R. W. Short, "Comments on 'Theory and Three-Dimensional Simulation of Light Filamentation in Laser-Produced Plasmas' [Phys. Fluids B **5**, 2243 (1993)]" to be published in *Physics of Fluids B*.

E. M. Epperlein and R. W. Short, "Generalized Electron Fluid Equations in the Presence of Laser Irradiation," to be published in *Physical Review Letters*.

T. Gong, J. F. Young, G. W. Wicks, P. J. Kelly, and P. M. Fauchet, "Hot-Carrier Dynamics Near the Fermi Edge of N-Doped GaAs," to be published in *Semiconductor Science and Technology*.

T. Gong and P. M. Fauchet, "Carrier-Carrier Interactions in GaAs Investigated by Femtosecond Spectroscopy," to be published in the *Proceedings of SPIE's OE/LASE '93*, Los Angeles, CA, 16–23 January 1993 (invited).

D. Gupta, W. R. Donaldson, and A. M. Kadin, "A Laser-Triggered, Inductive Opening Switch Using High-Temperature Superconducting Thin Films," to be published in *Advances in Cryogenic Engineering*.

D. Gupta, "A New Optically Triggered Superconducting Opening Switch for High-Power Applications," to be published in *Research Reports of the Link Energy Fellows*.

D. Gupta, W. R. Donaldson, and A. M. Kadin, "Fast Inductively Coupled Superconducting Opening Switch Triggered by Short Laser Pulses," to be published in the *Proceedings of the 9th IEEE International Pulsed Power Conference*.

J. W. Herman, H. E. Elsayed-Ali, and E. A. Murphy, "Time-Resolved Structural Studies of the Low-Index Faces of Lead," to be published in *Physical Review B*.

S. D. Jacobs, K. L. Marshall, and A. Schmid, "Liquid Crystals for Laser Applications," to be published in the *CRC Handbook of Laser Science and Technology, Supplement 2: Optical Materials*.

A. M. Kadin, D. Gupta, D. D. Mallory, M. Takahashi, W. R. Donaldson, and J. K. Truman, "Fabrication, Properties, and Applications of *In-Situ* Sputtered YBCO Films," to be published in the *Proceedings of the 6th Annual Conference on Superconductivity and Applications*, Buffalo, NY, 15–17 September 1992.

H. Kim, J. M. Soures, and P.-C. Cheng, "Confocal Microscopic Characterization of Laser-Fusion Target," to be published in the *Proceedings of the 39th AVS National Symposium and Topical Conferences*, Chicago, IL, 9–13 November 1992.

H. Kim and M. D. Wittman, "Optical Characterization of Inertial-Fusion Targets—An Overview," to be published in *Multidimensional Microscopy*.

E. M. Korenic, S. D. Jacobs, J. K. Houghton, F. Kreuzer, and A. Schmid, "Nematic Polymer Liquid-Crystal Waveplate for High-Power Lasers at 1054 nm," to be published in *Applied Optics*.

Y. Kostoulas, T. Gong, G. W. Wicks, and P. M. Fauchet, "Femtosecond Carrier Dynamics in Low-Temperature-Grown InP," to be published in *Applied Physics Letters*.

Y. Kostoulas, T. Gong, and P. M. Fauchet, "Investigation of Carrier-Carrier Scattering by Three-Pulse Probe Spectroscopy," to be published in *Semiconductor Science and Technology*.

W. Kula and R. Sobolewski, "Electric-Field-Effect Devices Based on Partially Oxygen-Depleted, Superconducting Y-Ba-Cu-O Thin Films," to be published in *Advances in Cryogenic Engineering*, Volume 40.

W. Kula and R. Sobolewski, "Electric-Field Effect in Partially Deoxygenated YBCO Thin Films," to be published in *Physica B*.

W. Kula and R. Sobolewski, "Charging Effect in Partially Oxygen-Depleted, Superconducting Y-Ba-Cu-O Thin Films," to be published in *Physical Review B*.

Y. Lin and T. J. Kessler, "Raman Scattering: A Four-Dimensional System," to be published in *Applied Optics*.

A. I. Lobad, S. M. Mehta, B. C. Tousley, P. J. Rodney, and P. M. Fauchet, "The Starting Mechanism in Coupled-Cavity Mode-Locked Laser Systems," to be published in the *IEEE Journal of Quantum Electronics*.

R. S. Marjoribanks, F. W. Budnik, H. Chen, and D. D. Meyerhofer, "Plasma Electron Temperature in Picosecond Laser Plasmas from Quasi-Steady Ratio of Isoelectronic Lines," to be published in *Physical Review Letters*.

F. J. Marshall, J. A. Delettrez, R. Epstein, and B. Yaakobi, "Diagnosis of Laser-Target Implosions by Space-Resolved Continuum Absorption X-Ray Spectroscopy," to be published in *Physical Review E*.

R. L. McCrory, "Progress Toward Ignition with Direct Drive," to be published in *Concerning Major Systems in Science and Technology*.

P. W. McKenty, S. Skupsky, J. H. Kelly, and C. T. Cotton, "Numerical Investigation of the Self-Focusing of Broad-Bandwidth Laser Light with Applied Angular Dispersion," to be published in the *Journal of Applied Physics*.

D. D. Meyerhofer and J. Peatross, "Angular Distributions of High-Order Harmonics," to be published in *SILAP (Super-Intense Laser Atom Physics)*.

L. Mu and W. R. Donaldson, "Simulating Photoconductive Switches in a Microwave Transmission Line," to be published in the *Proceedings of the 9th IEEE International Pulsed Power Conference*, Albuquerque, NM, 21–23 June 1993.

S. Papernov and A. W. Schmid, "Atomic Force Microscopy Studies of Laser-Triggered Morphology Changes in Y_2O_3 Monolayer Coatings," to be published in *SPIE's Proceedings of the Annual Symposium on Optical Materials for High Power Lasers*.

S. Papernov and A. W. Schmid, "Atomic Force Microscopy Observations of Water-Induced Morphological Changes in Y_2O_3 Monolayer Coatings," to be published in *SPIE's Proceedings of the Annual Symposium on Optical Materials for High Power Lasers*.

J. Z. Roach, A. Ninkov, S. W. Swales, and T. Morris, "Design and Evaluation of a Screen CCD Imaging System," to be published in *Optical Engineering*.

J. K. Samarabandu, R. Acharya, C. D. Edirisinghe, P. C. Cheng, H. Kim, T. H. Lin, R. G. Summers, and C. E. Musial, "Analysis of Multi-Dimensional Confocal Images," to be published in the *Proceedings of the SPIE Symposium "Biomedical Imaging,"* San Diego, CA, 24 February 1991.

A. W. Schmid, K. L. Marshall, and S. D. Jacobs, "Comment to 'Ultraviolet Filters Using Liquid Crystal Molecules' [J. Appl. Phys. **74**, 4867 (1993)]," to be published in the *Journal of Applied Physics*.

L. Shi, T. Gong, W. Xiong, X. Weng, Y. Kostoulas, R. Sobolewski, and P. M. Fauchet, "Femtosecond Reflectivity of 60-K Y-Ba-Cu-O Thin Films," to be published in *Applied Physics Letters*.

H. Shi and S.-H. Chen, "Novel Glassy Nematic and Chiral Nematic Oligomers Derived from 1,3,5-Cyclohexane-tricarboxylic and (1R,3S)-(+)-Camphoric Acids," to be published in *Liquid Crystals*.

S. Skupsky and T. J. Kessler, "A Speckle-Free Phase Plate (Diffuser) for Far-Field Applications," to be published in the *Journal of Applied Physics*.

R. Sobolewski, W. Xiong, W. Kula, and J. R. Gavaler, "Laser Patterning of Y-Ba-Cu-O Thin-Film Devices and Circuits," to be published in *Applied Physics Letters*.

R. Sobolewski, W. Xiong, W. Kula, and B McIntyre, "Electrical and Structural Properties of the YBCO Super-conducting-Semiconducting Interface," to be published in *Physica B*.

B. Soom, H. Chen, Y. Fisher, and D. D. Meyerhofer, "Strong K_α Emission in Picosecond Laser-Plasma Interactions," to be published in *OSA's Proceedings of Shortwavelength V: Physics with Intense Laser Pulses* ('93).

J. M. Soures, "The OMEGA Upgrade Laser Facility for Direct-Drive Experiments," to be published in the *Proceedings of the Fusion Power Associates Annual Meeting and Symposium*, Princeton, NJ, 25–26 June 1991, and in the *Journal of Fusion Energy*.

C. J. Twomey, S. H. Chen, T. Blanton, A. W. Schmid, and K. L. Marshall, "Solid Polymers Doped with Rare Earth Metal Salts. II. Thermal Behavior and Morphology of the Neodymium Acetate-Poly(ethylene oxide) System," to be published in the *Journal of Polymer Science, Polymer Physics Edition*.

C. J. Twomey, S.-H. Chen, T. Blanton, A. W. Schmid, and K. L. Marshall, "Solid Polymers Doped with Rare Earth Metal Compounds. III. Formation and Stability of Macromolecular Complexes Comprising Neodymium Nitrate and Dipivaloylmethane in Poly(Ethylene Oxide)," to be published in the *Journal of Polymer Science, Polymer Physics Edition*.

C. J. Twomey, S.-H. Chen, T. N. Blanton, A. W. Schmid, and K. L. Marshall, "Stoichiometry and Morphology in Terbium Nitrate-Poly (Ethylene Oxide) Macromolecular Complex," to be published in the *Journal of Polymer Science, Polymer Physics Edition*.

C. J. Twomey, S.-H. Chen, T. N. Blanton, P. W. Schmid, and K. L. Marshall, "Poly[(Methylene Oxide)Oligo(Ethylene Oxide)]vs Poly(Ethylene Oxide) as Hosts for Neodymium Compounds," to be published in the *Journal of Polymer Science, Polymer Physics Edition*.

C.-C. Wang, S. Alexandrou, and T. Y. Hsiang, "Picosecond Metal-Semiconductor-Metal and Silicon-on-Sapphire Photodiodes," to be published in *Applied Physics Letters*.

M. D. Wittman, R. Q. Gram, H. Kim, C. K. Immesoete, S. G. Noyes, and S. Scarantino, "Increased Retention Time for Hydrogen and Other Gases by Polymer Shells Using Optically Transparent Aluminum Layers," to be published in the *Journal of Vacuum Science and Technology*.

W. Xiong, W. Kula, and R. Sobolewski, "Fabrication of High Superconducting Electronic Devices Using the Laser-Writing Patterning Technique," to be published in *Advances in Cryogenic Engineering*, Volume 40.

W. Xiong, W. Kula, R. Sobolewski, W. N. Maung, and D. P. Butler, "Monolithic Y-Ba-Cu-O Electronic Devices Fabricated Using the Laser-Writing Patterning Technique," to be published in *Superconductor Science and Technology*.

B. Yaakobi, Q. Su, and F. J. Marshall, "Monochromatic Backlighting in Laser-Fusion Experiments," to be published in the *Journal of X-Ray Science and Technology*.

B. Yaakobi, F. J. Marshall, R. Epstein, and Q. Su, "New Diagnostic Features in the Laser Imposions of Argon-Filled Targets," to be published in *Optics Communications*.

L. Zheng and D. D. Meyerhofer, "A Linear Cross-Correlation Technique for Single-Shot Measurements of Weak Light Pulses," to be published in *Optics Letters*.

X. Zhou, S. Alexandrou, and T. Y. Hsiang, "Monte Carlo Investigation of the Mechanism of Subpicosecond Pulse Generation by Nonuniform Gap Illumination," to be published in *Applied Physics Letters*.

Conference Presentations

The following presentations were made at the 1993 OSA Annual Meeting, Toronto, Canada, 3–8 October 1993:

J. J. Armstrong and T. J. Kessler, "Holographic Diffractive Optics for Use in High-Peak-Power Laser Systems."

D. L. Brown, I. Will, R. G. Roides, C. K. Merle, M. D. Skeldon, and W. Seka, "Regenerative Amplifier with Negative Feedback for Enhanced Amplitude Stability and External Synchronizability."

D. Fried, J. D. B. Featherstone, W. Seka, R. Glena, and B. Bordyn, "Light Scattering in Dental Hard Tissues."

C. Kellogg, K. Kubath, A. Maltsev, and T. J. Kessler, "The Fabrication and Testing of a High-Damage-Threshold, UV Transmissive, Lens Array Telescope."

J. H. Kelly, K. A. Thorp, R. L. Keck, M. D. Tracy, C. Cotton, R. G. Roides, C. K. Merle, M. M. Tedrow, B. Staat, and I. Will, "Design and Performance of a Flexible, kJ-Class Frequency-Converted, Single-Beam Nd:Glass Laser."

Y. Lin, T. J. Kessler, and G. Lawrence, "Optical-Phase-Plate Design and Modeling for Laser Fusion."

J. Peatross and D. D. Meyerhofer, "Observation of Intensity-Dependent Phase of Atomic High-Harmonic Emission in the Far-Field Angular Distribution."

W. Seka, I. Will, J. Chow, D. L. Brown, M. D. Skeldon, C. K. Merle, R. G. Roides, and W. Ragg, "Highly Reliable, Stable, and Synchronizable Long-Pulse Mono-Mode Oscillator for Laser-Fusion Drivers."

M. D. Skeldon, "Transverse Modulational Instabilities in the Presence of Stimulated Rotational Raman Scattering with a High-Power Laser."

R. Stewart, S. Bui, and T. J. Kessler, "Spectral Masks for Optical Pulse Shaping of Lasers in Fusion."

M. D. Tracy, I. Will, C. K. Merle, R. G. Roides, K. Thorp, M. D. Skeldon, J. H. Kelly, and W. Seka, "Versatile Front-End Laser System for Laser-Fusion Drivers."

J. D. Zuegel and W. Seka, "Direct Measurements of Gain-Saturation Phenomena in Nd:YLF," ILS IX (1993), Toronto, Canada, 3–8 October 1993.

S. A. Letzring, "Design of a 60-kJ, 60-Beam Upgrade to the OMEGA Laser at the Laboratory for Laser Energetics, University of Rochester," 15th Symposium on Fusion Engineering, Hyannis, MA, 11–15 October 1993

T. E. Fortner and M. J. Shoup III, "Cooling Flow Management System for the OMEGA Laser System," Sensors Expo, Philadelphia, PA, 26–28 October 1993.

The following presentations were made at the XXV Boulder Damage Symposium on Optical Materials for High Power Lasers, Boulder, CO, 27–29 October 1993:

S. Papernov and A. W. Schmid, "Atomic Force Microscopy Studies of Laser-Triggered Morphology Changes in Y_2O_3 Monolayer Coatings."

S. Papernov and A. W. Schmid, "Atomic Force Microscopy Observations of Water-Induced Morphological Changes in Y_2O_3 Monolayer Coatings."

The following presentations were made at the 35th Annual Meeting of the American Physical Society, Division of Plasma Physics, St. Louis, MO, 1–5 November 1993:

R. Betti, R. L. McCrory, and C. P. Verdon, "Linear Growth Rates of the Ablative Rayleigh-Taylor Instability."

R. Betti and J. P. Freidberg, "Stability of the $m = 1$ Internal Kink in Ignited Plasmas."

T. R. Boehly, R. S. Craxton, R. J. Hutchison, J. H. Kelly, T. J. Kessler, S. A. Kumpan, S. A. Letzring, R. L. McCrory, S. F. B. Morse, W. Seka, S. Skupsky, J. M. Soures, and C. P. Verdon, "Progress on the Upgrade to the OMEGA Laser System."

D. K. Bradley, J. A. Delettrez, P. A. Jaanimagi, S. Skupsky, and C. P. Verdon, "Measurements of the Effects of Pulse Shaping on Rayleigh-Taylor Growth in Burnthrough Targets."

A. V. Chirokikh, W. Seka, R. S. Craxton, R. E. Bahr, A. Simon, R. W. Short, E. M. Epperlein, H. Baldis, and R. P. Drake, "Stimulated Brillouin Scattering at 1.053 µm in OMEGA Long-Scale-Length Interaction Experiments."

R. S. Craxton, T. Afshar-Rad, M. Dunne, and O. Willi, "Numerical Modeling of a Thermal Smoothing Experiment."

G. Cripps, M. A. Russotto, C. P. Verdon, S. Skupsky, and R. L. Kremens, "Simulation of Laser-Fusion Activation Diagnostics."

J. A. Delettrez, G. Bonnaud, P. Audebert, J. P. Geindre, and J. C. Gauthier, "PIC Code Simulations of the Interaction of 100-fs Gaussian Laser Pulses with Targets of Varying Scale Lengths."

E. M. Epperlein, "Implicit-Conservative Fokker-Planck Simulations of Heat Flowing Laser Fusion."

R. Epstein, S. Skupsky, and C. P. Verdon, "Smoothing of Laser Irradiation of Spherical ICF Targets Using a Pre-Formed Refracting Atmosphere Containing Small Inhomogeneities."

Y. Fisher, B. Soom, and D. D. Meyerhofer, "Ion Emission from High-Contrast, Picosecond, Laser-Plasma Interactions."

R. E. Giacone, C. J. McKinstrie, and R. Betti, "Angular Dependence of SBS in Homogeneous Plasma."

J. P. Knauer, C. P. Verdon, T. J. Kessler, S. Skupsky, R. L. McCrory, J. M. Soures, S. G. Glendinning, S. V. Weber, R. J. Wallace, S. N. Dixit, M. A. Henesian, J. D. Kilkenny, and H. T. Powell, "Stabilization of the Rayleigh-Taylor Unstable Ablation Interface with Trace Amounts of Chlorine."

J. S. Li, C. J. McKinstrie, and C. Joshi, "Thermal Filamentation of Counterpropagating Light Waves."

C. J. McKinstrie, J. S. Li, and C. Joshi, "Sideward SBS of Counterpropagating Light Waves."

D. D. Meyerhofer, H. Chen, J. A. Delettrez, E. M. Epperlein, Y. Fisher, and B. Soom, "Thermal Heat Front Penetration in Picosecond Laser-Plasma Interactions."

W. Seka, R. E. Bahr, R. S. Craxton, A. Chirokikh, R. W. Short, A. Simon, H. Baldis, and R. P. Drake, "OMEGA Long-Scale-Length Laser-Plasma Experiments."

R. W. Short, "Stimulated Brillouin Scattering Driven by Smoothed Laser Beams."

A. Simon, "The Effect of Jets of Accelerated Ions on Scattered Laser Light Near ω_0."

M. D. Tracy and E. M. Epperlein, "Eigenvalue Solution of the Fokker-Planck Equation for Ion-Acoustic and Entropy Waves in Multi-Species Plasmas."

C. P. Verdon, R. Betti, and R. L. McCrory, "Dynamic Stability of Imploding Shells."

C. P. Verdon, "High-Performance Direct-Drive Capsule Designs for the National Ignition Facility."

M. Yu, C. J. McKinstrie, and W. L. Kruer, "Relativistic Saturation of Forward SRS."

L. D. Lund, A. Rigatti, P. Glenn, and J. Glenn, "Characterization of Surface Particulate Contamination on Liquid-Crystal Optics for Laser Fusion," ASPE 8th Annual Meeting, Seattle, WA, 7–12 November 1993.

The following presentations were made at the 40th National AVS Symposium & Topical Conference, Orlando, FL, 15–19 November 1993:

R. Q. Gram, D. S. Brennan, S. G. Noyes, R. A. Mangano, and R. L. Fagaly, "A Low-Mass Mounting Method for Cryogenic Inertial-Fusion Targets."

H. Kim, P. W. McKenty, and P. Cheng, "Confocal Microscopy of Inertial-Fusion Fuel Capsules."

C. P. Verdon, "Target Requirements for the OMEGA Upgrade."

M. D. Wittman, "Compensation of the Lens Effects of Thick Cryogenic Layers Using an Interferometric Imaging System."

The following presentations were made at the Materials Research Society 1993 Fall Meeting, Boston, MA, 29 November–3 December 1993:

P. Gierlowski, W. Kula, S. J. Lewandowski, and R. Sobolewski, "Microwave Response of Mixed-Phase $Bi_2Sr_2Ca_2Cu_3O_x/Bi_2Sr_2Ca_1Cu_2O_y$ Thin Films."

W. Kula and R. Sobolewski, "Hydrogen Doping of Y-Ba-Cu-O Thin Films with Various Oxygen Content."

L. Shi, T. Gong, W. Xiong, X. Weng, Y. Kostoulas, R. Sobolewski, and P. M. Fauchet, "Dependence of Femtosecond Reflectivity on the Oxygen Content in Y-Ba-Cu-O Thin Films."

UNIVERSITY OF
ROCHESTER